U. PORTO

FC **FACULDADE DE CIÊNCIAS**
UNIVERSIDADE DO PORTO

Multiwavelength high precision radial velocities: pushing precision and characterizing astrophysical sources of noise

Diana da Cunha

Tese de Doutoramento apresentada à
Faculdade de Ciências da Universidade do Porto
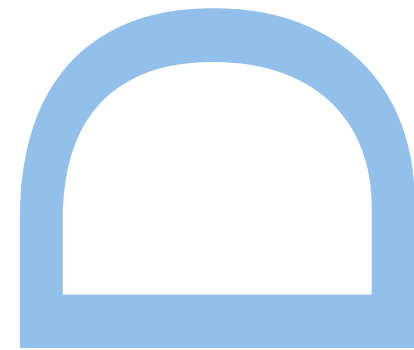Departamento de Física e Astronomia
2014
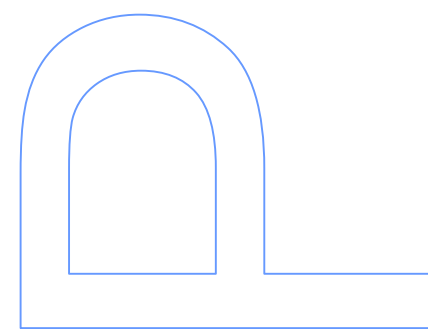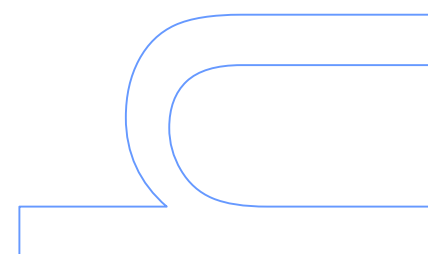
Image credit: Luis Calçada / ESO

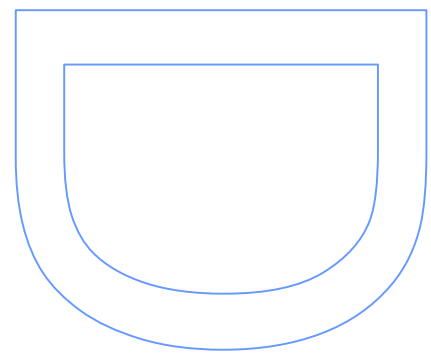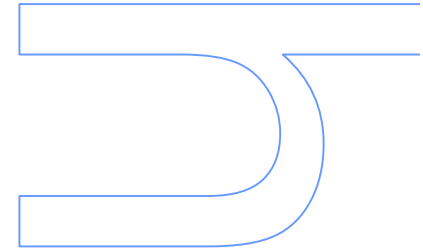# Multiwavelength high precision radial velocities: pushing precision and characterizing astrophysical sources of noise

Diana da Cunha
Doutoramento em Astronomia
Departamento de Física e Astronomia
2014

Orientador
Pedro Ricardo Lourenço Figueira,
Investigador Auxiliar, Centro de Astrofísica da Universidade do Porto

Coorientador
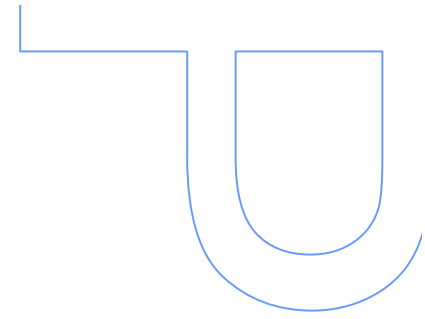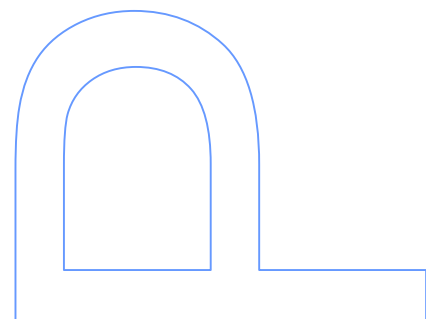Nuno Miguel Cardoso Santos,
Professor Associado Convidado, Faculdade de Ciências
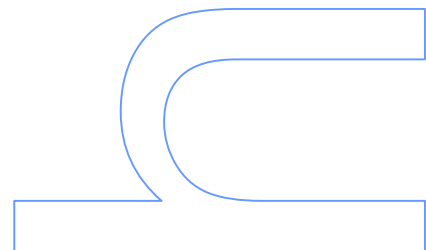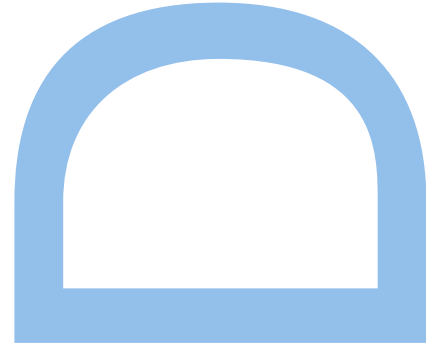
Diana da Cunha

Multiwavelength high precision radial velocities: pushing precision and characterizing astrophysical sources of noise

U.PORTO

FC FACULDADE DE CIÊNCIAS
UNIVERSIDADE DO PORTO

Tese submetida à Faculdade de Ciências
da Universidade do Porto para obtenção
do grau de Doutor em Astronomia.

Defesa pública: 21 de Abril de 2015

O júri de doutoramento:

Presidente:	Prof. Doutor Orfeu Bertolami
Orientador:	Doutor Pedro Ricardo Lourenço Figueira
Co-orientador:	Doutor Nuno Miguel Cardoso Santos
Outros vogais:	Doutor Francesco Pepe
	Doutor Joã M. Fernandes
	Doutor Johannes Sahlmann
	Doutor Jorge Fílipe da Silva Gameiro

Fiat lux!

Et terra erat inanis et vacua

Tinham os astros já mil annos, –
tinham
Talvez cem mil – ou tinham um
minuto –
Pois quem sabe contar horas ou
seculos
No relogio – que tem o firmamento
Por quadrante, – e algarismos, sóes e
estrellas?)[...]

— Antero de Quental, 1863

To my family.

Acknowledgements

And the journey is coming to an end...

I would like to thank all those of you that, in a way or another, helped me through this challenge.

Then, I would like to thank my supervisors for all their guidance, support, and patience. It is good to have supervisors with such great sense of leadership, and at the same time a young, friendly, and adventurous spirit.

To the jury members of this thesis, my thanks for the time spent reading my work.

I can not forget the people from the CAUP (IA-UP). From the administration department, outreach unit, stars and planets team, those with whom I go for lunch, and some times for dinner and/or drinks, to the "+1s" that usually join us, to the ex-"symposium" fellows, my office mates, not forgetting those who already left, my special thanks for your support, work discussions, and friendship. ExoEarths team: 2-DEMOC forever!

My thanks go also to all my friends: to those who have been my friends and accompanied my journey since elementary school, those who became my friends during high-school, and have been part of my life ever since, those who have time for a chat, a dinner, or a "Kima maracujá" when I go visit my homeland; also to those who entered in my life and heart during faculty: ex-classmates, ex-roommates, ex-flatmates, ex-flatmates that have become my neighbors, and their "+1s". We may not always be together, but you are never forgotten. You have played your part helping me through the less good moments, encouraging me, and getting me to this moment.

To my boyfriend, thank you! Thank you for the support, patience, for being at my side all these years, at the good and at the not so good moments of my personal and working life.

To all my family that in some way or another had showed me their support during my

academic path, especially to my big brothers and big sister, my thanks go to all of you as well.

Lastly, a special thanks to my parents for their caring, patience, for the education they gave me, and all the efforts and sacrifices they made to get me further. You may no longer be among us, but you both are always in my heart.

Abstract

In the near future, new instruments such as ESPRESSO will arrive, allowing us to reach a precision in radial-velocity measurements of the order of $10\,\mathrm{cm\ s^{-1}}$. At this level of precision, several noise sources that until now have been outweighed by photon noise will start to contribute significantly to the error budget. A stellar companion within the fiber is such a possible noise source, as well as the telluric lines that are not neglected by the masks for the radial velocity computation, here called micro-telluric lines.

In this thesis I aim at characterizing the impact of a stellar companion within the fiber to radial velocity measurements made by fiber-fed spectrographs. I consider the contaminant star either to be part of a binary system whose primary star is the target star, or as a background/foreground star. I also investigate the impact of micro-telluric lines in the radial velocities calculations, and how to correct for their effect (on radial velocities).

To carry out our study on the impact of a stellar companion within the fiber, I used HARPS spectra, co-added the target with contaminant spectra, and then compared the resulting radial velocity with that obtained from the original target spectrum. I repeated this procedure and used different tunable knobs to reproduce the previously mentioned scenarios.

I find that the impact on the radial velocity calculation is a function of the difference between individual radial velocities, of the difference between target and contaminant magnitude, and also of their spectral types. For the worst-case scenario in which both target and contaminant star are well centered on the fiber, the maximum contamination for a G or K star may be higher than $10\,\mathrm{cm\ s^{-1}}$, on average, if the difference between target and contaminant magnitude is $\Delta m < 10$, and higher than $1\,\mathrm{m\ s^{-1}}$ if $\Delta m < 8$. If the target star is of spectral type M, $\Delta m < 8$ produces the same contamination of $10\,\mathrm{cm\ s^{-1}}$, and a contamination may be higher than $1\mathrm{m\ s^{-1}}$ if $\Delta m < 6$.

In the study of the impact of micro-telluric lines in the radial velocities calculations, I follow two parallel lines. First, I calculated the impact of the micro-telluric lines by multiplying a synthetic solar-like stellar spectrum by synthetic atmospheric spectra and evaluated the effect created by the presence of the telluric lines. Then, I divided HARPS spectra by synthetic at-

mospheric spectra to correct for its presence on real data and calculated the radial velocity on the corrected spectra. When doing so, we consider two atmospheric models for the synthetic atmospheric spectra.

I find that the micro-telluric lines can induce an impact on the radial velocities calculation that can already be close to the current precision achieved with HARPS, and so its effect should not be neglected, especially for future instruments such as ESPRESSO. Moreover, we find that the micro-telluric lines' impact depends on factors, such as the radial velocity of the star, airmass, H_2O vertical column, and the barycentric Earth radial velocity projected along the line of sight at the time of the observation.

Resumo

Num futuro próximo, novos instrumentos, tal como o spectrógrafo ESPRESSO, ficarão operacionais, permitindo atingir uma precisão nas medidas das velocidades radiais na ordem dos $10\,\mathrm{cm\,s^{-1}}$. Com este nível de precisão, várias fontes de ruído até agora escondidas pelo ruído dos fotões começarão a contribuir significativamente para os erros. A presença de uma companheira estelar dentro da fibra é exemplo de uma tal fonte de ruído. Outro exemplo é a presença no espectro estelar de riscas atmosféricas que não são ignoradas pelas máscaras usadas no cálculo da velocidade radial. A essas riscas baptizamos de micro-telúricas.

Com o trabalho feito durante este doutoramento pretende-se caracterizar, usando dados obtidos com espectrógrafos de fibra óptica, o impacto que a presença de uma companheira estelar dentro da fibra pode ter na determinação da velocidade radial. Neste trabalho considera-se que a estrela contaminante tanto pode ser a estrela secundária de um binário em que a estrela principal é a nossa estrela alvo, como também pode simplesmente ser uma estrela em plano de fundo ou em primeiro plano. Também é investigado o impacto das micro-telúricas no cálculo das velocidades radiais, bem como um método para a correção destas riscas atmosféricas.

Para o estudo do impacto de uma companheira estelar dentro da fibra usámos dados obtidos com o espectrógrafo HARPS, adicionou-se o espectro da estrela alvo ao da contaminante, e depois comparou-se a velocidade radial obtida com aquela resultante apenas do espectro da estrela alvo. Este procedimento foi repetido usando diferentes combinações que reproduzissem os vários cenários mencionados anteriormente.

Verifica-se que o impacto de uma companheira estelar na determinação da velocidade radial é função da diferença entre as velocidades radiais individuais das estrelas envolvidas, da diferença entre as magnitudes das duas estrelas e também do seu tipo espectral. No caso limite, em que tanto a estrela alvo como a estrela contaminante estão bem centradas na fibra, a contaminação numa estrela de tipo espectral G ou K pode, em média, ser maior do que $10\,\mathrm{cm\,s^{-1}}$ no caso de a diferença entre a magnitude das duas estrelas ser de $\Delta m < 10$, e maior do que $1\,\mathrm{m\,s^{-1}}$ no caso de $\Delta m < 8$. Se a estrela alvo for do tipo espectral M, um $\Delta m < 8$ produz a mesma contaminação de $10\,\mathrm{cm\,s^{-1}}$, enquanto que um $\Delta m < 6$ produz uma contaminação que pode ser maior do que $1\,\mathrm{m\,s^{-1}}$.

No estudo do impacto das riscas micro-telúricas na velocidade radial, seguiu-se dois caminhos paralelos. Primeiro, calculou-se o impacto das riscas micro-telúricas multiplicando um espectro sintético de uma estrela do tipo solar por um espectro sintético da atmosfera terrestre, e avaliou-se o efeito criado pela presença das riscas telúricas. Depois dividiu-se espectros obtidos com o HARPS por espectros atmosféricos sintéticos de modo a corrigir a sua presença em espectros observacionais e calculou-se a velocidade radial dos espectros corrigidos. Ao criar os espectros sintéticos da atmosfera da Terra considerou-se dois modelos atmosféricos diferentes.

Verificou-se que as riscas micro-telúricas podem induzir um impacto nas velocidades radiais que pode já ser próximo da precisão actual alcançada com o HARPS, e portanto o seu efeito não se deve neglegenciado, em especial em futuros instrumentos do tipo do ESPRESSO. Mais ainda, verificou-se que o impacto das micro-telúricas depende de factores tais como a velocidade radial da estrela, massa de ar, coluna vertical de H_2O e da velocidade radial baricêntrica da Terra projectada ao longo da linha de visão na altura da observação.

Contents

List of Figures

Chapter 1

Introduction

Since the discovery by Mayor & Queloz (1995) of *51 Peg b*, the first discovered planet orbiting a star other than the Sun, all the efforts have been made to find a planet similar to our own planet Earth. Over the past almost 20 years we have witnessed a great improvement of the instruments and techniques in the search of Exoplanets. A clear mark of this improvement was the discovery of the planet *μ Ara c* by Santos et al. (2004). This was the first of a new class of planets of the Neptune mass. Its discovery was only possible due to the (at the time) "new and unique planet-hunting machine HARPS (High-Accuracy Radial velocity Planetary Searches)" (Mayor et al. 2003). It was also with HARPS that *Gl 581 e*, a planet with a minimum mass of less than $2\,M_{\oplus}$, was found later on by Mayor et al. (2009).

It is important to stress that what is considered to be a good precision/accuracy today, may no longer considered to be a good precision/accuracy in a short period of time from now. In 1996 the ELODIE spectrograph (the one with which *51 Peg b* was found) had allowed the measurement of Radial Velocity (RV) with an precision better than $15\,\mathrm{m\,s^{-1}}$ for stars up to 9th magnitude in less than than 30 minutes exposure time (Baranne et al. 1996). Just seven years later, by October 2003, HARPS become operational permitting the detection of exoplanets at a level of $1\,\mathrm{m\,s^{-1}}$ (Mayor et al. 2003). But in spite of the great improvements over the last past years, these were not enough to find an Earth like planet orbiting a Sun like star. One shall not forget that the RV semi-amplitude induced by our planet on the Sun is only of $8.9\,\mathrm{cm\,s^{-1}}$, much lower than the accuracy currently achieved by HARPS. To meet this requirement, new instruments are already being planned and constructed. This is the case of ESPRESSO (Echelle SPectrograph for Rocky Exoplanet - and Stable Spectroscopic Observations) for the VLT (Very Large Telescope) (Pepe et al. 2010) and of HIRES (high resolution spectrograph) for the E-ELT (European - Extreme Large Telescope)(Maiolino et al. 2013), two spectrographs that aim at to reach a RV precision of better than $10\,\mathrm{cm\,s^{-1}}$.

One of the limitations to the RV precision is the presence of systematic errors present in the

measurements. With the increasing precision of the instruments, new systematics become important. It is therefore important to identify and to characterize all the systematics that cam limit the attainable precision.

In this PhD thesis, I want to address systematic errors that can affect planetary searches. For a better framework of this thesis, the first and second chapters will be reserved to a brief review on exoplanets and its search methods and techniques, to the enunciation of the open question in this area and to the key scientific goals of this work. The third chapter will be reserved to the study of the impact of possible stellar companions contamination within the fiber in the RV calculation, and the fourth to the study of the impact of micro-telluric lines in the RV calculation. In the fifth chapter we will present the conclusions and some propositions for future work.

1.1 Exoplanet definition

Before present and discuss the methods and techniques of exoplanets detection, we should establish a planet definition. Although this may seem a simple question, it was only in 2006 that the IAU (International Astronomical Union) provided a definition of planet only applicable to the Solar System (Binzel 2006):

"A planet is a celestial body that

(a) is in a orbit around the Sun,

(b) has sufficient mass for its self-gravity to overcome rigid body forces so that it assumes a hydrostatic equilibrium (nearly round) shape, and

(c) has cleared the neighbourhood around its orbit".

It was this definition that demoted Pluto from the planet status.

A few years before the IAU Solar System planet definition, the IAU Working Group on Extrasolar Planets (WGESP) provided the following statements about low mass companions (Boss et al. 2003):

1. "Objects orbiting around solar-type stars with true masses above the limiting mass for thermonuclear fusion of deuterium (currently calculated to be 13 Jupiter masses for objects of solar metallicity) are "brown dwarfs" (no matter how they formed) while objects with true masses below this limiting mass are "planets".

2. Free-floating objects in young star clusters (which presumably formed in the same way as stars and have not been shown to be ejected from planetary

systems) with masses below the limiting mass for thermonuclear fusion of deuterium are not "planets", but are "sub-brown dwarfs" (or whatever name is more appropriate)".

This is not a unanimous definition. As an example, Chabrier et al. (2014) suggests that an exoplanet definition should take into account the formation process.

1.2 Detection methods

In this section I will present the exoplanets detection methods. The use of different methods gives access to different information about the planets. Therefore, although the work presented in this thesis only makes use of the RV method, it it important to understand each method to allow a better utilization and synergy between the methods.

1.2.1 Radial velocities

The RV of a star is nothing more than its velocity in the direction of the line of sight. Up to today, we can count more than 1800 discovered exoplanets [1]. From these, about 580 were discovered making use of the RV method. Putting into simple words, the RV method measures the Doppler shift in the stellar spectral lines. If a star is moving towards the Earth, its light will be blue shifted (shorter wavelength and higher frequency); on the other hand, if a star is moving away from Earth, its light will be redshifted (longer wavelength and lower frequency). An illustration of this effect is shown in Fig. 1.1. If one or more planets are present, the system's center of mass will not be the center of mass of the star. Therefore, the star will orbit around the center of mass of the system. The back-and-forth movement of the star is traduced in periodic variations of the Doppler shift. The semi-amplitude of these variations is given by

$$K_1 = \left(\frac{P}{2\pi G}\right)^{-\frac{1}{3}} \left(1 - e^2\right)^{-\frac{1}{2}} \frac{M_2 \sin i}{(M_1 + M_2)^{\frac{2}{3}}}, \tag{1.1}$$

where P is the orbital period, G the gravitational constant, e is the eccentricity of the orbit, i is the inclination of the orbital plane with respect to the tangent plane of the sky, and M_1 and M_2 are, respectively, the masses of the star and of the planet (Cumming et al. 1999). If one assumes that $M_2 << M_1$, the semi-amplitude can be written as

$$K_1 = \frac{28.43}{\sqrt{1 - e^2}} \frac{M_2 \sin i}{M_J} \left(\frac{M_\odot}{M_1}\right)^{\frac{2}{3}} \left(\frac{1\,yr}{P}\right)^{\frac{1}{3}} \quad \mathrm{m\,s^{-1}}, \tag{1.2}$$

---

[1] from The Extrasolar Planets Encyclopaedia (www.exoplanets.eu) on 28/October/2014
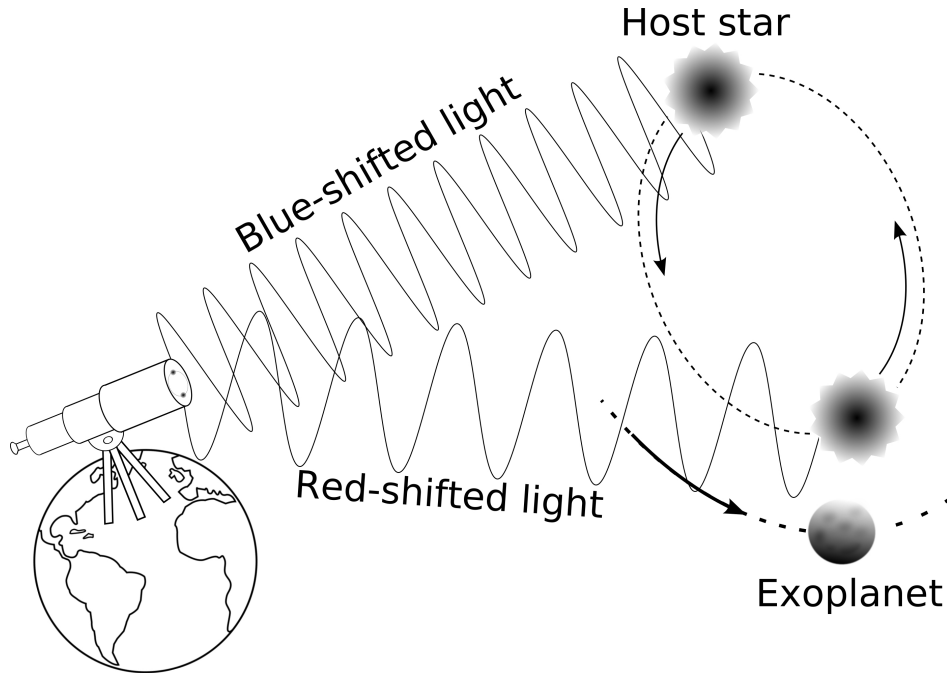
Figure 1.1: Illustration of the Radial Velocity technique.

where $M_\odot$ is the mass of the Sun, and M_J is Jupiter mass. It easy to check that the RV semi-amplitude induced by Jupiter if of $12.5\,\mathrm{m\,s}^{-1}$, and that the RV semi-amplitude induced by Earth is only of $8.9\,\mathrm{cm\,s}^{-1}$, much below of the precision reached with current instrumentation. One can also see that the closer the planet is to the host star, the larger will be the induced RV. It is also important to notice that the RV method does not provide the exact mass of the planet, unless i is known. $M_2 \sin i$ is called the "minimum mass". To find the inclination of the orbital plane one has to resort to another method, like the photometric transit method or astrometry.

1.2.2 Photometric transits

The photometric transit method consists of the measurement of the dimming of star light during the passage of the planet in front of the host star (see illustration of Fig. 1.2). This is a more advantageous method for planets of short period than long ones, because the transit probability is higher, and it is easier to monitor photometrically shorter spans. From the orbital fit one can measure the ratio between the radius of the planet and the one of the star (R_p/R_s), the ratio between the radius of the star and the semi-major axis (R_s/a) and the inclination. If the transit light curve, the RV, and the stellar properties information are available, one can completely classify the system orbital parameters, and also calculate the real mass of the planet.
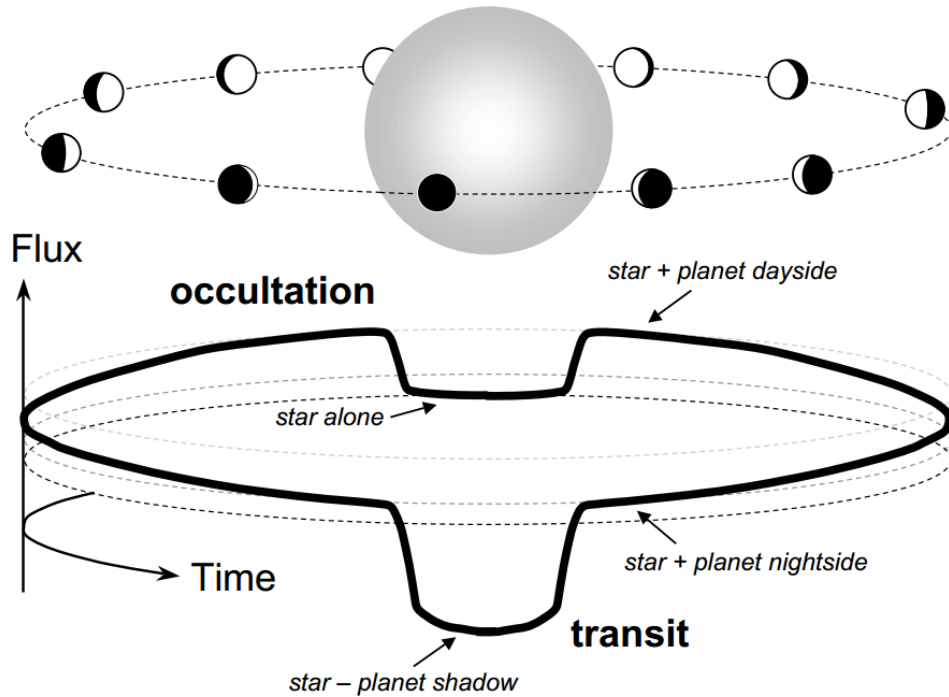
Figure 1.2: Illustration of transits and occultations. (Winn 2010)

However, by itself this method is prone to possible several types of false positives. The most common causes for false positives are grazing eclipses, the existence of triple systems, and the occurrence of transit by a low mass star. The first transit detection dates back to 1999 by Charbonneau et al. (2000). They observed the light curve by a gas giant planet around the host star *HD 209458*. Currently, the majority of the exoplanets discovery was made using this method. A big help for the increasing number of planet detected using this method have been the CoRoT and the Kepler missions. CoRoT (Convection, Rotation and planetary Transits) was launched in December 2006 and it is a space mission to study the Convection and Rotation of stars, and to detect planetary Transits (see as e.g. Baglin et al. 2006; Auvergne et al. 2009). But the "big champion" of planetary discoveries is Kepler, a NASA mission launched by March 2009, and it was build to be capable of finding Earth-size planets and in Earth-like orbits around other stars (see e.g. Borucki et al. 2010; Koch et al. 2010). This mission already counts with 989 confirmed planets and 4234 planet candidates [2].

1.2.3   Astrometry

The basic idea of this technique is to measure the projected orbital motion of the star in the sky. If one measures with precision the position of the star, and if the star has planets orbiting around, one can see the difference in the position of star with respect to the center

---

[2]as http://kepler.nasa.gov/ on 28/October/2014

of mass of the system. Dealing with the system as a binary system, and if the orbits are well characterized, one can measure the mass of the planetary companion. This method was not able to detect a planet until now, but it was already used to confirm or refute the presence of a planet detected with another method (e.g. Correia et al. 2010; Reffert & Quirrenbach 2011). An advantage of the astrometry is that the real mass of a planet can be measured and also the inclination of the orbit. This already permitted to distinguish between giant planets and brown dwarfs.

In the end of 2013, the Gaia mission was launched (e.g. de Bruijne 2012). Gaia was designed with the primary goal of investigating the origin and subsequent evolution of the Milky Way. With the astrometric measurements provided by this mission, astronomers expect to find exoplanet of the Jupiter size around solar type stars, and to explore Saturn-mass planets around late-type stars (Casertano et al. 2008; Sozzetti 2010; Perryman et al. 2014).

1.2.4 Direct imaging

Even though the principle of direct imaging method is very simple, the results are not so spectacular in terms of number of planets discovered. The biggest problem with direct imaging is that the light of the star will obfuscate the one coming from the planet: it is very difficult to find planets $10^6 - 10^9$ fainter than the star. Since planets around young stars are brighter than planets around old stars , direct imaging should look for planets around young objects. One of the major enemies of this method is the atmospheric turbulence, so the use of Adaptive Optics (AO) or space observatories are good allies. To reduce the contrast between the brightness of star and planet, it is better to observe in Infrared (IR) wavelengths. A coronagraph is also used to block the starlight. The first planet discovered with this method was around the star called *Fomalhaut*. *Fomalhaut b* lies about $119\,AU$ from the star and $18\,AU$ of the dust belt, matching predictions of its location (Kalas et al. 2008). In the same year, 2008, Marois et al. (2008) announce three planets orbiting the star HR 8799 revealed by high-contrast observations with the Keck and Gemini telescopes, using angular differential imaging (Marois et al. 2006). All the observed planets using this method were found in a orbit far from the host star, because these are the easiest planets to separate from starlight/resolve.

1.2.5 Microlensing

The microlensing method consists on the measurement of the effect of a planet gravity on the light of a distant star. The starlight is bent and focused by gravity as the exoplanet passes between the star and our planet. This method needs a large continuous photometric survey, because the probability of such a configuration is intrinsically low. One drawback of the gravitational microlensing method is that the parameters ore often ill-determined with large

error bars. Another issue is that usually the effect is observed only once, and so it cannot be verified. According to the Extrasolar Planets Encyclopaedia, 29 planets have been discovered up to now using this method. These discoveries were possible using the dedicated telescope networks OGLE (Udalski et al. 1997) and MOA.

1.2.6   Pulsar timing

Pulsars are small remnants of a star that has exploded as a supernova. As they rotate, the pulsars emit radio waves with an extreme regularity. The presence of a planet creates a time delay in these regular pulses. This method is so sensitive that it is able to detect very small planets, much lighter than any other method can currently do. The very first extra-solar planets were discovered by using this method (Wolszczan & Frail 1992). However, there are several disadvantages to this method. Since a pulsar is formed as a result of a supernova explosion, planets around these neutron stars are second generation planets and thus completely different from our own. Another disadvantage of the pulsar timing is the fact that pulsars emit high-energy radiation, making life, as we know and define it, impossible on these planets.

8

Chapter 2

Instruments, techniques and contamination sources for Radial Velocities

The fundamentals of the Radial Velocity method were presented in Cap. 1. This second chapter is dedicated to the instruments and techniques used to obtain and process the spectra used in the determination of the RVs and to the sources of contamination that may affect RV calculation.

2.1 Spectroscopy and spectrographs

When one is looking at a rainbow, one is, in fact, looking at the spectrum of the Sun. When sunlight enters a water drop, it is refracted, then it is internally reflected, and it is again refracted as it reaches the surface in its way out of the drop. Because the refraction of the light depends on the wavelength (blue light is refracted at a greater angle than red light), the white sunlight is separated in its component colors. To this effect we call dispersion.

From the study of the light coming from the astronomical sources one can obtain a lot of information. Just by using the naked eye, one can have an rough idea of stellar temperatures. Blue star are the hottest stars in the universe, then we have the white, yellow, and the cooler ones are red. The Sun, a yellow star, has a temperature of 5778 K.

The use of high precision spectra, in which detailed spectroscopic features can be identified (e.g., individual line wavelengths and shape), provide significant information:

- chemical composition can be inferred by knowing which atom or molecule produces the

transition;

- physical conditions, such as temperature and density of the environment local to the system, can be determined from assigning the actual transition being observed to the precise energy levels in the atom;

- chemical abundances can be determined if the intrinsic strength of the observed transition is known;

- radial velocities can be determined measuring the shift in the wavelength of the lines;

- pressure can be monitored observing the line profile. The greater the pressure, the more frequent the collision between species, the greater the broadening of the line.

There are many books where one can find information about astronomical spectroscopy. For reference the reader can look at Tennyson (2005).

In order to obtain spectra from the astronomical sources we one needs to make use of a spectrograph. Although there are several possibilities for the spectrograph design, its construction can be generically described as being formed by a light interface/feeding, a dispersive element, a detector, and ancillary optics (Fig. 2.1).
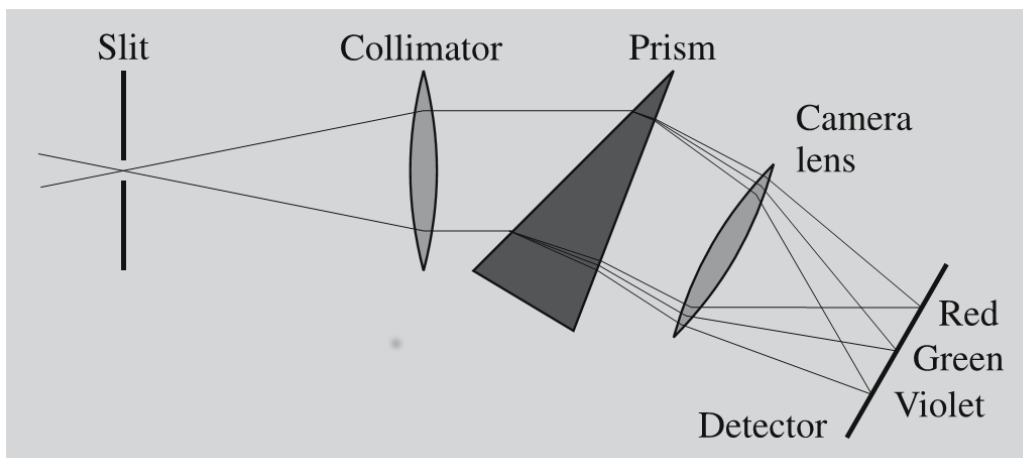
Figure 2.1: The principle of the slit spectrograph. Light rays entering through a slit are collimated (made parallel to each other), dispersed into a spectrum by a prism and projected onto a photographic plate or a CCD (from Karttunen et al. 2007).

2.1.1   Light feed elements

The light feed element selects the target objects in the field of view, and it can be either a slit or a fiber. The slit is in the focal plane and it is a mechanical aperture, usually with an adjustable width. The slit preserves one direction of the image, making possible to obtain

spectra from different targets simultaneously. As an disadvantage, the spectra obtained with a slit is sensitive to how the illumination is done.

The fiber is a waveguide that works based on the total internal reflection principle, and so, the spectrograph does not need to be mounted at the telescope. Multi-source spectroscopy is only possible using several fibers or with an integral field unit. If more than one source is within the fiber field of view, the light from all these sources are fed in the detector in the same position, that is to say that the light of the sources inside the field of view of the fiber is scrambled, creating a composite spectrum.

2.1.2 Dispersive elements

The dispersive element can be prisms or gratings. The prism is the classical and the earliest element. The prism is a refracting optical element that acts as a disperser through the effect of differential refraction. The refractive index, n, of the prism varies with the wavelength ($n = n(\lambda)$), and so the components of the light are deviated when passing through the prism according to its wavelength, and following the Snell's law for refraction, assuming that the prism is in the vacuum,

$$\sin(i) = n(\lambda)\sin(r), \tag{2.1}$$

with i the incident angle of the ray to the normal to the surface and r the angle of refraction of the ray to the normal to the surface.

The gratings are composed by many parallel apertures, with space between them similar to the wavelength of the light being observed. Despite its many apertures, it works based on the interference effect produced by only two apertures. One of the most commonly used gratings are the echelle gratings. Echelle gratings are coarse gratings with the blaze angle greatly increased. This combination permits the usage of high orders. An individual order covers a small wavelength range, and it will be overlapped by a short wavelength interval from the next order. To separate these superimposed spectra, a second disperser is used, creating a set of parallel orders on the detector. The second disperser is called cross-disperser.

2.1.3 Detectors

The most common detectors used in Astronomy are the CCDs (Charge-Coupled Devices). The simplest way to explain the CCD operation is to use the "water bucket" analogy when one wants to measure the amount of rain in each point of a mountain (Fig. 2.2). In this analogy each bucket represents one pixel of the CCD, and the raindrops the incoming photons that strike the silicon within the pixel. After the rainstorm, the buckets in each row are moved down the mountain. As the buckets in each column reach the foot of the mountain, they are

emptied in another set of buckets (one for each row of buckets), that carries the rainwater to a metering station for measurement.
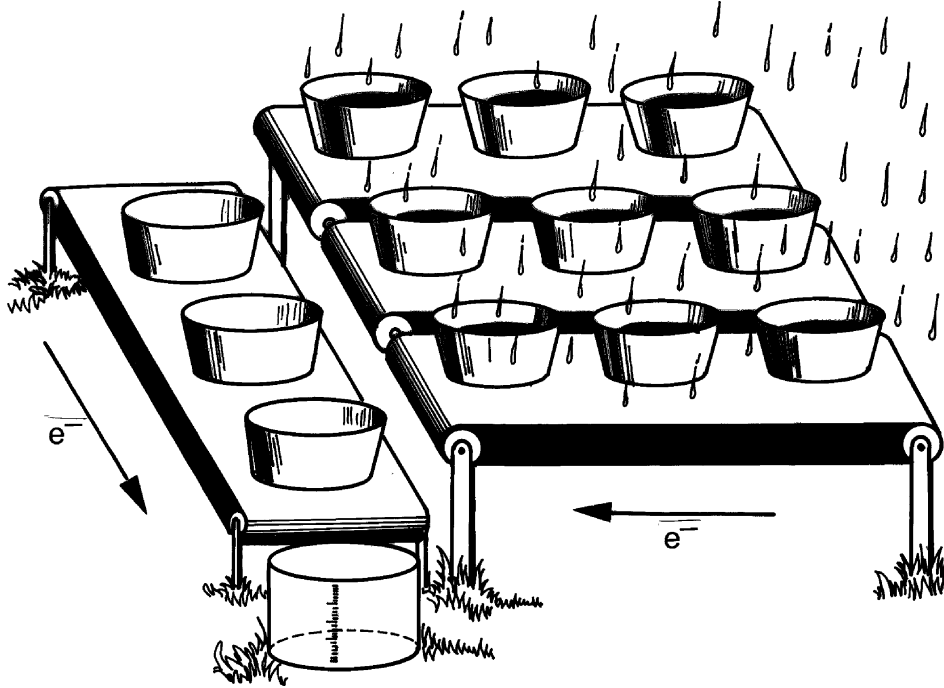
Figure 2.2: Esquematic for CCD "water bucket" analogy (from Janesick 2001).

There are several reasons to use CCDs as detector. Among them one have the low read-out noise, their quantum efficiency, and their band-pass. For more on CCDs, Janesick (2001) or Howell (2006) provide a good start.

2.1.4 HARPS and its context in this thesis

The discovery of an Earth-like planet orbiting a Sun-like star in an one year orbit is an expected benchmark yet to be achieved. One of the future instruments with the capability for such achievement is expected to be available in 2017. Its name is ESPRESSO and it will be placed at the ESO's VLT. ESPRESSO is an high-resolution, fiber-fed and cross-dispersed echelle spectrograph with a resolution of $R = 140000$ for the visible wavelength range (380 nm 800 nm) (Pepe et al. 2010). Its requirement is to reach $10\,\mathrm{cm\,s^{-1}}$, but the aimed goal is to obtain a precision level of few $\mathrm{cm\,s^{-1}}$. It is being optimized for the search of extra-solar planets and thus for the highest radial velocity performance.

As it was mentioned in Cap. 1, at such level of precision sources of noise up to now neglected, can become significant. Because the new generation spectrographs is not available yet, we carried our studies using data from the instrument with more similar characteristics. For the ESPRESSO, that instrument is HARPS (Fig. 2.3).

As ESPRESSO, HARPS (High-Accuracy Radial velocity Planetary Searcher) is a fiber-fed cross-dispersed echelle spectrograph. It has two fibers, one for the target object and the other for calibration. The fiber aperture on sky is 1 arcsec, the same diameter than ESPRESSO's fiber will have. HARPS is also a spectrograph for the visible wavelengths, with a spectral domain ranging from the 380 nm to the 690 nm, with a spectral resolution of 115000. It systematically achieves a precision of better than $1\,\mathrm{m\,s^{-1}}$ (Mayor et al. 2003).

Figure 2.3: The HARPS spectrograph inside the air-conditioned room at La Silla just before being closed and evacuated (from Mayor et al. 2003).

2.2 Cross-correlation function

The Cross-correlation function (CCF) technique used to calculate the RV of a star is a commonly used technique to obtain high precision RV measurements. This technique is being used, as an example, with the spectra taken with ELODIE at the Observatoire de Haute Provence, the CORALIE at the 1.2 m Swiss telescope at La Silla, and HARPS at the 3.6 m also at La Silla.

The CCF technique is well described in Baranne et al. (1996) and it can be defined as the correlation of the stellar spectrum with a binary mask (template spectrum). The non-zero zones of the binary mask correspond to the theoretical positions and widths of the stellar spectral features at zero velocity. The CCF is then computed by shifting the mask as a

function of the Doppler velocity:

$$CCF(v) = \sum_i A[\lambda(i)] \cdot M[\lambda(i)\,(1 + v/c)] \tag{2.2}$$

where $A[\lambda(i)]$ is the spectrum intensity at wavelength $\lambda(i)$, $M[\lambda(i)]$ is the binary mask at the same wavelength, and $M[\lambda(i)\,(1 + v/c)]$ is the mask shifted by a Doppler effect with RV of value v. An illustration of the construction of the CCF is presented in Fig. 2.4.
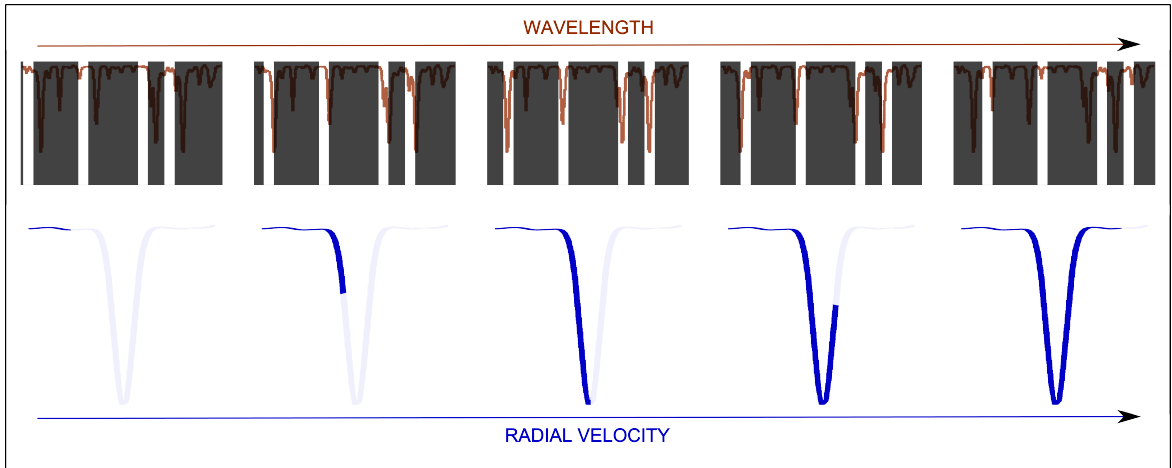
Figure 2.4: Construction of the CCF. As the binary mask is shifted over the spectrum, the CCF the degree of similarity between the mask and the spectrum. It can be seen that the minimum of the CCF (corresponding to the largest degree of similarity) corresponds to the radial velocity where the mask holes are perfectly aligned with the spectral lines they correspond to (from Martins 2013).

Although spectral lines with different depths contain different amount of information, i.e., deep and sharp lines provide more RV information than shallower broad lines, the CCF presented in Eq. 2.2 does not take into account these differences. In order to take this into account, Pepe et al. (2002) presents a new a weighted cross-correlation function $CCF^w(v)$ which accounts for the correct weight of each spectral line contained in the mask:

$$CCF^w(v) = \sum_i A[\lambda(i)] \cdot M[\lambda(i)\,(1 + v/c)] \cdot w_i \tag{2.3}$$

with w_i being the weight of the spectral line $M[\lambda(i)]$, i.e., its own depth.

2.3 Wavelength calibration

The wavelength calibration is an essential part of the RVs determination. A perfect calibrator would be a calibrator that covers the full spectral range of the spectrograph. The calibrator should have a high density of spectral lines, that should be evenly spaced, with homogeneous

intensities close to the saturation. The line width should be smaller than the spectrograph resolution, and the wavelength of the lines should be highly stable and well known. There are several used calibrators. Two common calibrators are the Iodine (I_2) absorption cell and the Thorium-Argon (Th-Ar) lamp. These two are not perfect calibrators. To improve the wavelength calibration, more recently two other calibrator have been developed, tested, and now started to being used. This is the case of the laser frequency combs (LFC) and of the etalons. It this section we briefly describe the wavelength calibration methods.

2.3.1   Th-Ar lamp

The RV calculations from HARPS observations are done using the CCF technique presented in the previous section. This instrument, as its predecessor CORALIE (Baranne et al. 1996), do the wavelength calibration using a Th-Ar lamp reference spectrum. The Th-Ar lamp imprints emission lines along the wavelength domain of the spectrograph. Because HARPS is a very stable spectrograph, with temperature and air pressure drifts below 0.01 K and 0.01 mbar, it usually suffices to take a Th-Ar reference spectrum per night to derive the wavelength solution. To improve the precision one may use the second fiber of the spectrograph to obtain the Th-Ar reference spectrum at the same time that the first fiber is collecting light from the target star. An advantage of this calibration method is its large number and strong emission lines of the Th-Ar lamp. As an disadvantage we point the fact that the Ar lines are dependent on the pressure, and so this lamp can only be used in very stable spectrographs (Lovis & Pepe 2007).

2.3.2   Gas cell

Besides the emission lamp technique, it is also common to use a gas absorption cell as wavelength calibrator. An alternative common absorption gas used is I_2. Several spectrographs are equipped with this technology (e.g. the HIRES spectrograph at the Keck telescope). As the iodine absorption cell can be positioned directly in front of the slit, the spectrum entering the slit is, in fact, the product of the gas cell spectrum and the stellar one. This method allows a precision of $1 - 2\,\mathrm{m\,s^{-1}}$ (Marcy & Butler 1992; Butler et al. 1996). One of the advantages of this method is the common path of the stellar light and the I_2 absorption. The disadvantages of this method include the loss of flux cause by the absorption of the gas cell, and also the fact that the spectral bandwidth is defined by the I_2 absorption band in the visible (500 nm - 620 nm).

2.3.3 Laser frequency combs

The LFC method uses a mode-locked femtosecond-pulsed laser stabilized with an atomic clock to produce a comb-like spectrum of narrow lines, that are much brighter than the ones from the emission lamps. Because the comb-lines must be not only uniformly spaced, but also resolved by the spectrograph, the series of modes produced by the laser are filtered out by a Fabry-Pérot cavity.

Experiments with laboratory prototypes demonstrate that a LFC enables RV measurements with a precision of $1\,\mathrm{cm\,s^{-1}}$ (e.g. Murphy et al. 2007; Li et al. 2008), and tests by Wilken et al. (2012) show the calibration of an astronomical spectrograph with a short-term Doppler shift repeatability of $2.5\,\mathrm{cm\,s^{-1}}$.

2.3.4 Etalons

A Fabry-Pérot interferometer , also called etalon, is an optical resonant cavity that transmits light from a continuum lamp at frequencies that are integer multiples of its free spectral range. The transmitted frequencies by the Fabry-Pérot interferometer are defined by the etalon geometrical properties.

A calibrator system based on a Fabry-Pérot interferometer was built by the Geneva team in collaboration with ESO. Tests with HARPS demonstrated a $10\,\mathrm{cm\,s^{-1}}$ stability over one night and $1\,\mathrm{m\,s^{-1}}$ over 60 days (Wildi et al. 2010, 2011). This technology is also being used in HARPS-N (Cosentino et al. 2012), and is being extended to cover the near infrared to the K band in the frame of the SPIRou project (Wildi et al. 2012).

2.4 Sources of contamination

The RV technique is prone to false positives, i.e., signals created by effects that mimic the presence of a planet. One source of contamination that may mislead to a false planet comes from stellar activity. Although the RV of a stars is defined as the RV of its center of mass, the spectral lines used to measure the Doppler shift are produced in the stellar atmosphere. For pulsating stars or star with active atmospheres, changes may then happen in the spectral line profiles and so the RV measured is not exactly the one from the center of mass of the star. Therefore, if a star presents a variation in the RV, one should also look for changes in the line profiles. In the presence of a planet the RV variations in the host star also show spectral line profiles that are constant in time. On the other hand, the detection of spectral line profiles changes are a clue that we are in the presence of an atmospheric phenomena, instead of a real RV change in the center of mass of the star. By way of example, we can point to the work of

Queloz et al. (2001) in which they present the case of the star *HD 166435*, a star presenting a RV signal with a period of 3.8 days. Photometric data and an analysis to the line profiles indicate that the these variations are consequence of the presence of stellar spot instead of a planetary companion. Many more examples of false positives due to stellar activity can be found in the literature (e.g Huélamo et al. 2008; Figueira et al. 2010a).

Stellar activity features are not the only source of possible contamination. If light coming from a stellar companion enters the fiber it will blend with the target star light and it can contaminate the spectra from the target star. An example of this kind of contamination is that of the binary system composed by the two stars *HD 41004 A* and *HD 41004 B* Santos et al. (2002). The primary star *HD 41004 A* is brighter than its companion by 3.68 mag, and the angular separation between stars is only of $0.5''$. Such small separation made it impossible with the used instrument to separate the light coming from both stars, being the obtained spectra a blend of the two stars. Given the large difference between the magnitudes of the two binary components, the authors did not expect that the *HD 41004 B* spectral component would affect significantly the stellar parameters of the *A* star. Therefore, when the analysis of the RV revealed a 1.3 days period variation, with an amplitude of $50\,\mathrm{m\,s^{-1}}$, the first hypothesis was that it was due to the presence of a $0.25\,M_J$ planetary companion around the primary star of the binary system. However, after further analysis to the RV, line profiles, and photometric data, the authors concluded that the presence of a brown dwarf around the *HD 41004 B* was the best explanation for the observations.

2.4.1 Earth's atmosphere

Transparent to our eyes, one may sometimes forget that Earth's atmosphere surrounds us. Although essential for life in this planet, and therefore for our existence, it can be an obstacle when it comes to ground-based astronomical observations. Earth's atmosphere can affect ground-based observations in several ways, and this subsection is reserved to its effects.

Astronomical observations are prone to contamination due to Earth's atmosphere. A simple example is the refraction of the starlight in the different layers of the atmosphere, which have different temperatures and pressure values, makes the direction of the star under observation not the true direction: the apparent altitude of the star is changed.

The absorption by the atmosphere is other aspect to take into account. Earth's atmosphere is composed of several molecules and atoms, such as N_2 , O_2, A, CO_2, Ne, He, CH_4, Kr, H_2, N_2O, CO, H_2O, O_3, and other gases. These molecules, atoms and gases absorb radiation along almost all the atmospheric spectra. In the Ultraviolet (UV), the absorption by the molecules and atoms (essentially the absorption by O_3), and the Rayeigh scattering (in a very simple way, the Rayleigh scattering tells us that the scattering is proportional to λ^{-4},
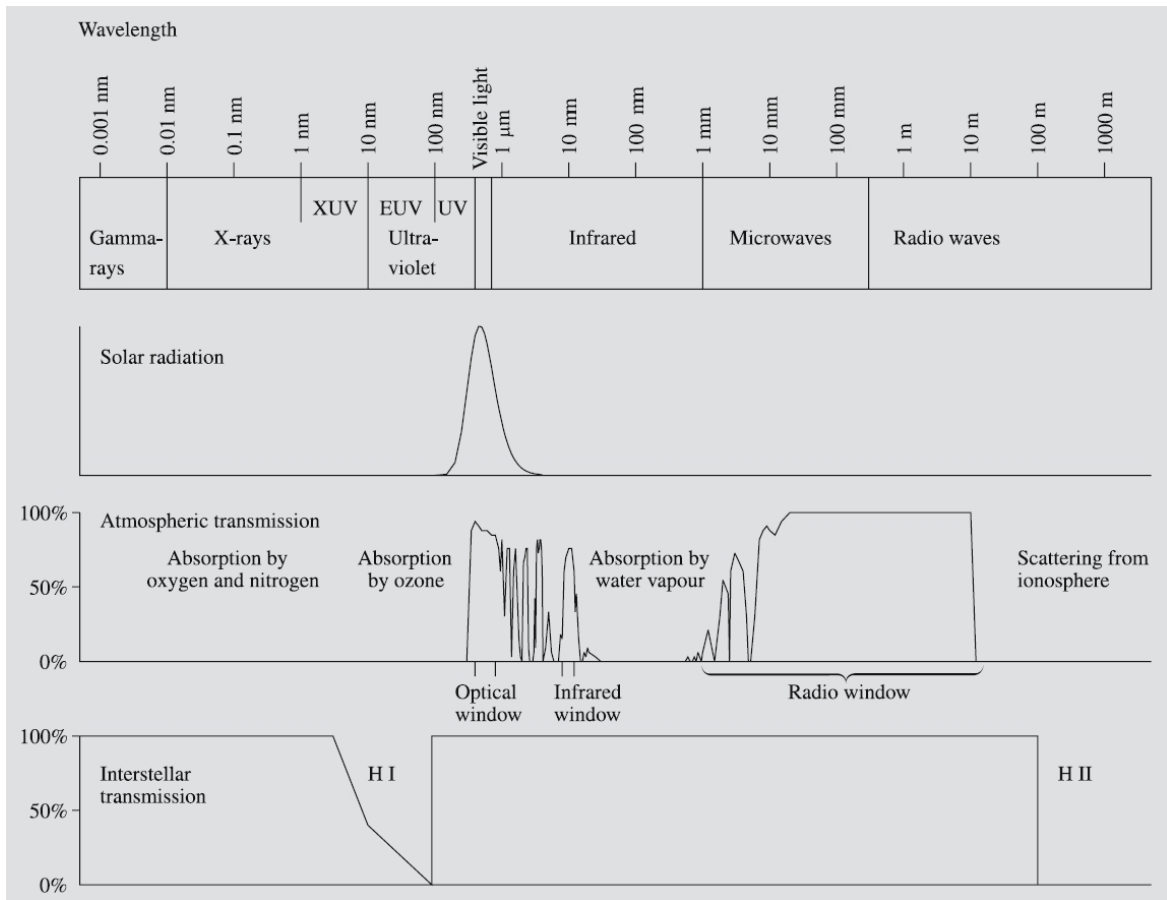
Figure 2.5: Earth's atmospheric transmission. 100 % transmission means that the atmosphere is completely transparent and all the radiation reaches Earth's surface, and a 0 % transmission means that the absorption is total and the atmosphere is completely opaque (from Karttunen et al. 2007).

i.e., shorter wavelengths – such as UVs – are scattered more strongly than longer ones) causes a complete opacity of the atmosphere for $\lambda < 300$ nm. Because the O_3 is concentrated around the 48 km above the sea level (near the stratopause), ground-based UV observations are infeasible (Fig.2.5).

At the visible wavelengths there is little absorption of the electromagnetic spectrum, making it one of the best windows for ground-based observations. After all, did not we all made our first "astronomical observation" by stargazing with the naked eye?

In the Infrared (IR) Earth's atmosphere becomes, once again, problematic for ground-based observations. At these wavelengths there are some regions in which the atmosphere is almost completely opaque and in some other regions it has an high transmission. These high transmission windows are enough to allow ground-based observation in the IR.

Looking at Fig. 2.5, one can see that only in the major part of the radio window the transmission is total. For the other atmospheric windows in which ground-based observations are

Table 2.1: Common band-passes in the visible (UBVRI), near-infrared (JHKLM), and mid-infrared (NQ) (from Chromey 2010).

Band	Central wavelength (μm)	Width (μm)
U	0.365	0.068
B	0.44	0.098
V	0.55	0.089
R	0.70	0.22
I	0.90	0.24
J	1.25	0.38
H	1.63	0.31
K	2.2	0.48
L	3.4	0.70
M	5.0	1.123
N	10.2	4.31
Q	21.0	8

possible, there is always some atmospheric extinction. The atmospheric extinction may be described by the Beer-Lambert-Bouguer law:

$$I(z) = I_0 e^{-\tau_0 \sec z}, \tag{2.4}$$

where z is the zenith angle. The intensity of the light that passes through the atmosphere ($I(z)$) will depend on the airmass of the observation ($\sec z$), and on a parameter τ_0 which is basically the optical depth, and it is dependent of several conditions, such as the scattering by aerosols (salt, dust, industrial pollution,...), Rayleigh scattering, and the absorption by O_3, O_2, CO_2, and water vapor. In other words, the atmospheric extinction is time and site dependent. As an example, because the water vapor is essentially concentrated in the layers of the atmosphere up to 5 km above the sea level, one can observe from high altitude observatories to minimize the effects of the water vapor in the IR wavelengths.

To control observations, in particular, to control contamination from the opaque windows of the IR, astronomers have created filters/band-passes to restrict the range of a detector's sensitivity. There are many band-passes systems and variation of the same band-pass system. For reference, Table 2.1 is presented, showing the central wavelength and the bandwidth of the Johnson-Cousins-Glass system, which is a commonly used system.

The atmosphere affects both photometric and spectroscopic observations. There are some features in the atmospheric spectrum that are imprinted in the astronomical spectra taken from Earth's surface. In the visible, these features come from the H_2O and O_2 and may be a source of contamination and should not be neglected. This is particularly true for high precision radial velocities measurements, as will be discussed in Cap. 4. Currently, RV

calculations already have in attention the telluric lines and correct for them. To minimize the effect of this contamination on RV computation, 3 of the 72 HARPS spectral orders, the ones in which the deeper telluric lines are present, are neglected in the RV calculations (Mayor et al. 2003). Moreover, in the other spectral orders with deep telluric lines and/or strong blended lines, stellar masks used in the CCF take into consideration only a very few stellar lines (Baranne et al. 1996; Pepe et al. 2002). But as the S/N of the spectra increases and the calibration methods are improved, the relative impact of shallow, not-neglected telluric lines, here designated as micro-telluric lines, will become larger. Therefore, it becomes urgent to explore how to study the impact of these telluric lines of smaller depth, and correct their effect in the RV calculation.

Other effect of the telluric atmosphere is the scintillation of the stars, that can even be observed with just the naked eye. The observed scintillation is due to the turbulence resulting from the unsteadiness of the atmospheric layers with different temperatures and densities. This phenomenon is called seeing and it limits the angular resolution of a large telescope. The effect of the seeing results in an speckle pattern image instead of the ideal diffraction pattern with a strong central peak. On long exposure observations, the speckles will be averaged producing a "seeing disc". The FWHM (full width half maximum) of the seeing disk gives us the seeing value. There are techniques to compensate for the seeing effect, like AO, but this is not subject of this thesis. The lower values for the seeing are around a few tenths of arcsec, and on the other extreme it can reach the several tens of arcsec. With respect to photometry, the smaller the seeing the better. When it comes to spectroscopy, this may not be entirely true. To minimize the effects of possible spots or other features in the photosphere of the star in the calculations of RVs, one wants the obtained stellar spectrum to be an average spectrum of all the stellar disk. If the seeing is to small, the resulting spectrum may be to focused in just part of the star. One the other hand, is the seeing is to high, there may be loss of flux and/or contamination by a background/foreground source.

Chapter 3

Impact of stellar companions within the fiber

3.1 Introduction

As we have seen earlier in this work, the fact that the RV technique is prone to false positives and one should be extremely careful about signals that can mimic the presence of a planetary companion. With the advent of very high precision spectrographs, such as ESPRESSO or CODEX (Pepe et al. 2010), the RV precision enters a new domain, that of the $\mathrm{cm\,s^{-1}}$, which in turn will increase the quality of our characterization of these unwanted yet ubiquitous signals (e.g. Cegla et al. 2012). As part of this thesis, we address the so far unexplored mechanism capable of distorting RV signals and creating false ones, that was mention in Sect. 2.4: the contamination of the main spectrum by that of an unresolved or/and undetectable companion. We consider two different possibilities:

1. that of a faint gravitationally bounded companion; and

2. that of an unbounded star that is aligned with the target at the moment of observation.

We assumed the target stars to be placed at the Galactic disk edge to consider a representative case that encompasses several scenarios of contaminant stars. We used real high signal-to-noise ratio (S/N) observations obtained with HARPS to create the composite spectra and process these with RV pipeline to evaluate the impact of the contamination in the most realistic way possible. While we aim at characterizing this effect down to the precision level of ESPRESSO, $10\,\mathrm{cm\,s^{-1}}$, it can be assessed at an even lower precision level.

Although this study is performed to characterize the impact on the RV when using the CCF, point spread function modeling will also be affected by stellar companions, in a different way.

The results of this study are particularly interesting for deep surveys in crowded fields, such as Kepler surveys.

If the RV of the companion star (contaminant) remains constant, i.e., the spectral lines of the companion have the same wavelength in every spectra, its contamination will also be constant in time. In this case, the contamination caused by the stellar blends will be undetectable in the RV calculation. However, if the contaminant RV is changing, if there is a variation of the seeing, or if there are guiding variations during observations, the effect of the contamination will no longer be constant and it may mimic the signal due to an extra-solar planet, as it was the case of the planet around the *HD 41004 A* (Santos et al. 2002) presented in Sect. 2.4. Another example is WASP-9b, which was discarded as a planet after it was discovered that the signal was due to a fortuitous alignment (Triaud, priv. comm.).

3.2 Contaminant cases

When one chooses a target star to observe, we want to observe that star alone. However, without the knowledge of the observer, a secondary star may be present. This secondary star may become source of contamination in the calculation of the chosen star RV. These secondary/contaminant stars may appear as two different types: physical binaries or fortuitous alignments.

3.2.1 Real Binaries

In the physical binaries the target star is gravitationally bounded to the contaminant one. In this section we present the probability distributions of the physical binary properties that we use in our work. For the G- and K primaries we based our study on the results of Duquennoy & Mayor (1991), who studied the multiplicity among solar type stars in the solar neighborhood. They considered a sub-sample of 146 primary stars with spectral types between F7 and G9. Using Table 7 of Duquennoy & Mayor (1991) on the mass-ratio distribution among G-dwarfs binaries, we can calculate the probability of observing a binary with a mass-ratio $q = M_2/M_1$, where M_2 represents the mass of the secondary star and M_1 is the mass of the primary. These probabilities are shown in Table 3.1. There we can see that there is a maximum probability for the mass-ration range $]0.2, 0.3]$. The distribution of orbital periods (P) of their study is approximated to a Gaussian with $\overline{\log P} = 4.8$ and $\sigma_{\log P} = 2.3$.

Duquennoy & Mayor (1991) also presented the eccentricity distribution por $P < 1000$ and $P > 1000$ days, shown here in Table 3.2.

We stress that there is a large uncertainty for very low mass companions (VLMC) binaries

Table 3.1: Probability of observing a binary with a mass-ratio $q = M_2/M_1$ among G-dwarfs binaries for periods $P < 10^4$ days and $P < 10^4$

q_{max}	0.1	0.2	0.3	0.4	0.5	0.6	0.7	0.8	0.9	1.0	1.1
	$P < 10^4 days$										
P(q) [%]	12.0	16.3	13.1	12.7	12.3	12.9	6.5	1.9	2.6	3.4	6.2
	$P > 10^4 days$										
P(q) [%]	11.1	11.9	18.4	15.8	10.5	11.2	6.6	6.6	4.0	4.0	0
	Total										
P(q) [%]	11.4	13.6	16.4	14.6	11.2	11.8	6.5	4.8	3.4	3.8	2.4

Note: from Duquennoy & Mayor (1991).

Table 3.2: Probability of observing a binary with an eccentricity e among G-dwarfs binaries for periods $P < 10^3$ days and $P < 10^3$ (from Duquennoy & Mayor 1991).

e_{max}	0.15	0.3	0.45	0.6	0.75	0.9	1
	$P < 10^3 days$						
P(e) [%]	12.50	43.75	31.25	6.25	6.25	0.0	0.0
	$P > 10^3 days$						
P(e) [%]	5.88	11.76	23.53	14.71	20.59	23.53	0.0

(with $q < 0.1$), and that in this study it is not included values of q below 0.01. We also emphasize that this mass ratio distribution is calculated for binary stars, but we recall that, also according to Duquennoy & Mayor (1991), there are 57% of binary systems with a mass ratio higher than 0.1, and 43% of apparently single stars. Of these 43%, $(8 \pm 6)\%$ most probably have a VLMC, which puts the percentage of single stars at $\sim 30\%$.

Table 3.3: Probability of observing an M-dwarf binary with a mass ratio $q = M_2/M_1$ (from Janson et al. 2012).

q_{max}	0.1	0.2	0.3	0.4	0.5	0.6	0.7	0.8	0.9	1.0
P(q) [%]	0.0	1.61	5.95	10.45	12.93	13.84	14.48	13.03	14.58	13.13

For dwarf stars of spectral type M we used the distributions of mass, q, and of semi-major axis, a, from the work of Janson et al. (2012) on M-dwarf multiplicity. The authors suggest an M-dwarf total multiplicity fraction of 34%. Table 3.3 shows the probability of observing an M-dwarf binary with a mass ratio q. Janson et al. (2012) found a uniform distribution to be more consistent with the mass ratio of their observed sample, than a rising distribution. Accordingly, we assumed their uniform distribution in our work. For the semi-major axis distribution Janson et al. (2012) also compared the Sun-like and the narrow distribution, finding the latter to be more consistent with their sample. We therefore used this distribution, which is shown in Table 3.4. As no information was given on the eccentricity distribution for M-dwarf binaries, we assumed the distribution from Duquennoy & Mayor (1991).

Table 3.4: Probability of observing an M-dwarf binary with a certain $\log a$ (from Janson et al. 2012).

$\log a_{max}$	0.25	0.5	0.75	1.	1.25	1.5	1.75	2.	2.25	2.5
$\mathbf{P}(\log a)$ [%]	0.51	2.60	9.02	15.39	17.13	17.65	14.73	11.74	7.85	3.37

3.2.2 Fortuitous alignment

Even if the target star is a single star, a fortuitous alignment with a background/foreground object may occur. To study the probability of such an event we used the Besançon model (Robin et al. 2003). This model allows one to compute the stellar population density on a given direction of our Galaxy, permitting one to infer the most probable contaminants and their probability. To do so, we simulated an observation[1] of the *HD 85512* coordinates - $(l, b) = (271.6759, 8.1599)$ - which is positioned at the border of the Galactic disk. We also considered a distance interval of $50\,kpc$ (approximately the diameter of the Milky Way), magnitudes between 0 and 30, and a solid angle for a radius of $3°$. The purpose of these parameters was to have a large number of stars for each bin of magnitude an spectral type and then to divide it by the ratio between the considered area and that of the HARPS fiber (radius of $0.5\,arcsec$), thus obtaining the density of stars, i.e., the probability to have a fortuitous alignment within the HARPS fiber. In Fig. 3.1 we present a contour plot of the total number of stars obtained in the simulation for each bin of magnitude and spectral type. The most probable contaminants for the accidental alignments are shown in Table 3.5.

Table 3.5: Most probable contaminants for the fortuitous alignments.

Spectral type	$\mathbf{m}_V$	$\mathbf{P}$ [%]
$[F0, F5[$	$[13, 16] \wedge [20, 23]$	0.08
$[F5, G0[$	$[13, 24]$	1.25
$[G0, G5[$	$[13, 25]$	1.74
$[G5, K0[$	$[13, 25]$	1.32
$[K0, K5[$	$[12, 26]$	2.5
$[K5, M0[$	$[16, 30]$	4.48
$[M0, M5[$	$[17, 30]$	16.99
$[M5, M8[$	$[20, 30]$	12.12
$[M8, M9]$	$[21, 30]$	13.17

3.3 Data

We considered target stars from spectral type G to late M, with visual magnitudes, m_v, between 5 and 15. As described in the previous section (Sect. 3.2.2), the most probable

---

[1] using the model form available at http://model.obs-besancon.fr/
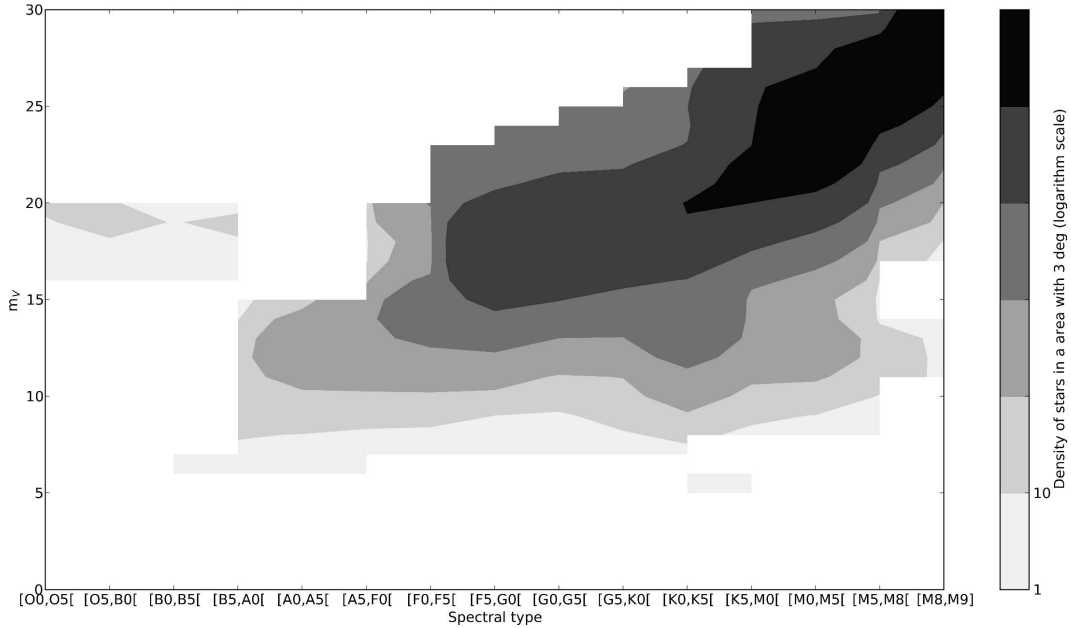
Figure 3.1: Number of stars in each bin of spectral type and magnitude (radius of $3°$).

contaminant stars are of spectral types FGKM. To represent both target and contaminant spectral types, we chose spectra from nine stars, which are shown in Table B.1.

Table 3.6: Stars used in our simulations, their spectral type, visual magnitude (m_v) and S/N at the center of the spectral order 50 (SN50) [1].

Object	Spec.Type	m_v[2]	SN50
HD20852	F2	6.92	225; 98
HD103774	F5	7.12	102; 146
Sun	G2	3.65 [3]	225; 260
Tau Ceti	G8	3.50	300; 450
HD69830	K0	5.95	253; 380
Alpha Cen B	K1	1.33	385; 399; 302
HD85512	K5	7.65	156; 86
Gl436	M1	10.68	15; 31; 46
Gl581	M3	10.57	37; 22

[1]the observations were taken under the Program IDs: 086.C-0284(A), 084.C-0229(A), 087.C-0990(A), 183.C-0972(A), 183.C-0437(A), 085.C-0019(A), 072.C-0488(E), 088.C-0011(A), and 082.C-0718(B)
[2] from Simbad (http:simbad.u-strasbg.fr/simbad/sim-fid)
[3] m_v of the moon within the HARPS 0.5" radius fiber.

We used spectra with an S/N at the center of the spectral order number 50 (which corresponds to a wavelength of 437.28 nm), varying between 15 to represent a star of spectral type M, and 450 for a G-star. The S/N values of these spectra can be found in Table 3.6. The stars were chosen because they had the highest S/N in their spectral type range, as observed with HARPS.

25

3.4 Method

The goal of this study is to characterize a possible stellar contamination of the target star. To do so, we co-added target and contaminant spectra. We not only considered contaminant stars of spectral types F2, F5, G2, G8, K0/K1, K5, M1, and M3, but also different ratios of magnitude between target star and contaminant, as well as differences in RV. To sum two spectra with these particular conditions is not trivial. We need to control the magnitudes and RVs.

We set the magnitude V of the target (m_t) star according to the data available in Simbad [2] and then calculated the magnitude of the contaminant (m_c) with respect to the target star using the apparent magnitude - flux relation

$$m_t - m_c = -2.5 \times \log(F_t/F_c) \,, \tag{3.1}$$

where F_t and F_c are the fluxes of the target and of the contaminant. The magnitudes are now calibrated and can be changed by multiplying the flux by a factor of

$$f = 10^{-x/2.5}, \tag{3.2}$$

where x is the difference between the new chosen magnitude and the true magnitude of the star in the target-star system.

We also considered the relative RV between the two spectra as a tunable knob. However, when processing our spectra using the HARPS pipeline the reduction takes into account the header (and properties) of the parent spectra. To overcome this situation, we first need to replace the header of the contaminant spectrum file with that from the target, and then run the cross correlation function (CCF) recipe of the RV pipeline in order to obtain the contaminant RV in the target star reference frame. The next step in this process is to shift the contaminant spectra. To assess by how much the contaminant spectra had to be shifted, we used equation 3.3

$$\lambda_c = \lambda_t \times \left(1 + \left(\frac{RVC_c' - RVC_t - \Delta RV}{c} \right) \right) \,, \tag{3.3}$$

where λ_c are the new wavelengths to derive the desired ΔRV (difference between the RV of the target and the contaminant), λ_t are the wavelengths from the wave file corresponding to the target, and c is the light speed in vacuum. These new wavelengths were used to calculate, by linear interpolation, the number of pixels by which the contaminant needed to be shifted. This gives a new xx axis that it was used, recurring to another linear interpolation, to shift the contaminant spectra. Now that we we have the control over the target and contaminant

---

[2]http://simbad.u-strasbg.fr/simbad/sim-fid

RVs, the next step is the sum of the target with the modified contaminant spectra, which is the sum of their fluxes. The shift of the contaminant spectra should not be larger that the maximum barycentric Earth radial velocity (BERVMX) of the star, otherwise there is the risk that the spectral lines enter and leave the orders when performing the CCF calculation. BERVMX defines the excluded spectral lines from the correlation due to the orbital movement of the Earth toward the star. Our goal is to introduce a shift equivalent to a BERV value lower than the |BERVMX|, so that we do not need to exclude new lines.

We then co-added the target spectrum with the modified contaminant spectra and processed the result with the HARPS RV pipeline.

3.4.1 The "real binaries" stars simulation strategy

To study the impact of a companion on the RV calculation of a binary primary star, we reproduced the cases discussed in the work of Duquennoy & Mayor (1991). We considered a primary G2 (the Sun) star with six different secondary/contaminant stars: G2 (Sun), G8 (Tau Ceti), K1 (Alpha Cen B), K5 ($HD\,85512$), M1 ($Gl\,436$), and M3 ($Gl\,581$).

The first case had a G2 star (the Sun) as contaminant with positive and negative values of $\Delta RV = RVC'_c - RVC_t$, where RVC_t is the target barycentric radial velocity (drift corrected) without contamination, and RVC'_c is the contaminant barycentric radial velocity (drift corrected) in the target reference frame. In Fig. 3.2 we show the impact, $RVC_t - RVC'_t$, of the stellar companion on the target RV, where RVC'_t is the target barycentric radial velocity (drift corrected) with contamination. We can see that symmetrical shifts of the contaminant lead to symmetrical contamination values. Therefore, from now on we work with absolute values.

For each target-contaminant pair we considered a range of $|\Delta RV|$ between 0 and $30\,\mathrm{km\,s^{-1}}$ (in steps of $1\,\mathrm{km\,s^{-1}}$), except for a secondary star of spectral type K5 in which the maximum $|\Delta RV|$ was of $24\,\mathrm{km\,s^{-1}}$.

3.4.2 Fortuitous alignment simulation strategy

The fortuitous alignment case is more generic. Here we considered six spectral types of primary stars (G2, G8, K0, K5, M1, and M3) in combination with the eight spectral types as contaminants – the same six used as target stars plus an F2 (HD20852) and an F5 (HD103774) star. For each spectral type of primary stars we considered contaminants with magnitudes m_v between 5 and 15 (in steps of one). The contaminants considered were those described in Table 3.5.
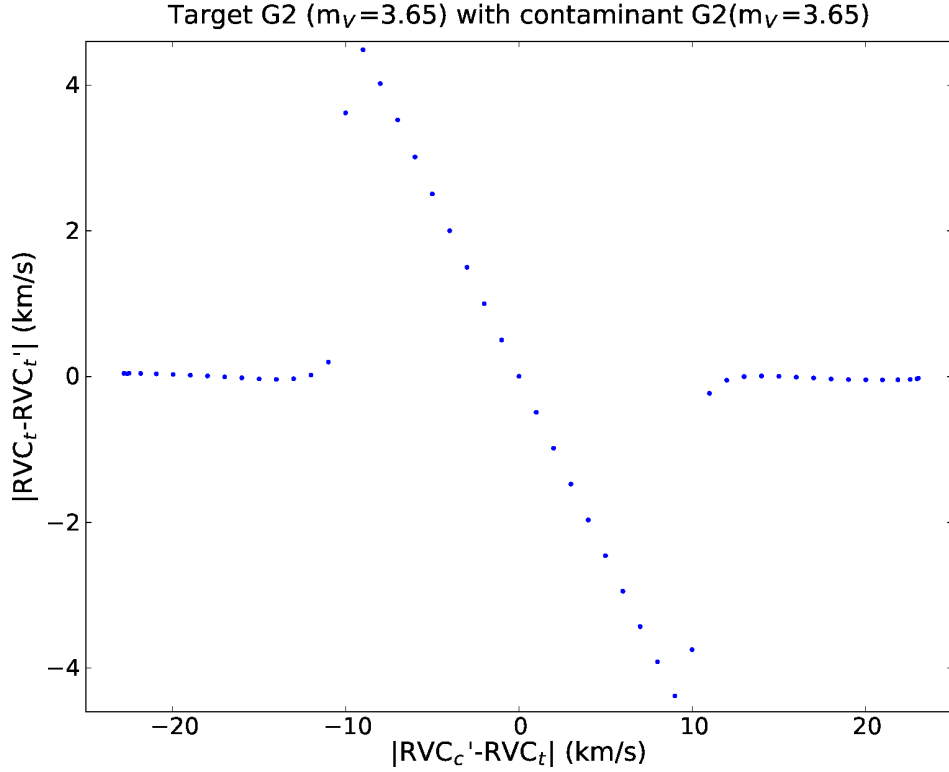
Figure 3.2: Shift of a G2 target RV caused by a contaminant of the same spectral type and magnitude, m_v, in function of the difference between individual radial velocities.

Although the Besançon model includes oxygen and carbon AGB (asymptotic giant branch) stars and white dwarfs in the search, we only considered main-sequence (MS) stars. Very metal-poor stars were also excluded from our study. For an M1 target star a K0 star (HD69680) was used instead of the K1 mentioned above. This was because the barycentric Earth radial velocity (BERV) value from the K1 star did not allow the desired shift in RV. For each target-contaminant pair we considered the differences between its RV, $|\Delta RV|$, under $20\,\mathrm{km\,s^{-1}}$, which is half the width of the CCF window. Although giant stars will often be contaminant stars, we assumed that spectra from MS stars are similar to those of giants and only used spectra of MS stars in our simulations.

3.5 Results

3.5.1 Real Binaries

The results for the contamination by a secondary star of a binary system, in which the primary star is of spectral type G2, as a function of ΔRV can be found in Fig. 3.3. As one would expect, the impact on the RV calculation depends on the difference between the RVs
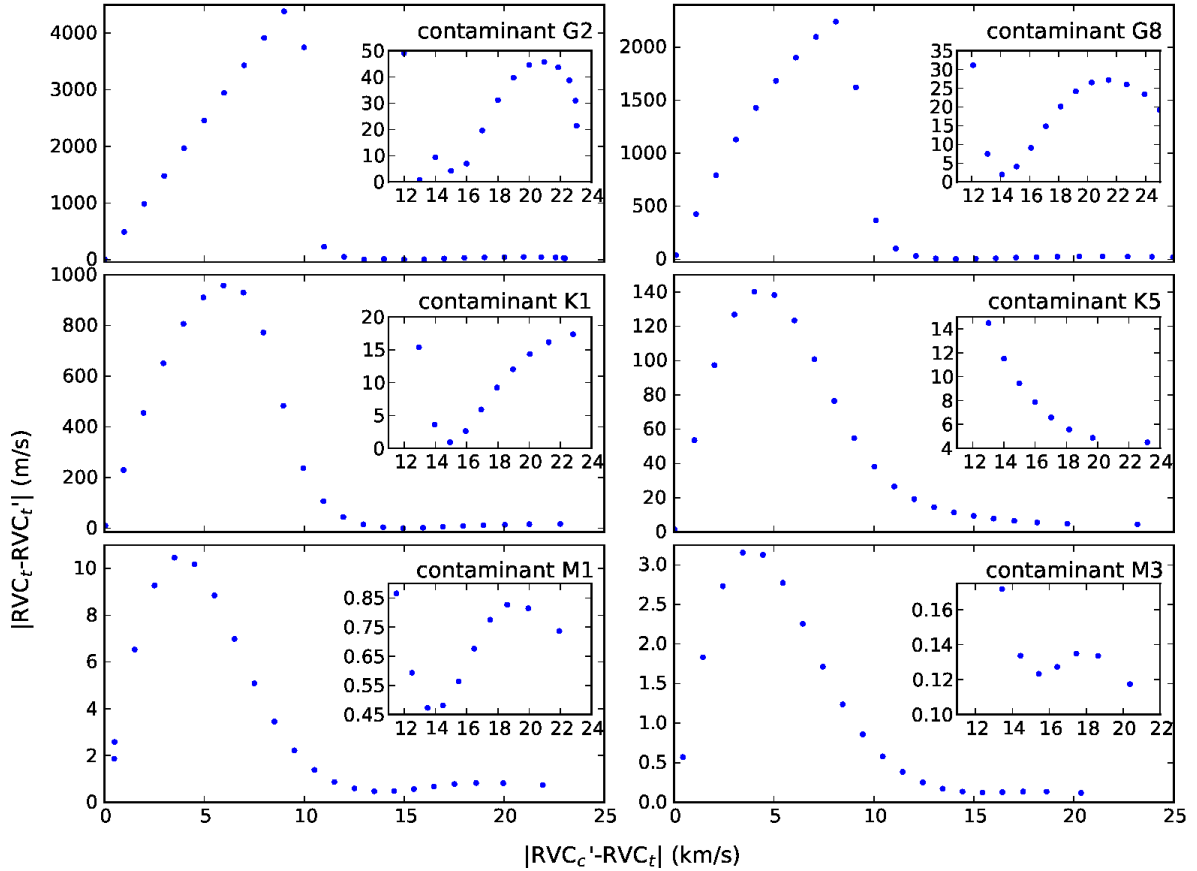
Figure 3.3: Impact on the RV of a G2 target star caused by a companion of spectral type G2, G8, K1, K5, M1, and M3 (left to right, top to bottom). For each case a close-up with a bump for the impact for $10 < \Delta RV < 24\,\mathrm{km\,s^{-1}}$ is shown.

of target and contaminant RV stars (ΔRV). As seen in Sect. 2.2, one can interpret a CCF curve as an "average" line of the spectrum, that is fitted by a Gaussian curve to measure the center of the CCF. In the presence of a secondary star, the CCF is composed by two curves. For $\Delta RV = 0$ the two curves fully overlap, and so the impact of the contaminant on the Gaussian fit, and consequent RV calculation is minimum. As the ΔRV increases, the impact of the secondary star on the Gaussian fit also increases until the point when the two CCF curves overlap, with the contaminant RV, $|RVC_c'|$, close to 0.6 times the FWHM of the target CCF. When the curves become distinct, the impact on the measured RV of the primary star decreases. For $|\Delta RV| > 20\,\mathrm{km\,s^{-1}}$ the peak of the contaminant CCF curve moves out the CCF window (we used the default value for the CCF window which is of $40\,\mathrm{km\,s^{-1}}$), and for values of $|\Delta RV| > 25\,\mathrm{km\,s^{-1}}$ the CCF curve of the contaminant star completely exits the CCF window of the target. Nevertheless, the contamination is not null. There are bumps, still inside the correlation window, in the wing of the CCF curve that slightly contaminate the target spectra.

Figure 3.4 shows the maximum contamination for each type of contaminant. We can see that the biggest maximum contamination of $\sim 4.5\,\mathrm{km\,s^{-1}}$ occurs in the case for which the companion star is of the same spectral type. This is also the case for which the companion star have the smallest magnitude value of $m_v = 3.7$, that is to say, the case for which the companion is brightest. On the other side, the lowest maximum contamination ($\sim 3.15\,\mathrm{m\,s^{-1}}$) occurs for a companion/contaminant star of spectral type M3 and has a magnitude of only $m_v = 9.2$. In short, as the secondary stars become fainter and of later spectral type, the maximum contamination decreases.
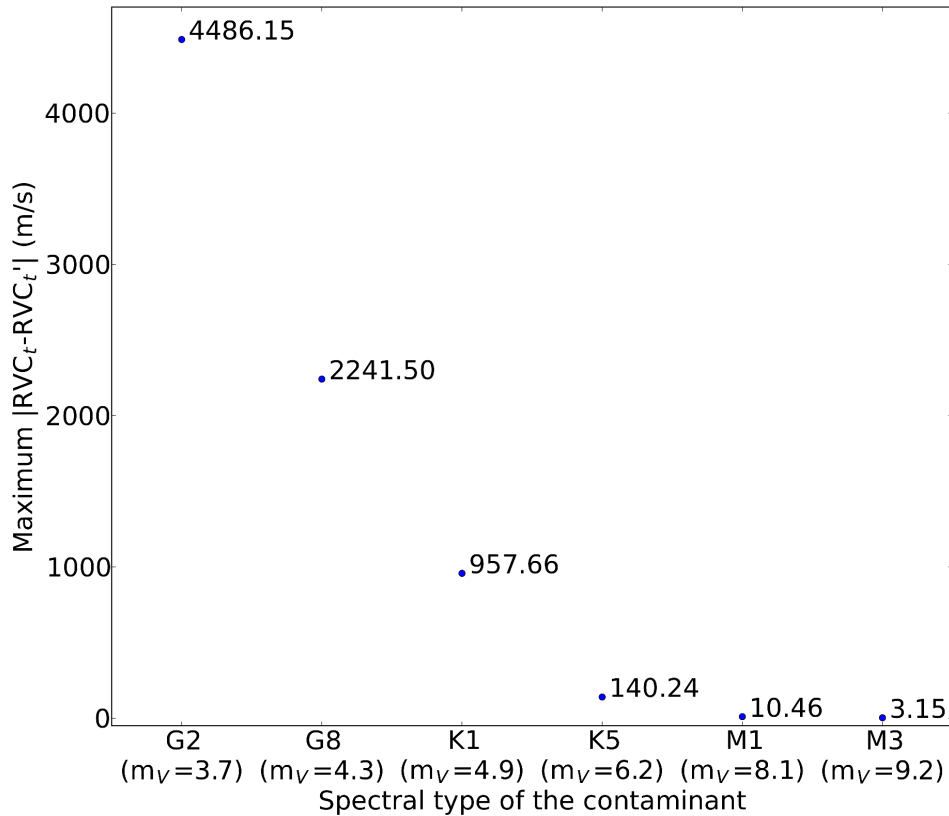
Figure 3.4: Maximum contamination of a G2 target star caused by each companion spectral type in $\mathrm{m\,s^{-1}}$.

3.5.2 Contamination by the sky

The sky is not completely dark and most of its light results from the reflection and scattering of the Sun spectrum. The sky brightness has a magnitude per $arcsec^2$ in the V band of 21.8 on a new-moon night, and of 20.0 on a full-moon night. To study the impact of the sky contamination on the target star RV we assumed that the sky spectrum is the solar one. This is equivalent to say that for a fiber of $0.5''$ radius, we have a systematic contamination of a G2 star with $m_v \sim 20$ on a full-moon night to a limit of a G2 star with $m_v \sim 22$ (new-moon). The

results of the maximum contamination by the sky brightness study are shown in Fig. 3.5. We
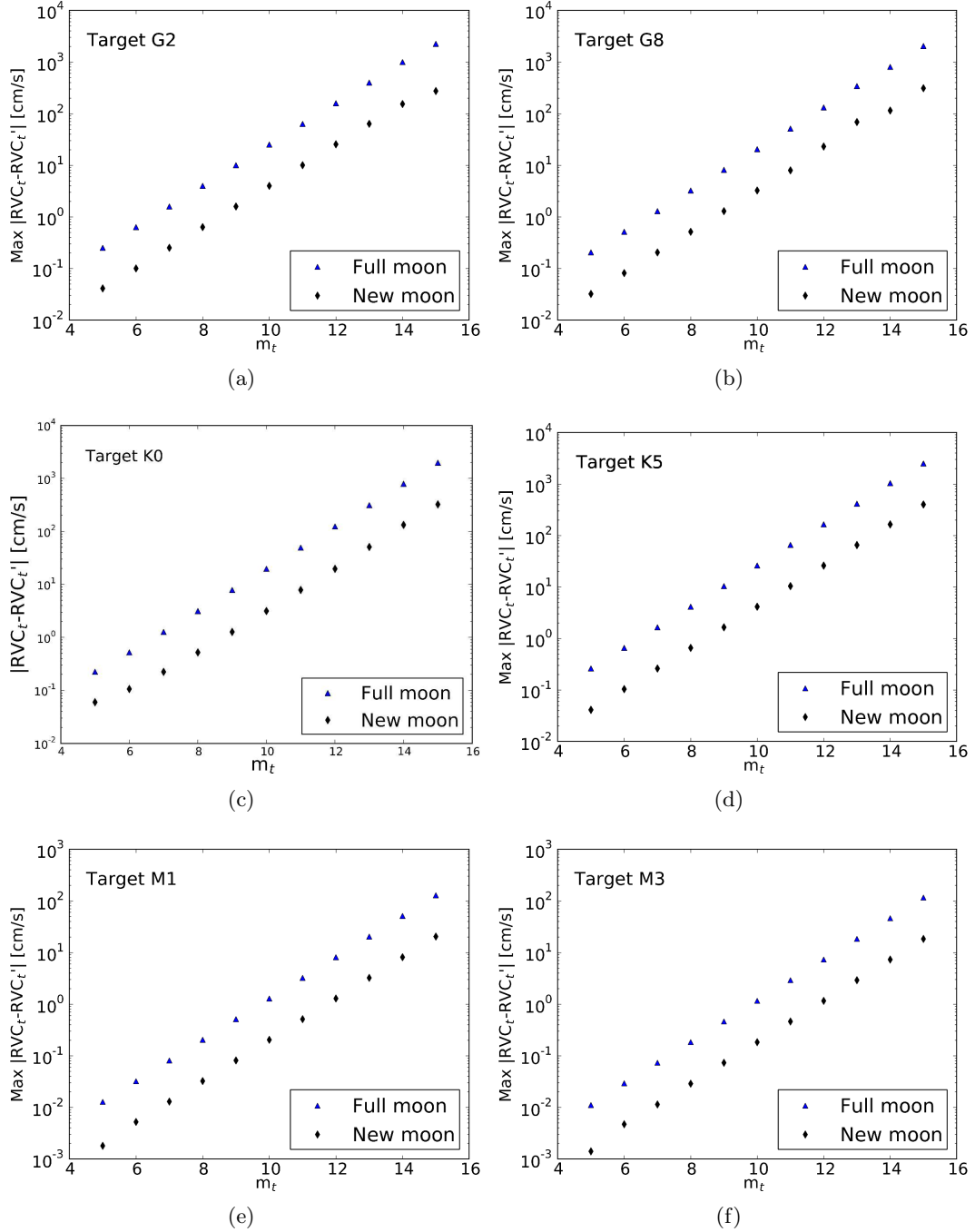
Figure 3.5: Maximum contamination of the sky brightness on a **a)** G2, **b)** G8, **c)** K0, **d)** K5, **e)** M1, and **f)** M3 target star spectra. The blue triangles show the impact on the RV caused by the sky brightness on a full-moon night, while black diamonds show the impact on a new-moon night.

can see that that when observing a a G2, G8, K0, or a K5 target star fainter than $m_v = 11$, or a M1, or M3 fainter than $m_v = 14$, the errors induced on the measured RV can be larger

31

than $10\,\mathrm{cm\,s^{-1}}$, which can become a problem for future instruments such as ESPRESSO. For a night of observation with a full-moon, induced errors become larger than $10\,\mathrm{cm\,s^{-1}}$ for G- and K target stars fainter than $m_v = 9$ and for an M star fainter than $m_v = 12$.

3.5.3 Fortuitous alignment

Here we present a more exhaustive study of all the possible sources of stellar contamination. Beyond having the moon as a contaminant, or the possibility of the target star to be part of an (unknown) binary system, there is a vast range of possible contaminants as was discussed in Sect. 3.2.2. Our study is made simpler because our analysis holds for similar spectra with different absolute values of magnitude for target and contaminant star, but with the same difference between them ($\Delta m = m_c - m_t$)), as we can see from Fig.3.6. This way, we only
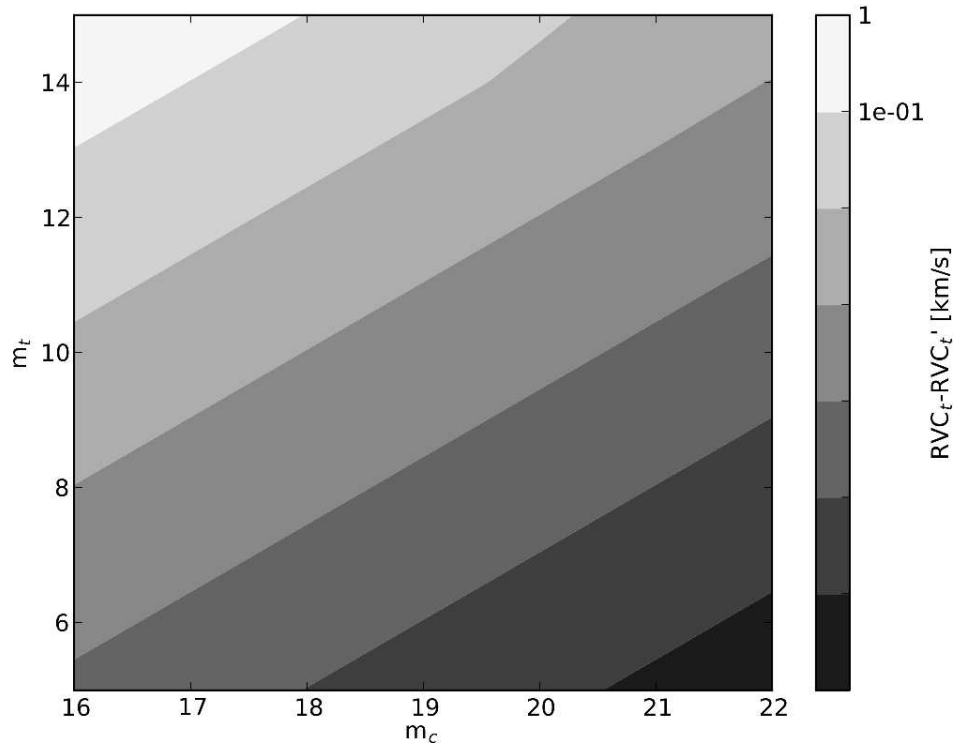
Figure 3.6: Contour plot of the maximum induced RV shift in the target $|RVC_t - RVC_t'|$ depending on the target (m_t) and contaminant (m_c) magnitudes.

carried out our study on the impact of a fortuitous alignment for a star in which m_v differs $|\Delta m|$ from the contaminant star. The result of our study for contamination as a function of spectral type is shown in Fig. 3.7.

We first note that t there is a clearly defined relation between Δm and the maximum of contamination, except for some cases where the difference in magnitude between target and contaminant star is null, i. e., when target and contaminant have the same magnitude. A
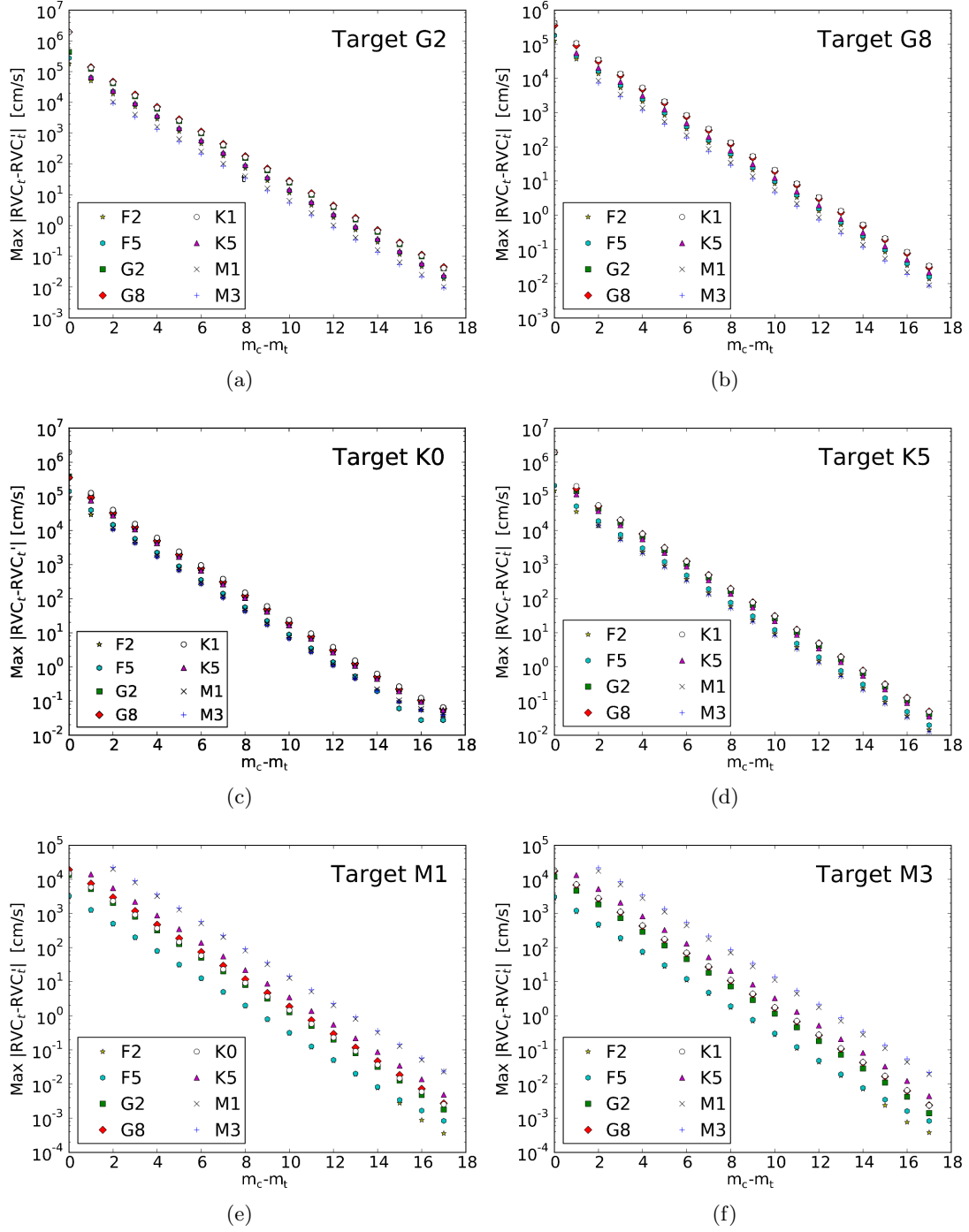
Figure 3.7: Maximum impact of $|\Delta m|$ on the $|RVC_t|$ for a target star of spectral type **a)** G2, **b)** G8, **c)** K0, **d)** K5, **e)** M1, and **f)** M3, and contaminants of spectral types F2 (star), F5 (hexagon), G2 (squares), G8 (diamonds), K1 (circles), K5 (triangles), M1 (x crosses), and M3 (+ crosses).

misidentification of the contaminant correlation peak with that of the target star may happen due to a (slightly) larger contrast. If we consider only values of $\Delta m > 1$, we can describe the

relation between the Δm and the maximum of the contamination induced by a contaminant within the fiber star in the RV calculation as

$$\mathrm{Max}|RVC_t - RVC_t'| = 10^{a \cdot \Delta m + b}, \qquad (3.4)$$

where a and b are the coefficients presented in Table 3.7. In this table we also present the the value of the root mean square (rms) for each fit. By comparing the panels of Fig. 3.7 we can also see that the contamination depends not only on Δm, but also, as expected, on the target-contaminant spectral type combination. This becomes more evident in Fig. 3.8. This
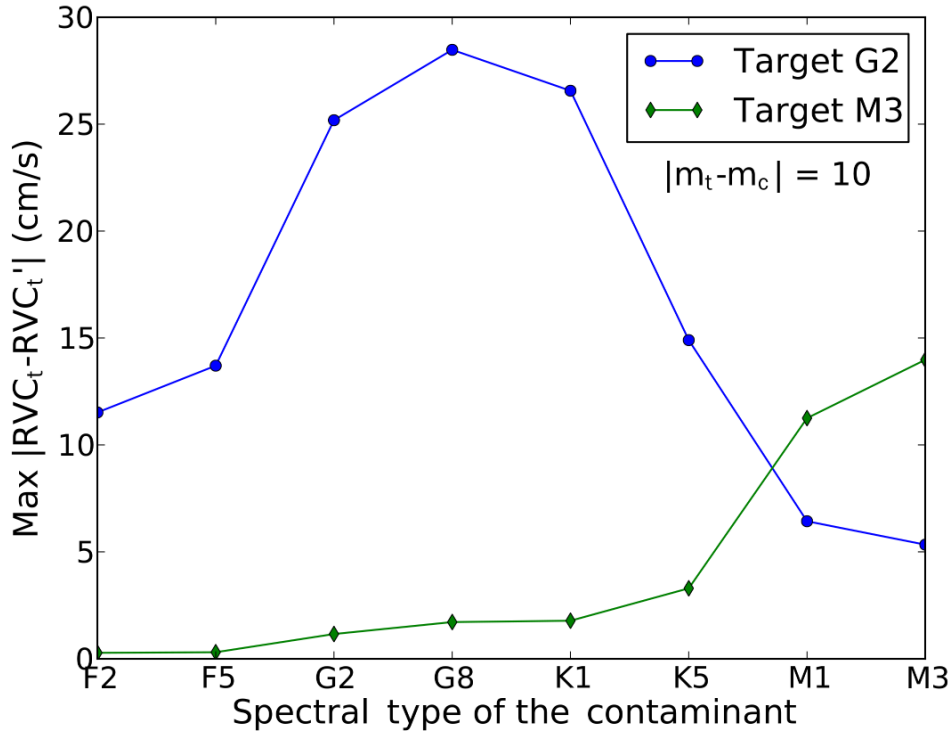
Figure 3.8: Maximum contamination $|RVC_t - RVC_t'|$ as a function of the contaminant spectral type for a G2 (blue dots) and M3 (green diamonds) target star with $\Delta m = 10$.

figure shows the maximum contamination in the RV calculation of target stars of spectral type G2 (the target star of earliest spectral type used in this work) and M3 (the target star of latest spectral type used here), as a function of the spectral type of the contaminant with $\Delta m = 10$. We find two possible reasons for this behavior. First, less contamination occurs with increasingly different spectra. Second, the contamination will depend on the depth of spectral lines. Therefore, when we have similar spectra for target and contaminant star, cooler stars will cause higher contamination, because they have deeper spectral lines.

Table 3.7: Coefficients a an b for each fitting of the relation between Δm and the maximum impact on the RV calculations: $\text{Max}|RVC_t - RVC'_t| = 10^{a \cdot \Delta m + b}$, and rms resulting from each combination of target spctral type (TST) and contaminant spectral type (CST).

TST	CST	a	b	rms [cm/s]
G2	F2	-0.4008	5.0733	815.0813
	F5	-0.4019	5.1601	1644.9045
	G2	-0.4022	5.4288	4491.1375
	G8	-0.4023	5.4829	4956.4768
	K1	-0.4026	5.4556	5136.0605
	K5	-0.4009	5.1859	1500.0546
	M1	-0.4001	4.8096	23.3793
	M3	-0.3996	4.7301	197.1604
G8	F2	-0.4008	4.9379	681.0614
	F5	-0.4019	5.0222	1075.0923
	G2	-0.4027	5.3440	3968.9098
	G8	-0.4021	5.3154	2697.4956
	K1	-0.4027	5.3641	4215.8544
	K5	-0.4007	5.11	1139.4446
	M1	-0.3995	4.7357	3.0972
	M3	-0.3984	4.651	51.5545
K0	F2	-0.3812	4.7320	1566.6309
	F5	-0.4008	4.9521	871.3506
	G2	-0.3933	5.2712	5307.563
	G8	-0.3929	5.2613	4246.1257
	K1	-0.3954	5.3704	7390.8788
	K5	-0.3914	5.1827	3347.1766
	M1	-0.3799	4.7540	566.5518
	M3	-0.3777	4.6783	532.1239
K5	F2	-0.3988	4.9559	200.036
	F5	-0.3999	5.0865	724.4446
	G2	-0.4035	5.4592	7366.4185
	G8	-0.4032	5.5354	8587.4134
	K1	-0.4053	5.5580	14146.5377
	K5	-0.4030	5.3793	4935.42
	M1	-0.4011	4.9458	71.0313
	M3	-0.4009	4.9257	98.6394
M1	F2	-0.4056	3.5177	18.1497
	F5	-0.3932	3.4673	24.6295
	G2	-0.4018	4.1212	10.1997
	G8	-0.4011	4.2786	13.0058
	K1	-0.3990	4.1604	24.4166
	K5	-0.4014	4.5525	19.9346
	M1	-0.3985	5.0993	33.3093
	M3	-0.3994	5.1581	56.2493
M3	F2	-0.4052	3.4770	14.7829
	F5	-0.3924	3.4421	25.7393
	G2	-0.4035	4.0854	30.8372
	G8	-0.4019	4.2469	23.5459
	K1	-0.4024	4.2649	35.7392
	K5	-0.4021	4.5317	32.2298
	M1	-0.3991	5.0440	13.2551
	M3	-0.3999	5.1436	63.9946

3.5.4 Statistical analysis of the contamination

After calculating the impact caused by a contaminant source in the RV calculation, it is important to know how often this kind of contamination occurs. Therefore we calculated the probability of measuring the target RV with a given contamination.

In the previous subsections, Sects. 3.4.2 and 3.5.3, we presented a study for the impact of having a contaminant source within the fiber on the RV calculation, assuming that the fiber was well centered on both target and contaminant stars. Although this is a relevant study, it is not very probable to happen. The most probable scenario for real observations is that of a contaminant star that is not centered in the fiber. In this case we cannot consider that both target and contaminant fluxes will completely enter the fiber. Therefore, to make the statistical analysis we calculated how much of each flux enters the fiber. The fraction of binary and fortuitous alignments and their properties also follow established probability laws. To take these parameters into account in a realistic way, we ran Monte Carlo simulations with 10000 trials, to calculate the distribution function of the impact caused by the presence of a contaminant star on the RV calculation. Once again, we had to consider both kinds of contaminants: binaries and fortuitous alignment. If in our simulations one star was in a binary system and had a background/foreground star at the same time, we only considered the stronger RV effect. In these simulations we did not taken into account the contamination by the sky brightness either, and also just considered that only $\Delta RV \leq 20\,\mathrm{km\,s^{-1}}$ will produce a significant impact. We ran simulations for each case of spectral type target considered in the previous sections, at a distance $d = 1$, 5, 10, 50, and $100\,\mathrm{pc}$ from Earth.

Before presenting our results of the statistical analysis we describe in more detail the considerations to statistically analyze the real binaries and the fortuitous alignments.

Statistical analysis of binaries

For our statistical analysis of contamination in binary systems, we considered the mass ratio distribution, q, mentioned in Sect. 3.2.1. We used Table 3.1 based on the study of Duquennoy & Mayor (1991) for target stars of spectral types G and K, and Table 3.3 based on the study of Janson et al. (2012) for target stars of spectral type M. Because we had M1 and M3 spectra to represent the M stars, we used the M1 spectrum to calculate the contamination caused by M0 - M4 stars, and the M3 spectrum for later types. From the work of Duquennoy & Mayor (1991) and Janson et al. (2012) we also used the the probability density function for the orbital period and for the eccentricities (see Table 3.2) for G dwarfs, and the probability density function for the semi-major axis for M-dwarfs (see Table 3.4). The projected distance, R, and the ΔRV were drawn performing a Monte Carlo simulation of Kepler's laws and its projection,

considering a uniformly random mean anomaly ($M \in [0, 2\pi]$), inclination ($\cos i \in [-1, 1]$), longitude of the node($\Omega \in [0, 2\pi]$), and argument of the periapsis ($\omega \in [0, 2\pi]$).

To compute the luminosity of the stellar companion given the mass of the star, we used the relation 3.5 from Duric (2003):

$$\begin{cases} \frac{L}{L_\odot} \propto \left(\frac{M}{M_\odot}\right)^{4.0} & \text{if } M > 0.43 M_\odot; \\ \frac{L}{L_\odot} \propto 0.23 \left(\frac{M}{M_\odot}\right)^{2.3}, & \text{if } M < 0.43 M_\odot. \end{cases} \tag{3.5}$$

Statistical analysis of fortuitous alignments

For the fortuitous alignment we are only interested in contaminant stars whose flux can enter the fiber. With a seeing of 0.93, which is the mean value for the La Silla observatory, we measured that the fraction of flux that enters the fiber of a star at 2.6 arcsec from the fiber center is of 2×10^{-8}. If target and contaminant star have the same magnitude, this corresponds to an effective Δm of 19 within the fiber, and so its impact on the target RV calculation can be considered null for our purpose. We then created a probability density function representing a contaminant source of a certain spectral type and magnitude within a radius of up to 2.6 arcsec around the target star, using the density tables from Appendix A.

For background/foreground stars within 2.6 arcsec radius we assumed a uniform distribution, and if a contaminant is present, the probability that the star is standing at a distance r from the target is proportional to r^2, and the probability to have fortuitous contaminant star between r and $r + dr$ is given by equation 3.6:

$$P(r, r + dr) = \pi(2r dr + dr^2), \tag{3.6}$$

in which the members are self-explanatory.

To calculate ΔRV we used the probability density function for the systemic RV, which was computed by fitting a Gaussian to the systemic velocity of stars from HARPS. This yielded an average and a dispersion of $(\mu, \sigma) = (7.87, 29.87)$.

Statistical analysis results

The probability to have a given impact on the RV calculation of a target of spectral type from G to M is presented in Fig. 3.9 We can see that the most probable scenario is to have a contamination with an impact of less than $10\,\text{cm}\,\text{s}^{-1}$. But contamination may happen and it is more probable for faraway target stars, either because they are fainter due to the distance , or because, in the case of binary star, it is more probable that the companion star flux enters

37

the fiber. We can examine the target star G8, for instance. In this case, if the target star is $100 \, \mathrm{pc}$ away, there is only a probability of 67% for a contamination below $10 \, \mathrm{cm \, s^{-1}}$, and a 14% probability for a contamination between 10 and $100 \, \mathrm{m \, s^{-1}}$. There is a peak around a contamination of $10 \, \mathrm{m \, s^{-1}}$, which is, very probably, caused by physical binary contamination. This level of contamination needs to be taken into account when choosing targets for planet searches. This becomes even more important when choosing target stars to be observed with the future spectrograph ESPRESSO.

3.6 Discussion

With our work we showed that we should not neglect the possibility that a stellar companion contaminates the RV calculations. This is specially true for faraway target stars, which have a higher probability to have flux coming from two stellar sources within the fiber. Nevertheless, we stress some assumptions we made that may have some impact on our work. Because spectra with high S/N are scarce for late-M stars, in our statistical analysis we used the M1 spectra to represent M0 - M4 bin and the M3 spectra for M5 - M9. We also assumed that the target star will have at most one stellar contaminant source, because we found that the probability to have two contaminant stars is too low. We also did not take into account the effect of the sky brightness either in the case in which a stellar companion is present or in the case in which the sky brightness is the only possible contamination source.

We also stress that the Besançon model is a probabilistic model, and thus it is not free of errors. We consider it reasonable that the distribution of fortuitous alignment is a Poisson distribution of stars. Therefore, the associated error is to $\sqrt{N}$, where N is the number of stars per area element.

The results presented in Fig. 3.7 may lead one to think that contamination may be stronger that it actually is. We should not forget that this figure represents only the particular case in which both target and contaminant stars are well-centered in the fiber and that all the flux coming from the two stars enters the fiber. On top of that, it only shows the maximum impact of this particular and not very probable configuration, as a function of Δm, which occurs when $|RV(contaminant)| \sim 0.6 \times FWHM(target)$. With our statistical analysis we are able to conclude that it is important to take into account the possibility of contamination by stellar contaminant sources within the fiber, especially when the RV precision enters the domain of the $\mathrm{cm \, s^{-1}}$. Although the probability to have a contamination lower than $10 \, \mathrm{cm \, s^{-1}}$ is above 50% for every target star considered in this work, we should pay special attention to faraway target stars, for which the impact of contamination can be higher than $10 \, \mathrm{cm \, s^{-1}}$ for $30 - 40\%$ of the cases.

3.6.1 Impact on typical cases

As a consequence of the results presented in Fig. 3.7, we present in Table 3.8 a study on the limit Δm for which the maximum impact on the RV calculation is higher than $10\,\mathrm{cm\,s^{-1}}$, 1, 10, and $100\,\mathrm{m\,s^{-1}}$. From this table we can see that for a G star with a contaminant M star,

Table 3.8: Limit Δm for which the maximum impact (I_{max}) on the target RV is higher than 0.1, 1, 10, and $100\,\mathrm{m\,s^{-1}}$, for each combination of target sepctral type (TST) and contaminant spectral type (CST).

TST	I_{max}[m/s]	CST							
		F2	F5	G2	G8	K0	K5	M1	M3
G2	0.1	10	10	11	11	11	10	9.5	9.5
	1	8	8	9	9	9	8	7	7
	10	5.5	5.5	6	6	6	5.5	4.5	4.5
	100	3	3	4	4	4	3	2	2
G8	0.1	10	10	11	11	11	10.5	9.5	9.5
	1	7.5	7.5	8.5	8.5	8.5	8	7	7
	10	5	5	6	6	6	5.5	4.5	4.5
	100	2.5	2.5	3.5	3.5	3.5	3	2	2
K0	0.1	9.5	9.5	11	11	11	10.5	9.5	9.5
	1	7.5	7.5	8.5	8.5	8.5	8	7.5	7.5
	10	4.5	5	6	6	6	5.5	4.5	4.5
	100	2.5	2	3.5	3.5	3.5	3	2	2
K5	0.1	10	10.5	11	11.5	11.5	11	10	10
	1	7.5	8	8.5	9	9	8.5	7.5	7.5
	10	5	5.5	6	6.5	6.5	6	5	5
	100	2.5	2.5	3.5	4	4	3.5	2.5	2.5
M1	0.1	6.5	6.5	7.5	8	8	8.5	10.5	10.5
	1	4	4	5.5	6	5.5	6.5	8	8
	10	1.5	1.5	3	3	3	4	5.5	5.5
	100	—	—	0.5	0.5	0.5	1.5	2.5	2.5
M3	0.1	6.5	6.5	7.5	8	8	9	10.5	10.5
	1	3.5	3.5	5	5.5	5.5	6.5	7.5	7.5
	10	1	1	2.5	3	3	3.5	5	5
	100	—	—	0	0.5	0.5	1.5	2.5	2.5

an impact higher than $100\,\mathrm{m\,s^{-1}}$ only occurs if $\Delta m < 2$. However, in Table 3.5 we have seen that the probability to have a contaminant M star of $m_v < 17$ is very low. Thus, if we only care about target stars brighter than $m_v = 15$, an impact of larger than $100\,\mathrm{m\,s^{-1}}$ is very unlikely. We can see that when observing an M star, an F star can never cause an impact higher than $100\,\mathrm{m\,s^{-1}}$, and a impact of tens $\mathrm{m\,s^{-1}}$ is only possible if target and contaminant source have almost the same magnitude ($\Delta m \lesssim 1.5$). On the other hand, even for actual precisions, we may reach a potentially detectable contamination due to a $\Delta m = 9$. In any cases the induced effect is not detectable because it is a constant effect. Nevertheless, there are conditions (variable seeing, centering and/or pointing problems, etc.) in which the induced effect will not be constant. Even so, a very particular configuration is necessary (and is highly unlikely) for the effect to create a periodic signal. A contamination stronger than $1\,\mathrm{m\,s^{-1}}$ on

the RV calculation of a K0 target star is possible if $\Delta m < 9$. If the K0 star is at $10\,pc$, it will have a $m_v \sim 6$, which means that contaminants stars with with a visual magnitude of $6 \leq m_v \leq 15$ can cause such a contamination. The probability to have one contaminant star with $6 \leq m_v \leq 15$ within the 0.5" radius fiber is of 0.02% only.

We note that these tabled effects correspond to the maximum contamination, i.e., to the difference between contamination and no contamination. Nevertheless, to extensively analyze a variable contamination impact we would need to perform many hypotheses with uncertain parameters, such as seeing or flux counts.

Sky brightness

In our analysis of the sky brightness impact we assumed the flux provenience is the moon;, as the moonlight is nothing more that reflected light from the Sun, its spectrum will be that of a star with spectral type G2. The new-moon sky brightness, should then be considered as a lower limit for the contamination coming from the sky brightness with a G2 spectrum. However, we should not forget that sky brightness has other sources and may depend on the sky zone. Sky spectra from the Galactic disk are surely different from the Galactic halo. Moreover, there is also the possibility to have a galaxy as a contaminant, which is not considered in the scope of this work. Nevertheless, we consider it is a good approximation, or at least a good starting point, to treat the sky brightness as a G2 star.

If observations are carried out on a night with moon, and if cirrus are present, the contamination by the moon will be enhanced.

Tripathi et al. (2010), reported two outlier RV data points caused by cirrus during their observations of *WASP-3*, an F7 star of $mv = 10.7$, on a full-moon night. Their RV measurements present a redshift of $140\,\mathrm{m\,s^{-1}}$ and of $49\,\mathrm{m\,s^{-1}}$ with respect to their best-fit models. Again, if we assume that cirrus will reflect some of the moonlight, we have a G2 contaminant. The maximum value considered for all practical effects for visual magnitude of this contaminant will be that the target star (if it were higher than the target magnitude, the target star would be no longer visible). Thus, for a G2 target star with $m_v = 10.7$ and a contaminant with the same spectral type and magnitude, the maximum contamination will be of $2.7\,\mathrm{km\,s^{-1}}$.This corresponds to 0.15% of the moonlight flux, considering that 100% of the moonlight flux corresponds to a star of magnitude 3.65. If 0.01% of the moonlight reaches the fiber, corresponding to a contaminant source of spectral type G2 with $m_v = 13.7$, the contamination would be of $140\,\mathrm{m\,s^{-1}}$. For a contamination of $49\,\mathrm{m\,s^{-1}}$, 0.003% of the moonlight flux would be enough, corresponding to a G2 contaminant star with a visual magnitude of $m_v = 14.8$. Because the Tripathi et al. (2010) data were taken with the High Resolution Échelle Spectrometer (HIRES) on the Keck I telescope, and we used HARPS spectra in our

simulation, and also because we did not calculate the impact for a target of spectral type F, these contamination values are presented here just as a reference, since we cannot directly compare them. Nevertheless, our results suggest that their hypothesis of cirrus contamination is a valid one.

The sky brightness contamination is not easily removed. Although its signal may be strong enough to contaminate the RV calculations, it will be to weak to be adequately characterized, fitted, and removed, even for a long-slit spectrograph.

Kepler stars

Our work can also be a valuable asset for the follow-up of programs such as *Kepler*. Stars observed by *Kepler* have between of $11 \lesssim m_v \lesssim 18$ (see Batalha et al. 2012), and consequently, measuring the RV of these stars becomes challenging. Beyond the problem of these being faint stars, there is also the problem of the false-positive planet transit. As an example, we consider the case of *Kepler-14b* (Buchhave et al. 2011), a planet orbiting an F star with a companion star nearly the same magnitude and only $0.3''$ of sky-projected angular separation. Buchhave and collaborators were not able to detect a second peak on the CCF and concluded that the two stars probably have nearly the same RV. They computed an impact of $280\,\mathrm{m\,s^{-1}}$ on the RV caused by the companion star. A direct comparison with their work is not possible, because their observations were carried out with the Fiber-fed Échelle Spectrograph (FIES) at the $2.5\,\mathrm{m}$ NOT at La Palma, and with the HIRES mounted at the Keck I on Mauna Kea, Hawaii. Moreover, our simulation only contemplates target stars of spectral type GKM, and this is an F star. Still, performing a rough comparison, we see that our simulations indicate an impact of $\sim 276\,\mathrm{m\,s^{-1}}$ for G2 target star with a contaminant of the same spectral type, $\Delta m = 1$, and $\Delta RV = 1$.

3.7 Conclusions

This study on the impact of stellar companions within the fiber in RV calculations allows us to conclude that we should not neglect the possibility of contaminant flux from stellar companion sources, particularly if we are observing faraway stars. On average, if we are observing a G or a K star, the contamination may be higher than $10\,\mathrm{cm\,s^{-1}}$ if the difference between target and contaminant visual magnitude is $\Delta m < 10$, and higher than $1\,\mathrm{m\,s^{-1}}$ if $\Delta m < 8$. If the target is a star of spectral type M, a $\Delta m < 8$ is enough to obtain the same contamination of $10\,\mathrm{cm\,s^{-1}}$, and a the contamination may be higher than $1\,\mathrm{m\,s^{-1}}$ if the magnitude difference between target and contaminant star is $\Delta m < 6$. We also showed that sky brightness should not be discarded, particularly for the data obtained on full-moon nights, if one observes faint

target stars ($m_v > 10$).

These results will allow us to more wisely choose target stars to be observed with instruments such as ESPRESSO and CODEX. They provide provide reference values for different cases of contamination possible in fiber-fed high-resolution spectrographs. We also stress that there are diagnosis methods that should be capable of detecting most of the blends that mimic an exoplanet signal. We can detect a blend through bisector analysis of the CCF or from correlations using different templates (Santos et al. 2002).
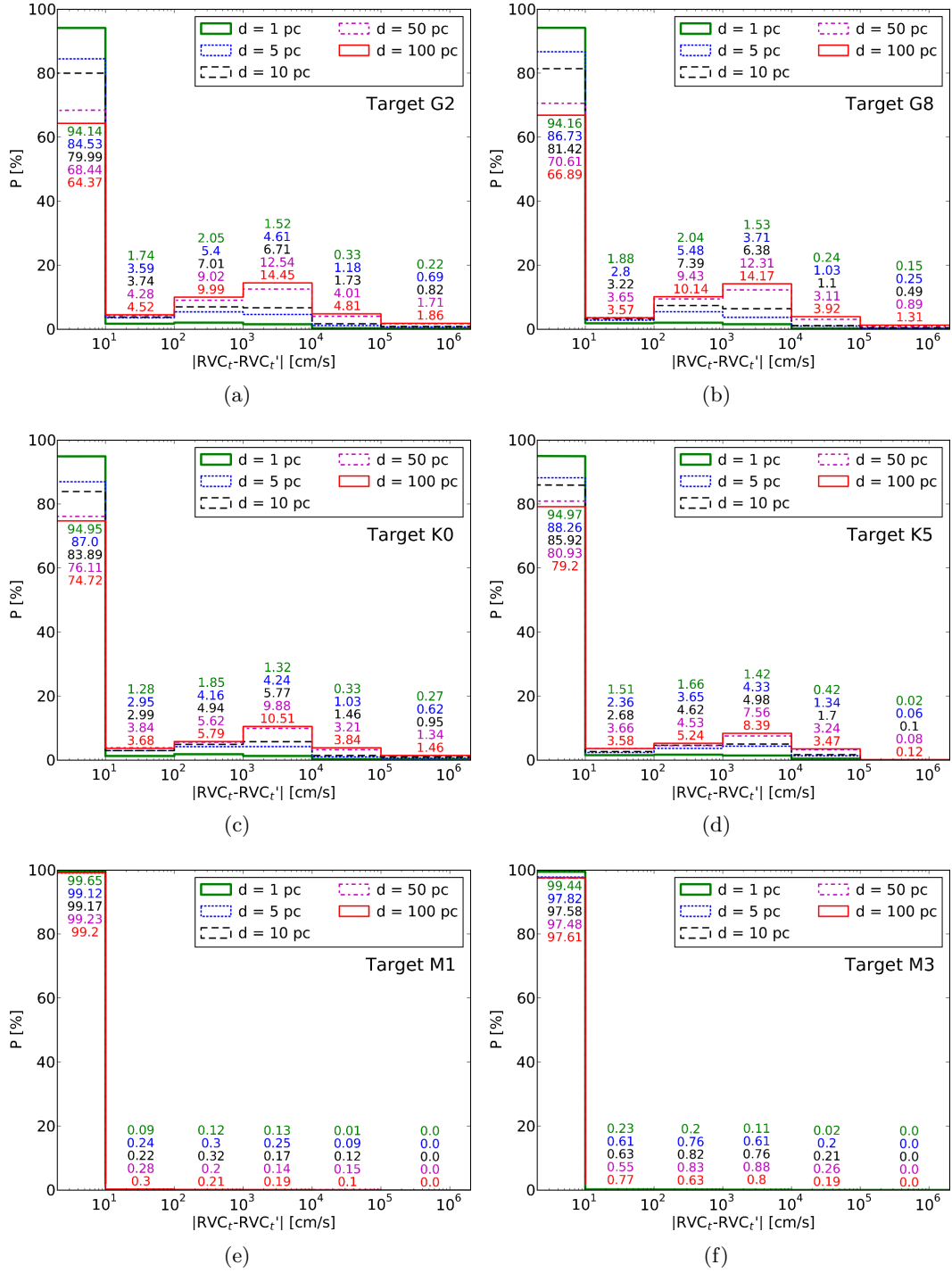
Figure 3.9: Close-up of the distribution of the expected contamination , $|RVC_t - RVC_t'|$, on the radial velocity, $|RVC_t|$, of a target star of spectral type **a)** G2, **b)** G8, **c)** K0, **d)** K5, **e)** M1, and **f)** M3, and at distance d, caused by a background or a companion star. The green thick solid line shows the distribution if the target star stands at a distance of d = 1 pc, the blue dotted line for d = 5 pc, black dashed line for d = 10 pc, magenta dash-dotted line for d = 50 pc, and red solid line for 100 pc. Numbers in each bin correspond to the impact probability for each target distance: the number in the top corresponds to 1 pc and the number in the bottom to 100 pc.

43

Chapter 4

Micro-telluric lines and stellar radial velocities

4.1   Introduction

The current ace of in extra solar planets discovery is HARPS, the fiber-fed, cross dispersed échelle spectrograph installed at the 3.6-m telescope at the La Silla observatory. It achieves routinely a precision of better than $1\,\mathrm{m\,s}^{-1}$ (Mayor et al. 2003), and down to $50 - 60\,\mathrm{cm\,s}^{-1}$ (Dumusque et al. 2012).

This level of precision is still not sufficient to find an Earth-like planet on a 1-year orbit around a Solar-like star. As we have seen in Sect. 1.2.1, the impact of Earth in the Solar RV is only of $\sim 9\,\mathrm{cm\,s}{-}1$. As we also have seen in Sects. 2.4 and 3.1, a new generation of high precision spectrographs is currently being planned with the objective of detecting Earth-mass extra solar planets; among these stands out ESPRESSO, aiming at a precision of ten $\mathrm{cm\,s}^{-1}$ (Pepe et al. 2010) and having as one of main science goals the detection of an Earth-mass planet in the habitable zone of a Sun-like star. An increase of precision (and accuracy) implies a more detailed characterization of systematics and in particular the need to be more careful with contamination sources. As was it was presented in previous chapter (Cap. 3), the presence of an unknown secondary star of a binary system, of a back/foreground star, or even just the moonlight may have an impact in the RV calculations of a target star.

One other possible source of contamination mentioned in Sect. 2.4 is the Earth's atmosphere, which spectrum is imprinted on top of the target star spectrum.

The pursuit for the best method of correcting stellar spectra from atmospheric lines is not a recent matter. One possible way of doing it is to use standard stars, for which spectral features are well known, to determine the atmospheric spectrum (as e.g., see Vacca et al.

2003). Using simulations, Bailey et al. (2007) showed that, for infrared observations, using an Earth atmospheric transmission spectrum modeled with SMART (Spectral Mapping Atmospheric Radiative Transfer model), leads to a better correction of the telluric lines than using the "division by a standard star" technique. Following Bailey et al. (2007) work, Seifahrt et al. (2010) developed a method to calibrate the wavelength of CRIRES (High Resolution Infrared Spectrograph for ESOs VLT) , and to correct its observations from telluric lines, by modeling the Earth atmospheric transmission spectra with the LBLRTM (Line-By-Line Radiative Transfer Model). Also, Cotton et al. (2013) used the division by modeled telluric spectra for the removal of telluric features from Jupiter and Titan's infrared spectra, just to cite a few examples from an extensive list.

The present chapter follows the method that resorts to theoretical atmospheric transmission spectra to remove telluric features from stellar spectra. To achieve that, we used the atmospheric models LBLRTM and TAPAS, which are described in the next section, Sect. 4.2. In Sect. 4.3 we present a study on the impact of the micro-telluric lines by adding an atmospheric spectrum to a synthetic sun-like stellar spectra, and in Sect. 4.4 this effect is corrected by removing the atmospheric spectra from HARPS spectra. We finish this chapter with a discussion about our work and presenting our conclusions in Sect. 4.5.

4.2 Atmospheric spectra with LBLRTM and TAPAS

In this section we describe the two atmospheric models used in this work: the Line-By-Line Radiative Transfer Model (LBLRTM) and the Transmissions Atmosphériques Personnalisées Pour l'AStronomie (TAPAS), which are not independent.

4.2.1 LBLRTM

The LBLRTM is an accurate model derived from the Fast Atmospheric Signature Code (FASTCODE) (Clough et al. 1981, 1992) that uses the HITRAN database (HIgh-resolution TRANsmission molecular absorption database) as the basis for the line parameters. This is a very versatile model that besides the predefined models (tropical, mid-latitude summer, mid-latitude winter, subarctic summer, subarctic winter, and U.S. standard 1976), it also accepts a user supplied atmospheric profile. This model has been extensively validated from ultra-violet to the sub-millimeter (e.g. Turner et al. 2004). The key attributes of LBLRTM are described in Clough et al. (2005) and Shephard et al. (2009), and are summarized here. Voigt line shape is used at all atmospheric levels with an algorithm based on a linear combination of approximating functions. The LBLRTM incorporates the MT_CKD (Mlawer, Tobin, Clough, Kneizys, Davies) water vapor model, which includes self- and foreign-broadened water vapor

as well as continua for carbon dioxide, and the collision induced bands of oxygen at $6.25\,\mu$m and nitrogen at $4.26\,\mu$m. Parameters from HITRAN line database are used including the pressure shift coefficient, and halfwidth temperature dependence, and the coefficient for the self-broadening of water vapor. Total Internal Partition Function (TIPS) program is used for temperature dependence of the line intensities (Fischer et al. 2003). CO_2 line coupling is treated as first order with coefficients for CO_2 generated from the code of Niro et al. (2005) and Lamouroux et al. (2010), and CH_4 line parameters include line coupling for the $3.33\,\mu$m and $7.7\,\mu$m bands of the main isotopologue. Temperature dependent cross section data, such as those available with HITRAN database, may be used to treat the absorption due to heavy molecules (e.g. halocarbons). Variation of the Planck function within a vertically inhomogeneous layer is treated using an implemented algorithm as discussed in Clough et al. (1992). LBLRTM is capable of computing analytic Jacobians, and includes the option of modeling absorption/emission due to clouds.

In this work, for the LBLRTM we used atmospheric data from the Air Resources Laboratory (ARL) - Real-time Environmental Applications and Display sYstem (READY) Archived Meteorology [1]. Because ARL-READY only provides data up to $26\,$km of altitude, for higher atmospheric layers we used the MIPAS Model Atmospheres (2001) for the mid-latitude, night-time [2]. If one wants one wants to have the absolute control on the input parameters for the atmospheric spectra, LBLRTM is undoubtedly the model to use. The drawback in using LBLRTM is the lack of user friendliness in the input method and the somewhat cryptic/highly technical user instructions. Therefore, in this work we tested a more user friendly model: TAPAS.

4.2.2 TAPAS

TAPAS is a free on-line service that simulates atmospheric transmission [3]. TAPAS makes use of the ETHER (Atmospheric Chemistry Data Center) facility to interpolate within the ECMWF (European Center for Medium-Range Weather Forecasts) pressure, temperature and constituent profile at the location of the observing site and within 6 hours from the date of the observations, and computes the atmospheric transmittance from the top of the atmosphere down to the observatory, based on the HITRAN and the LBLRTM code. TAPAS is much more user friendly than LBLRTM, although users have less control, having a much smaller number of input parameters. For more details the reader is referred to Bertaux, J. L. et al. (2014).

Figure 4.1 shows the spectra obtained with both models - LBLRTM and TAPAS - using as

---

[1]http://ready.arl.noaa.gov/READYamet.php
[2]http://www.atm.ox.ac.uk/RFM/atm/
[3]http://ether.ipsl.jussieu.fr/tapas/
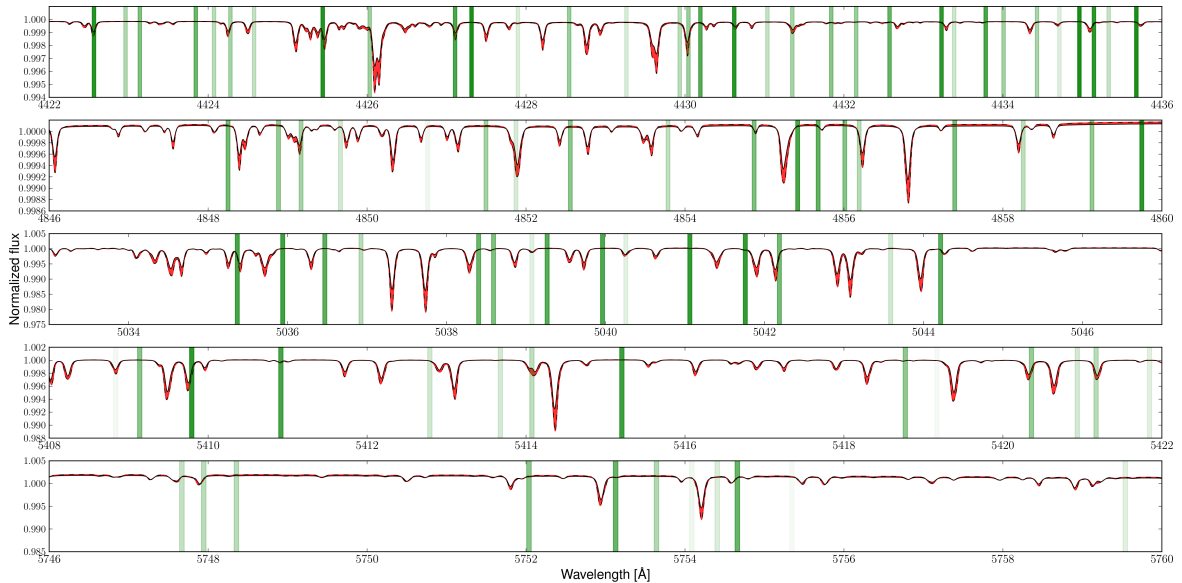
Figure 4.1: Normalized synthetic atmospheric spectra obtained with TAPAS (top black line) and LBLRTM (bottom black dashed line). The vertical thick green lines represent the G2 stellar mask for a velocity V = 0, and its intensity the weight in the CCF.

input identical physical conditions. The top black line represents the spectra obtained with TAPAS and the bottom dashed black line the LBLRTM model. The two spectra overlap significantly but show a few differences (red shadow area between lines). In Fig. 4.1 the vertical green tick lines represent the position of stellar lines in the G2 mask used by HARPS pipeline, where the intensity corresponds to the weight of each line in the CCF. One can see that some telluric lines fall within or close to the mask lines, and so they are taken into account in the RV calculation.

To compare the capabilities of the two models at reproducing the atmospheric transmission, a spectrum of a spectral type O5 star was corrected from Earth's atmospheric absorption using each of the models. A *HD 46223* HARPS spectrum, taken during the program ID 185.D-0056(L), with a S/N of 220 at the center of the spectral order number 50 (which corresponds to a wavelength of 4372.8 Å). The choice of an O5 star was motivated by the low number of spectral lines. Figure 4.2 shows the normalized stellar spectra before correction (blue), and after correction with LBLRTM (green) and with TAPAS (red). We also computed the standard deviation $\sigma_{O5/LBLRTM}$ and $\sigma_{O5/TAPAS}$ in a part of the spectra without stellar lines, but with telluric spectral lines ($6474.6\mathring{A} < \lambda < 6518.3\mathring{A}$), as a measurement of scattering of the corrected spectra. We obtained σ values of 0.0078 and of 0.0081, respectively. The differences between the models are small and both of them correct well the atmosphere, which is confirmed by the same order of magnitude of the standard deviations, with a difference between them of only 3.7%. In this work we have chosen to use the TAPAS method because it is easier to use.
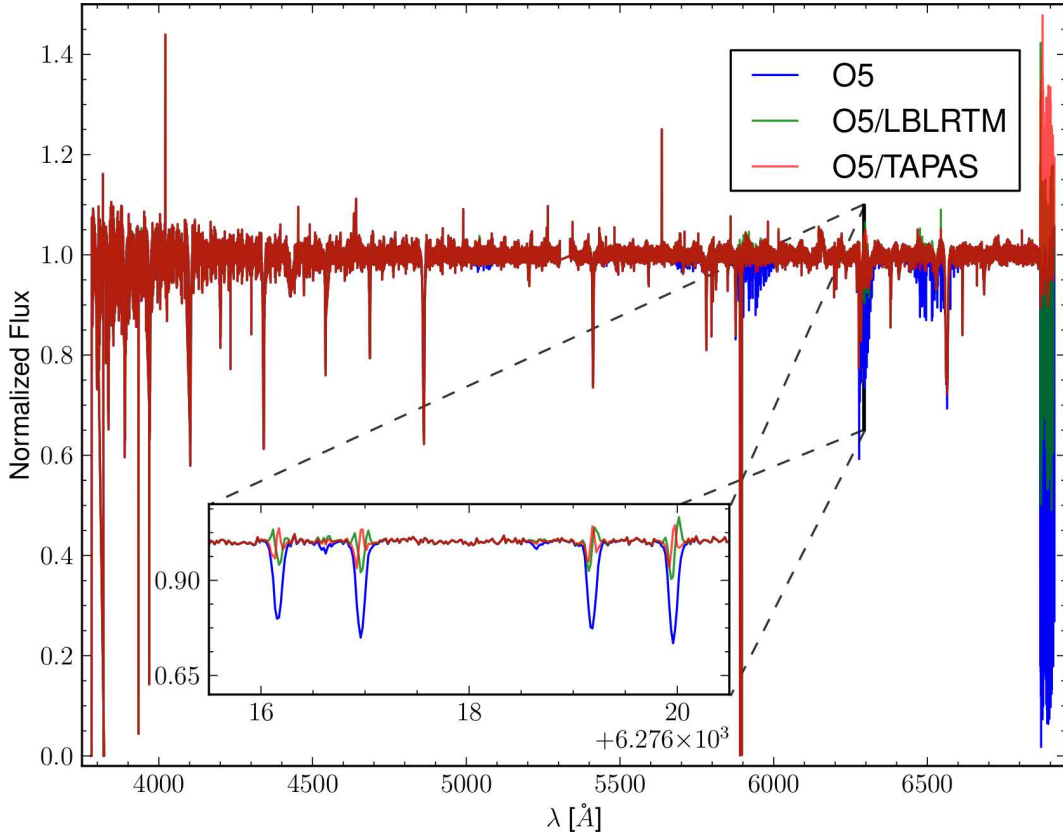
Figure 4.2: Blue: Normalized spectrum of the spectral type O5 *HD 46223* star; Green : Normalized spectrum of the spectral type O5 star *HD 46223* divided by the atmospheric spectrum obtained with LBLRTM; Red: Normalized spectrum of the spectral type O5 star *HD 46223* divided by the atmospheric spectrum obtained with TAPAS.

4.3 Synthetic stellar spectra test

Before correcting HARPS spectra from telluric lines absorption, we first calculate the impact of the micro-telluric lines using synthetic stellar spectra of a solar-like star, i.e., the difference between the RV obtained when using a stellar spectra with and without the atmosphere. The synthetic spectrum was build by extracting the spectral lines using VALD - Viena Atomic Line Database (Piskunov et al. 1995; Ryabchikova et al. 1997; Kupka et al. 1999, 2000), and then computing the spectrum using the running option *synth* off MOOG (Sneden 1973). This spectrum was multiplied by TAPAS atmospheric spectra for one night with H_2O vertical column of $14.52\,\mathrm{g\,m^{-3}}$. The water vapor content is relevant since the micro-telluric lines are partially H_2O and thus the lines' depth varies with the water vapor content. Moreover, the lines' depth in atmospheric spectra increases as the airmass increases. Therefore, we obtained TAPAS spectra for different values of the zenith angle (and so different values of airmass), using as input the same time of observation. In doing so we only consider zenithal angles up to $60\,^{\circ}$, i.e., for airmass values below 2.

49

For each simulated atmospheric spectra we then changed the RV of the star by shifting the stellar spectra from $RV = -100\,\mathrm{km\,s^{-1}}$ to $RV = 100\,\mathrm{km\,s^{-1}}$ in steps of $1\,\mathrm{km\,s^{-1}}$. The RV of each spectrum , with and without atmosphere, was calculated by cross-correlating it with a template (Baranne et al. 1996; Pepe et al. 2002). We then calculated the impact of the atmosphere as the difference between the RV of the original spectra (RV_o) and the RV of the modified spectra (RV_m)

$$\text{Impact} = RV_o - RV_m. \tag{4.1}$$

In the case of the synthetic spectra, the original spectra will be the one without atmosphere and the modified will be the one with atmosphere. The results are presented in Fig. 4.3, where one can see that the impact of the atmosphere will depend on the airmass of the observation, and on the RV of the star, as expected. The impact of the different models scales with airmass.
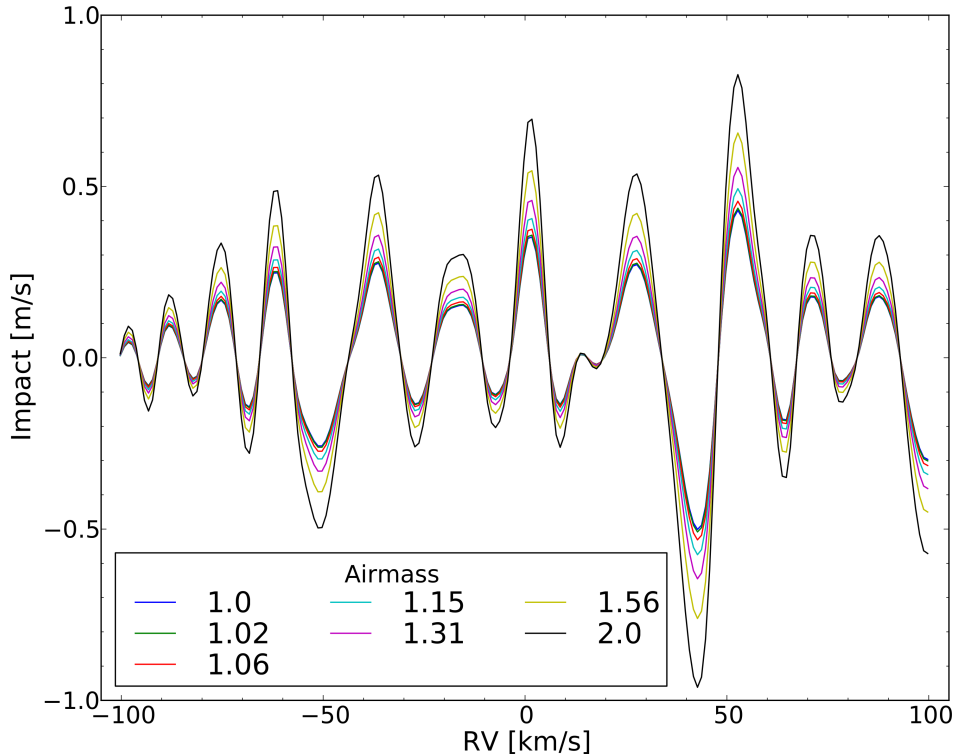
Figure 4.3: Impact of the atmosphere in the RV calculation for airmass values between 1 and 2. The inner line represents the airmass = 1 and the outer the airmass = 2.

When one compares the maximum impact for the different values of airmass (Fig. 4.4) one can see that the micro-telluric lines can introduce an RV variation large enough to mimic or hide a planet. This is specially relevant when searching for small exoplanets using observations taken in different nights with a large relative difference in the H_2O vertical column, or when the same star is observed several times along one night with large H_2O vertical column variation.
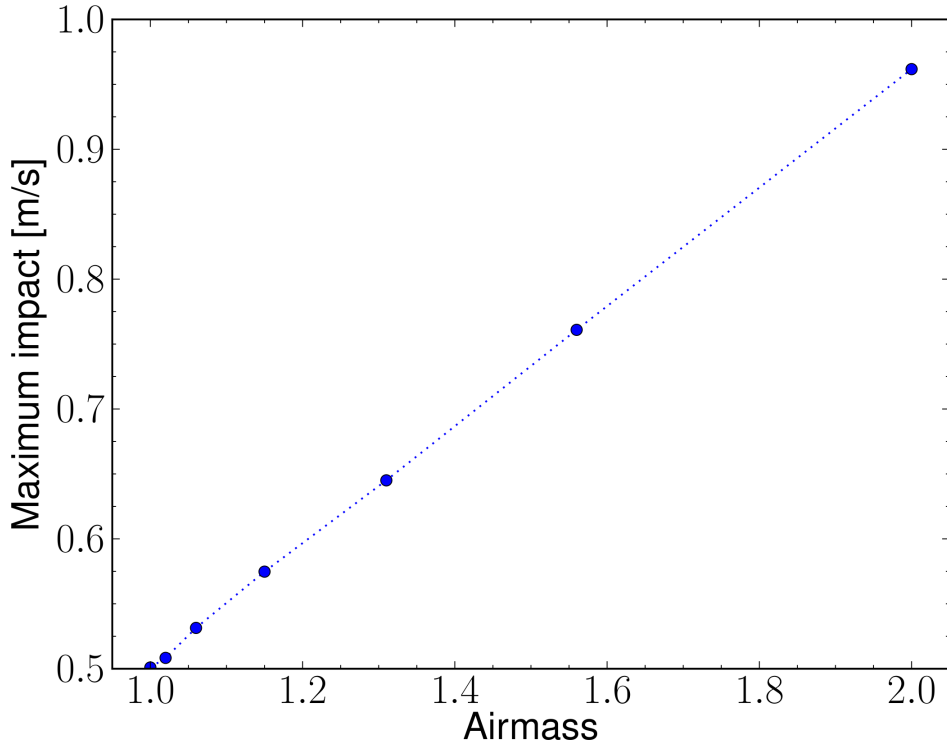
Figure 4.4: Maximum impact in the RV calculation for the different values of airmass.

4.4 Correcting HARPS spectra from micro-telluric lines

4.4.1 Data

In this section we investigate the impact of the atmospheric micro-telluric lines on real spectra obtained with HARPS. To do so, we used *18 Sco* time series of data obtained on the night of $2012-05-19$ under the program ID 183.D-0729(B), allowing therefore the study of the impact of the airmass in the RVs along the night. The S/N at the center of the spectral order number 50 (SN50) of the *18 Sco* observations varies between 124 and 212, and the H_2O vertical column predicted by TAPAS varies between 3.83 and $4.51\,g\,m^{-3}$.

To complement the analysis of the *18 Sco* data, we used spectra from three other stars, ranging from G to M - *Tau Ceti* (G8), *HD 85512* (K5),and *Gl 436* (M1). As in our work presented in the previous chapter (Cap. 3) on the impact of stellar companions within the fiber on precise radial velocities (see also Cunha et al. 2013), where these three stars where also used, we choose these stars because they were the ones for which we could find the highest S/N HARPS spectra for their spectra type. We used SN50 ranging from 30 for the M star to 439 for the G star. The values of SN50 of the used spectra can be found in the Appendix B.1, along with the airmass and the Program ID for each observation.

51

4.4.2 The method

To determine the impact of the atmosphere in the RV calculation using HARPS spectra we divided the HARPS stellar spectra by the normalized TAPAS synthetic atmospheric spectra. The TAPAS spectra used in the correction from the atmosphere of each stellar spectra is obtained using as input parameters: the Observatory (ESO La Silla Chile), the exact date and hour of the observation, the spectral range in wavenumber units ($14450 - 26550\,\mathrm{cm^{-1}}$ – corresponding to a wavelength of $377 - 692\,\mathrm{nm}$) , the instrumental function as Gaussian, ARLETTY atmospheric model (ARLETTY is a ETHER atmospheric profile computed by using the nearest in time of the ECMWF meteorologic field observation), a resolution power of 115000, which is the HARPS resolution, a sampling ratio, i.e., the number of points on which the convolved transmission will be sampled for each interval of FWHM, of 10, and the Zenithal angle of the star. All the remaining preferences of the TAPAS request form were the default ones. To convert the wavenumber to the air wavelength (AIR) used in HARPS spectra we first converted into vacuum wavelength (VAC)

$$WVNR\left[\mathrm{cms^{-1}}\right] = \frac{10^8}{VAC\left[\mathring{A}\right]}, \tag{4.2}$$

and then we used the IAU standard conversion from AIR to VAC as given by Morton (1991)

$$AIR\left[\mathring{A}\right] = \frac{VAC\left[\mathring{A}\right]}{(1.0 + 2.735182 \times 10^{-4} + \frac{131.4182}{VAC\left[\mathring{A}\right]^2} + \frac{2.76249\times10^8}{VAC\left[\mathring{A}\right]^4}}. \tag{4.3}$$

Because the atmospheric spectra wavelength grid is different from that of HARPS, we have interpolated the atmospheric wavelength grid to the HARPS grid. On top of that, we shifted the atmospheric spectra of $\pm1500\,\mathrm{m\,s^{-1}}$, in steps of $1\,\mathrm{m\,s^{-1}}$, and we divided the normalized stellar spectra by each shifted atmospheric spectra and we calculated which shifted spectra minimizes the difference between the stellar spectrum before and after atmospheric correction by minimizing the χ^2. This will be the atmospheric spectrum that best corrects for the atmosphere, as more telluric lines of the atmospheric spectrum will coincide with the telluric lines present in the stellar spectrum. The $\pm1500\,\mathrm{m\,s^{-1}}$ value was chosen to make sure that the shift between the telluric lines of the atmospheric spectrum and the telluric lines in the stellar one, either because of the interpolation itself, or because of the RV variations of the telluric lines (Figueira et al. 2010b, 2012), is within that range. Then we ran the HARPS pipeline to determine the RV of the stars, both when considering the atmosphere and after removing it. Recalling Eq. 4.1, in this case the impact is calculated considering RV_o as the RV calculated using the original HARPS spectra with the atmosphere, and RV_m as the RV of the HARPS spectra after the removal of the atmosphere.

4.4.3 Results

Following the work presented in Sect. 4.3, we wanted to investigate the impact of micro-telluric lines and its dependence on the airmass, now using HARPS spectra. We used *18 Sco* observations taken along the same night and with different airmass values. If one considers
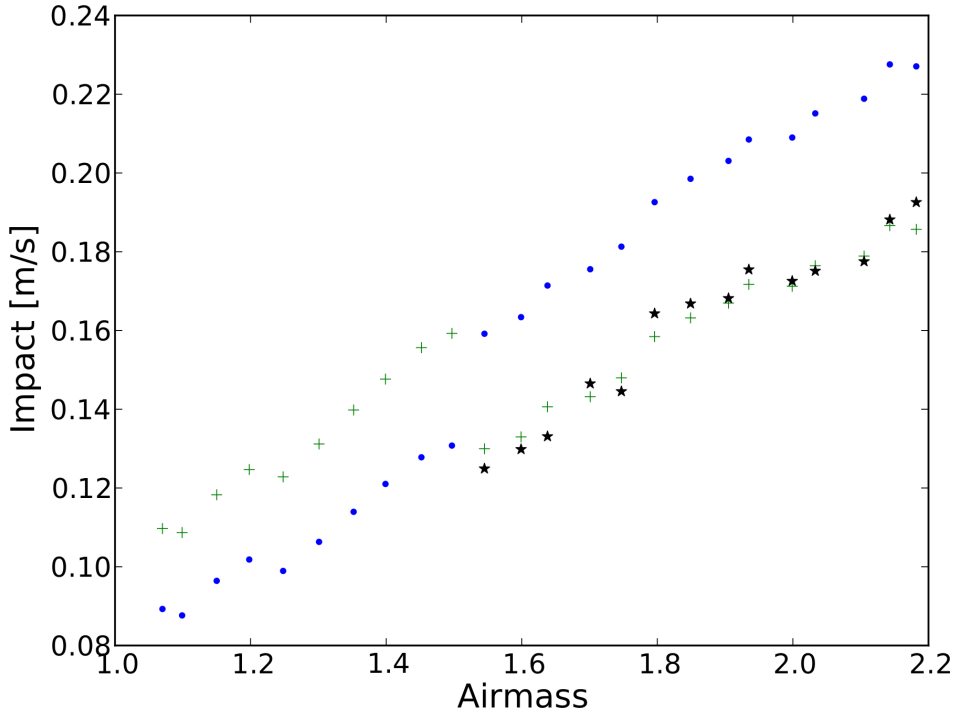
Figure 4.5: Impact of the atmosphere in the RVs for 18 Sco for different values of airmass. All the spectra were taken during the night of 2012-05-19. The blue dots represent the impact calculated using the default TAPAS spectra, the green + crosses in the left part of the plot represent the impact using the TAPAS spectra for the time corresponding to spectra with airmass 1.55, and green + crosses in the right part the impact using the TAPAS spectra for the hour corresponding to spectra with airmass 1.5. The black stars represent the impact using adjusted H_2O transmission spectra.

the blue dots in Fig. 4.5 one can see the impact of Earth's atmosphere in the *18 Sco* RV dependence on the airmass. One can easily see that the impact seems to be linearly proportional to the airmass, except for the airmasses around 1.5, where one can observe a jump in the impact value. This jump is because the data used in the TAPAS atmospheric model is obtained only every 6 hours. Thus, although one of the TAPAS input parameters is the exact hour of the observations, the atmospheric output will be based in an approximated hour. For one full night of observations, one will have at most three different modeled atmospheric spectra. To test if the jump in the impact around airmass = 1.5 was due to a change in the atmospheric data, we repeated our calculations, now using TAPAS spectra with a wrong time of observation: we used the TAPAS spectra with the time stamp of the stellar spectrum with airmass = 1.55 for the correction of stellar spectra with airmass ≤ 1.5 (green + crosses in the left part - before the "jump" - of Fig. 4.5), and TAPAS spectra with the time stamp

corresponding to the spectrum with airmass of 1.5 for the correction of the stellar spectra with airmass ≥ 1.5 (green + crosses in the right part - after the "jump" - of Fig. 4.5). By doing so we end up with two nearly parallel lines for the impact. Each line corresponds to a correction with a different modeled atmospheric spectrum. This result corroborates the hypothesis that the original jump in the impact is due to the use of two different atmospheric data sets. Moreover, we visually checked if the atmospheric lines were being well corrected, and we found that for airmasses greater than 1.5, telluric lines were being over corrected. Thus, for each of these spectra, we adjusted the H_2O transmission by using the power law $T^X(H_2O)$, T being the transmission and the X value the adjusting factor (Bertaux, J. L. et al. 2014). To choose the X value that better corrected the H_2O transmission, we chose a small part of the spectrum with no stellar lines ($\lambda = 6483.25 - 6490.25 \mathring{A}$), and we minimized the standard deviation for this corrected part of the spectrum. The black stars in Fig. 4.5 shows the calculated impact in the radial velocities, when the adjusted transmission for telluric correction is used. We find a difference between the impact calculated with and without adjusted transmission that can go up to $4\,\mathrm{cm\,s^{-1}}$, which is of the order of magnitude of the error of the impact calculation (see Sect. 4.5).

Besides the study of the effect of the micro-telluric lines on the RV calculation throughout a night, we also investigated if the impact of the atmosphere would vary along the year for stars of spectral type G8, K5 and M1. For the CCF of each spectrum we used the corresponding DRS (HARPS pipeline) stellar mask. i.e., for the G8, K5, and M1 target stars we used the G2, K5, and M2 masks, respectively. The result is shown in Fig. 4.6, where we can see the variation of the impact of the atmosphere in the RVs calculations with the Barycentric Earth Radial Velocity (BERV) for stars of spectral type G (small blue dots), ($\times$ green crosses), and M (large red dots). As one saw in Fig. 4.3, telluric lines have a different impact depending on the on the RV of the star. Therefore, as the RV of a star changes along the year w.r.t. the Earth, the impact of the atmosphere also varies as the Earth goes around the Sun, and as the BERV varies. The maximum absolute values of the impact for these G, K, and M stars is of 31.4, 22.6, and 149.6 $\mathrm{cm\,s^{-1}}$, respectively. We also calculated the standard deviation (σ) for the relations between the impact and the stellar RV of the G2 synthetic spectra (Fig. 4.3), and between the impact and the BERV (Fig. 4.6) for the different spectral types. For the G2 star we present σ for an airmass of 1.0, 1.15, and 2.0. For the stellar spectra obtained with HARPS we calculated σ considering all the impacts of each star, and also neglecting impacts obtained with airmasses above 1.15 for the G8 and K5 stars, and above 2.0 for the M1 star. These values are presented in Table 4.1. One can see that σ increases as the observations are done with a higher airmass. By considering only observations made with the target star at an airmass of less than 1.15, we obtained a difference in σ of 15.1% for the G8 star and of 2.4% for the K5, and neglecting airmasses above 2.0 fore the M1 star we found a difference of 1.6%. One should note that the spectra used to calculate the impact for the different spectral
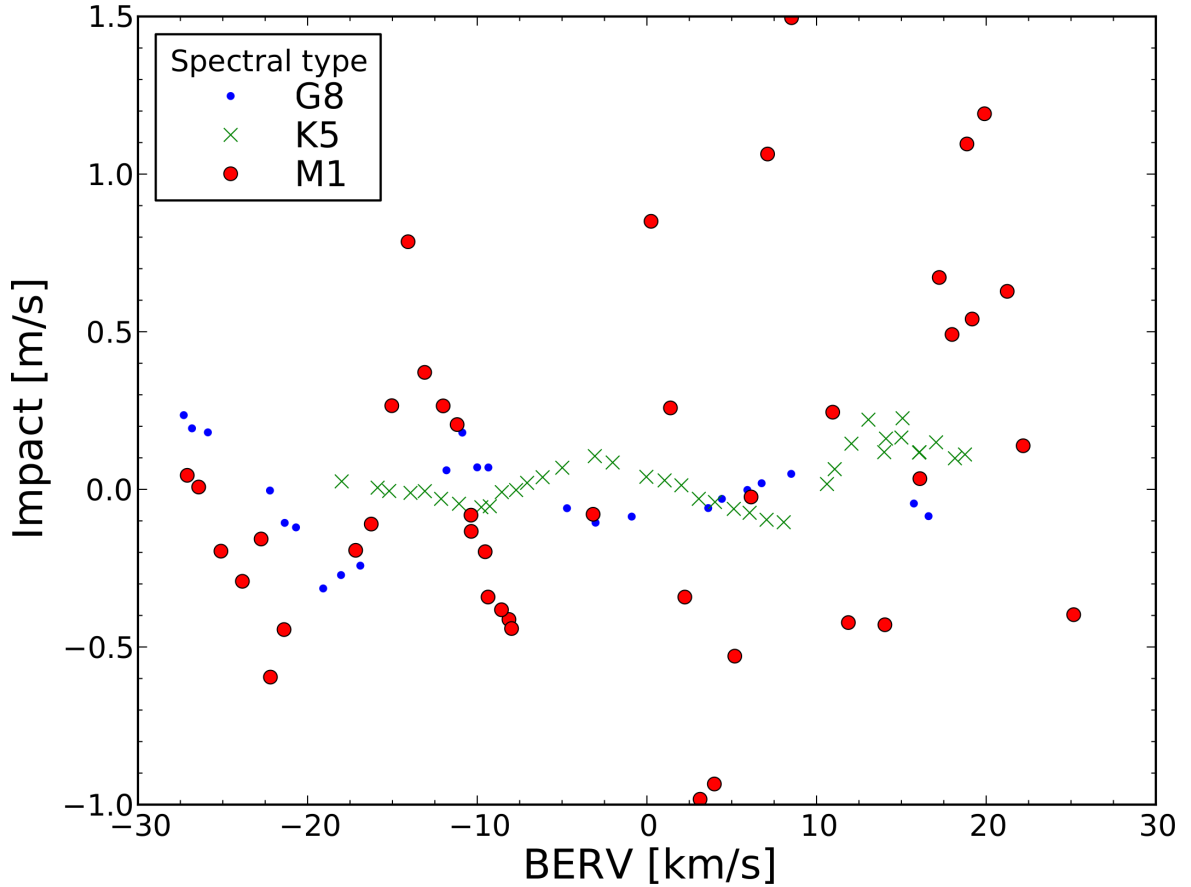
Figure 4.6: Impact of the atmosphere in the radial velocities for different BERV (Barycentric Earth Radial Velocity) values. A star of spectral type G is represented in small blue dots, a K star in green x crosses, and an M big red dots.

types were taken in different nights, and at different hours. Therefore, it is difficult to make a direct comparison between the impact of the atmosphere for the different spectral types. Nevertheless, we can envision a periodic variation of the impact with the BERV, which is more clear for the G8 and K5 stars.

4.5   Discussion and Conclusions

The work done and presented in this chapter allowed us to show that micro-telluric lines should be considered in the calculation of RVs at the level of sub-m s^{-1}. Our test case using synthetic spectra (see Fig. 4.4) shows a maximum impact of $96.2\,\mathrm{cm\,s^{-1}}$ for an airmass of 2. This is $46\,\mathrm{cm\,s^{-1}}$ more than when the star is at the zenith (airmass = 1). Thus, even if the $50.1\,\mathrm{cm\,s^{-1}}$ of impact for the minimum value of the airmass could be explained by systematics, the difference of $46\,\mathrm{cm\,s^{-1}}$ difference between the minimum and the maximum airmass can only be explained as a consequence of contamination by the micro-telluric lines. A $46\,\mathrm{cm\,s^{-1}}$

Table 4.1: Standard deviation, σ, of the relation between the impact of the atmosphere and the radial velocity of the star, depending on the airmass at the time of the observation.

Spect. Type	Airmass	σ $[\mathrm{ms^{-1}}]$
G2 (synth.)	1.0	0.173
	1.15	0.199
	2.0	0.336
G8	all	0.139
	< 1.15	0.118
K5	all	0.085
	< 1.15	0.83
M1	all	0.555
	< 2.0	0.546

impact is in the limit of HARPS precision, and it is larger than the predicted precision for ESPRESSO. Thus the Earth's atmosphere absorption should be corrected for when looking for Earth-size extra-solar planets in Earth-like orbits.

In Sect. 4.4 we divided HARPS spectra by atmospheric spectra modeled with TAPAS in order to correct the effect of the Earth's atmosphere spectral features not neglected by the stellar masks used by HARPS pipeline. When we corrected the stellar spectra of one star taken along one night (Fig. 4.5) we obtained a linear variation of the impact with the airmass, as observed also with the synthetic spectra. However, the atmospheric data is only updated every six hours. Therefore, the atmospheric spectra used in the correction might not be the spectra corresponding to the exact hour of the stellar observation, and so it may lead to an under/over correction of the stellar spectra. This is specially true when there is a change in the weather conditions. This should be the reason for the observed jump of $2.8\,\mathrm{cm\,s^{-1}}$ in the impact, previously presented in Fig.4.5.

The changes of the weather conditions, and the airmass variation are not the only factors involved in the micro-telluric lines effect. As one saw from Fig.4.6, there is also a variation with BERV, i.e., a periodic variation along the year. This periodic variation is clear, particularly for the G8 and K5 stars. For the M1 star this variation is not so clear. This might be because of the other factors that contribute for the atmospheric impact in the RVs: the spectra was taken along the year, and so, they were taken in different nights. thus under different conditions. The ESO atmospheric conditions archive for La Silla is not always available for the nights of observation, so we cannot confirm our hypothesis, but the most probable scenario is that in which there are significantly different weather conditions of the several nights. Moreover, as one can see from Table B.1, the airmass is not constant. Therefore, in addition to he BERV effect one also have the effect of the other factors that contribute to the impact of the micro-telluric lines in the RV calculation. From Fig. 4.6 one can also see that the impact

of Earth's atmosphere on RV is more problematic for the M1 star. This can be because of the high airmass values. This star is always near the horizon and so its airmass values are always above 1.7. One way of testing our micro-telluric correction is to calculate the rms for the RV points taken along one night, before and after the correction of the atmospheric lines. The rms is expected to be smaller after the correction of the telluric lines, i.e., that the RV points will be less dispersed. Unfortunately, HARPS currently available data does not permit to comfirm this. We would need asteroseismology time series observation for stars of spectral type K-M, which we expect to suffer a higher contamination from the atmosphere (Fig. 4.6). But there is no asteroseismology data for stars of these spectral types. We tested then for stars of spectral type G: *18 Sco* (G2) and *Tau Ceti* (G8). Although for some data sets there was, as expected, a decrease in the dispersion, the maximum improvement was marginal: $0.86\,\mathrm{cm\,s^{-1}}$ for *18 Sco* and $0.26\,\mathrm{cm\,s^{-1}}$ for *Tau Ceti*. With present-day data we cannot thus completely test the gain when correcting the telluric absorption. The impact of the micro-telluric lines in these G-type stars RV is of the order of $10-20\,\mathrm{cm\,s^{-1}}$, which is lower than the value of HARPS uncertainty along one night (Dumusque et al. 2011). Therefore, we are most probably dominated by instrumentation/calibration noise and not by the atmospheric contamination.

In addition to the factors considered in this work, others should be investigated. Of these we highlight the wind direction and speed variations, that may induce a shift in the atmospheric spectral lines.

We also want to note the lack of error bars in our figures, when working with HARPS spectra. Because the impact value is estimated using the same original stellar spectrum, with and without atmosphere, and the removal of the atmospheric lines is made using an error-free synthetic atmospheric spectrum, the error on the impact will just be the difference between the estimated RV uncertainties for the case with and without atmosphere. To have an idea of these errors, we present the *18 Sco* values when the star is at its lowest and highest airmass. In the first case (airmass = 1.070) the error will be of $2.1\,\mathrm{cm\,s^{-1}}$, and in the second (airmass = 2.182) it will be of $3.4\,\mathrm{cm\,s^{-1}}$.

Chapter 5

Conclusions and Future work

The work done for this thesis enables us to have a characterization of a couple of noise sources that can influence the detection of extra-solar planets using the radial velocity method. This is the case in which we have a stellar companion inside the fiber, and the case of the contamination by the telluric-lines that are not-neglected by the mask used in the CCF. With the obtained results, we can say that, indeed, we must take extra precautions when observing and analyzing future data. This is especially true when future instruments with very high precision, and capable of detecting signals caused by an Earth-size planet around a Sun-like star in one year orbit, become available.

From this point, we should double check the exoplanetary detections, using diagnosis methods, like the bisector method and the correlation using different templates, as was discussed in Cap. 3. We should also choose wisely the target stars. As was also discussed in Cap. 3, further the target star stands from us, higher is the probability of having light from a companion star entering the fiber that can contaminate the target spectrum.

This thesis is important, because it already provides reference values for several possible sources of contamination when using a fiber-fed spectrograph data for the RV calculation, and is a good start to the characterization of the new noise sources arising with the future levels of high precision RVs, it is not enough and more work needs to be done. We saw in Cap. 4 that the micro-telluric lines imprinted in the stellar spectra may become a limiting factor to the high precision, instead of the actual photon noise. Therefore, we should be more careful handling these lines. An option is to neglect these, until now, not-neglected shallow lines. This would mean to neglect also more stellar lines, and loose more stellar information. The other option is to correct for these lines.

In the last few years we witnessed an increase in the usage of modeled atmospheric spectra. As an example the reader can look at the work of Seifahrt et al. (2010)), and to the work

of Cunha et al. (2014) (also presented in Cap. 4). Consequently, we witnessed, as well, an increasing number of atmospheric models. For reference, we mention the SMART (Bailey et al. 2007), TAPAS (Bertaux, J. L. et al. 2014), and the Molecfit (Smette et al. 2014; Kausch et al. 2014) model. If one wants to achieve the required high precision to find an Earth-like planet, one needs to evaluate the different existing atmospheric models and seek for the one that best corrects the stellar spectra. Currently, Pace et al. (2014) is also developing at Centro de Astrofísica da Universidade do Porto a platform for manipulation of the efficient and highly flexible model LBLRTM (see Sect. 4.2.1 and Appendix C for details on this model). Because these models depend on atmospheric data gathered by satellites, it would also be important to improve this correction method by improving the collected data to be used in the models: more frequent, and localized data.

One of the telluric features still left to explore is the wind. In the future, we want to address how the wind speed and direction affects the telluric lines stability and the consequent effect in the RV determination. When exploring the telluric atmosphere modeling tools, one has to evaluate which one best incorporate the wind data.

Following the work of Cunha et al. (2014) presented in Cap. 4, we should improve in the future the stellar spectra continuum derivation, and make the correction from telluric lines a more automatic and generalized method. By doing so we expect that our method can be used in the future for a large range of spectra taken with different instruments, being of good use not only for the planet searches with RVs, but also for other areas of Astronomy, like chemical abundances or exoplanetary atmospheres.

Making it generalized we want it to be able to correct telluric lines not only in the visible. In particular, we want it to correct stellar spectra in the near-IR, where the contamination is much higher. Therefore, we also want to test the atmospheric transmission models in the infrared, in order to be able to correct for its effect and increase the number of stellar spectral lines used in the RV calculation, and so also increase the stellar spectral information. The telluric spectra in near-IR wavelengths is populated with telluric lines. As an example we have the CO_2 lines at 1.6 μm, and the CH_4 at 2.32 μm. The correction of the telluric lines in these wavelengths is very important in the planetary searches area (e.g. Figueira et al. 2010b). Observations in the near-IR are useful in the diagnosis of false positives caused by spots (e.g. Huélamo et al. 2008). The near-IR is also the best spectral band in the observation of stars of spectral type M (cooler stars), which have a life expectancy big enough to allow planets develop life, if conditions are reunited.

Within three years, the new generation of spectrographs will start to become available. In 2017 we will have not only the ESPRESSO first-light, but also SPIRou [1], a near-IR spectropolarimeter covering the near-infrared domain up to the K band with a resolution over

---

[1]http://www.cfht.hawaii.edu/en/projects/SPIRou/

70,000. It is expected it to achieve a precision of $1\,\mathrm{m\,s^{-1}}$. To achieve this level of precision, SPIRou will have an Farby-Pérot etalon for wavelength calibration. But this technology is currently not yet easily available. If one wants to get a precision in the level of the few $\mathrm{m\,s^{-1}}$ in the IR, one needs to use a simultaneous wavelength reference. The problem is that the more common wavelength calibrator used in the visible, the Th-Ar emission lamp and the I_2 absorption cell presented in Sections 2.3.1 and 2.3.2, are difficult to use in the IR. The Th-Ar lamp has a lower density of spectral lines in the IR than in the visible wavelengths, and there are no known gas providing a dense absorption lines in a wide wavelength in the IR. An alternative to use spectral lines from the molecular species of Earth's atmosphere, whose rotational and vibrational features are in the IR (e.g. Figueira et al. 2010c). However, as seen in Cap.4, telluric features may vary with the atmospheric conditions. Thus, a better knowledge of the telluric spectra and of its modeling will also be an asset for IR wavelength calibration.

Bibliography

Auvergne, M., Bodin, P., Boisnard, L., et al. 2009, A&A, 506, 411

Baglin, A., Michel, E., Auvergne, M., & COROT Team. 2006, in ESA Special Publication, Vol. 624, Proceedings of SOHO 18/GONG 2006/HELAS I, Beyond the spherical Sun

Bailey, J., Simpson, A., & Crisp, D. 2007, PASP, 119, 228

Baranne, A., Queloz, D., Mayor, M., et al. 1996, A&AS, 119, 373

Batalha, N. M., Rowe, J. F., Bryson, S. T., et al. 2012, ArXiv e-prints

Bertaux, J. L., Lallement, R., Ferron, S., Boonne, C., & Bodichon, R. 2014, A&A, 564, A46

Binzel, R. P. 2006, Minor Planet Bulletin, 33, 106

Borucki, W. J., Koch, D., Basri, G., et al. 2010, Science, 327, 977

Boss, A. P., Basri, G., Kumar, S. S., et al. 2003, in IAU Symposium, Vol. 211, Brown Dwarfs, ed. E. Martín, 529

Buchhave, L. A., Latham, D. W., Carter, J. A., et al. 2011, ApJS, 197, 3

Butler, R. P., Marcy, G. W., Williams, E., et al. 1996, PASP, 108, 500

Casertano, S., Lattanzi, M. G., Sozzetti, A., et al. 2008, A&A, 482, 699

Cegla, H. M., Watson, C. A., Marsh, T. R., et al. 2012, MNRAS, 421, L54

Chabrier, G., Johansen, A., Janson, M., & Rafikov, R. 2014, ArXiv e-prints

Charbonneau, D., Brown, T. M., Latham, D. W., & Mayor, M. 2000, ApJ, 529, L45

Chromey, F. R. 2010, To Measure the Sky

Clough, S. A., Iacono, M. J., & Moncet, J.-L. 1992, J. Geophys. Res., 97, 15761

Clough, S. A., Kneizys, F. X., Rothman, L. S., & Gallery, W. O. 1981, in Society of Photo-Optical Instrumentation Engineers (SPIE) Conference Series, Vol. 277, Society of Photo-Optical Instrumentation Engineers (SPIE) Conference Series, 152–166

Clough, S. A., Shephard, M. W., Mlawer, E. J., et al. 2005, J. Quant. Spec. Radiat. Transf., 91, 233

Correia, A. C. M., Couetdic, J., Laskar, J., et al. 2010, A&A, 511, A21

Cosentino, R., Lovis, C., Pepe, F., et al. 2012, in Society of Photo-Optical Instrumentation Engineers (SPIE) Conference Series, Vol. 8446, Society of Photo-Optical Instrumentation Engineers (SPIE) Conference Series, 1

Cotton, D. V., Bailey, J., & Kedziora-Chudczer, L. 2013, ArXiv e-prints

Cumming, A., Marcy, G. W., & Butler, R. P. 1999, ApJ, 526, 890

Cunha, D., Figueira, P., Santos, N. C., Lovis, C., & Boué, G. 2013, A&A, 550, A75

Cunha, D., Santos, N. C., Figueira, P., et al. 2014, A&A, 568, A35

de Bruijne, J. H. J. 2012, Ap&SS, 341, 31

Dumusque, X., Pepe, F., Lovis, C., et al. 2012, Nature, 491, 207

Dumusque, X., Udry, S., Lovis, C., Santos, N. C., & Monteiro, M. J. P. F. G. 2011, A&A, 525, A140

Duquennoy, A. & Mayor, M. 1991, A&A, 248, 485

Duric, N. 2003, Advanced Astrophysics

Figueira, P. 2010, PhD thesis, Observatoire de Genève

Figueira, P., Kerber, F., Chacon, A., et al. 2012, MNRAS, 420, 2874

Figueira, P., Marmier, M., Bonfils, X., et al. 2010a, A&A, 513, L8

Figueira, P., Pepe, F., Lovis, C., & Mayor, M. 2010b, A&A, 515, A106+

Figueira, P., Pepe, F., Melo, C. H. F., et al. 2010c, A&A, 511, A55

Fischer, J., Gamache, R. R., Goldman, A., Rothman, L. S., & Perrin, A. 2003, J. Quant. Spec. Radiat. Transf., 82, 401

Glass, I. S. 1999, Handbook of Infrared Astronomy, ed. R. Ellis, J. Huchra, S. Kahn, G. Rieke, & P. B. Stetson

Howell, S. B. 2006, Handbook of CCD Astronomy, ed. R. Ellis, J. Huchra, S. Kahn, G. Rieke, & P. B. Stetson

Huélamo, N., Figueira, P., Bonfils, X., et al. 2008, A&A, 489, L9

Janesick, J. R. 2001, Scientific charge-coupled devices

Janson, M., Hormuth, F., Bergfors, C., et al. 2012, ApJ, 754, 44

Kalas, P., Graham, J. R., Chiang, E., et al. 2008, Science, 322, 1345

Karttunen, H., Krüger, P., Oja, H., Poutanen, M., & Donner, K. J., eds. 2007, Fundamental Astronomy

Kausch, W., Noll, S., Smette, A., et al. 2014, subm. to A&A

Koch, D. G., Borucki, W. J., Basri, G., et al. 2010, ApJ, 713, L79

Kupka, F., Piskunov, N., Ryabchikova, T. A., Stempels, H. C., & Weiss, W. W. 1999, A&AS, 138, 119

Kupka, F. G., Ryabchikova, T. A., Piskunov, N. E., Stempels, H. C., & Weiss, W. W. 2000, Baltic Astronomy, 9, 590

Lamouroux, J., Tran, H., Laraia, A. L., et al. 2010, J. Quant. Spec. Radiat. Transf., 111, 2321

Li, C.-H., Benedick, A. J., Fendel, P., et al. 2008, Nature, 452, 610

Lovis, C. & Pepe, F. 2007, A&A, 468, 1115

Maiolino, R., Haehnelt, M., Murphy, M. T., et al. 2013, ArXiv e-prints

Marcy, G. W. & Butler, R. P. 1992, PASP, 104, 270

Marois, C., Lafrenière, D., Doyon, R., Macintosh, B., & Nadeau, D. 2006, ApJ, 641, 556

Marois, C., Macintosh, B., Barman, T., et al. 2008, Science, 322, 1348

Martins, J. H. C. 2013, Master's thesis, Faculdade de Ciências da Universidade do Porto

Massey, P. & Hanson, M. M. 2013, Astronomical Spectroscopy, ed. T. D. Oswalt & H. E. Bond, 35

Mayor, M., Bonfils, X., Forveille, T., et al. 2009, A&A, 507, 487

Mayor, M., Pepe, F., Queloz, D., et al. 2003, The Messenger, 114, 20

Mayor, M. & Queloz, D. 1995, Nature, 378, 355

Morton, D. C. 1991, ApJS, 77, 119

Murphy, M. T., Udem, T., Holzwarth, R., et al. 2007, MNRAS, 380, 839

Niro, F., Jucks, K., & Hartmann, J.-M. 2005, J. Quant. Spec. Radiat. Transf., 95, 469

Pace, G., Figueira, P., Santos, N. C., & Cunha, D. 2014, in prep.

Pepe, F., Mayor, M., Galland, F., et al. 2002, A&A, 388, 632

Pepe, F. A., Cristiani, S., Rebolo Lopez, R., et al. 2010, in Society of Photo-Optical In-
    strumentation Engineers (SPIE) Conference Series, Vol. 7735, Society of Photo-Optical
    Instrumentation Engineers (SPIE) Conference Series

Perryman, M. 2011, The Exoplanet Handbook

Perryman, M., Hartman, J., Bakos, G. A., & Lindegren, L. 2014, The Astrophysical Journal,
    797, 14

Piskunov, N. E., Kupka, F., Ryabchikova, T. A., Weiss, W. W., & Jeffery, C. S. 1995, A&AS,
    112, 525

Queloz, D., Henry, G. W., Sivan, J. P., et al. 2001, A&A, 379, 279

Queloz, D., Udry, S., Mayor, M., et al., eds. 2006, Extrasolar planets

Reffert, S. & Quirrenbach, A. 2011, A&A, 527, A140

Robin, A. C., Reylé, C., Derrière, S., & Picaud, S. 2003, A&A, 409, 523

Ryabchikova, T. A., Piskunov, N. E., Kupka, F., & Weiss, W. W. 1997, Baltic Astronomy, 6,
    244

Santos, N. C., Bouchy, F., Mayor, M., et al. 2004, A&A, 426, L19

Santos, N. C., Mayor, M., Naef, D., et al. 2002, A&A, 392, 215

Schwab, C., Stuermer, J., Gurevich, Y. V., et al. 2014, ArXiv e-prints

Seager, S. 2011, Exoplanets

Seifahrt, A., Käufl, H. U., Zängl, G., et al. 2010, A&A, 524, A11

Shephard, M. W., Clough, S. A., Payne, V. H., et al. 2009, Atmospheric Chemistry & Physics,
    9, 7397

Smette, A., Sana, H., Noll, S., et al. 2014, subm. to A&A

Sneden, C. A. 1973, PhD thesis, The University of Texas at Austin

Sozzetti, A. 2010, in EAS Publications Series, Vol. 42, EAS Publications Series, ed. K. Goździewski, A. Niedzielski, & J. Schneider, 55–77

Sutton, E. C. 2011, Observational Astronomy

Tennyson, J. 2005, Astronomical spectroscopy : an introduction to the atomic and molecular physics of astronomical spectra

Tripathi, A., Winn, J. N., Johnson, J. A., et al. 2010, ApJ, 715, 421

Turner, D. D., Tobin, D. C., Clough, S. A., et al. 2004, Journal of Atmospheric Sciences, 61, 2657

Udalski, A., Kubiak, M., & Szymanski, M. 1997, Acta Astron., 47, 319

Vacca, W. D., Cushing, M. C., & Rayner, J. T. 2003, PASP, 115, 389

Wildi, F., Chazelas, B., & Pepe, F. 2012, in Society of Photo-Optical Instrumentation Engineers (SPIE) Conference Series, Vol. 8446, Society of Photo-Optical Instrumentation Engineers (SPIE) Conference Series, 8

Wildi, F., Pepe, F., Chazelas, B., Lo Curto, G., & Lovis, C. 2010, in Society of Photo-Optical Instrumentation Engineers (SPIE) Conference Series, Vol. 7735, Society of Photo-Optical Instrumentation Engineers (SPIE) Conference Series, 4

Wildi, F., Pepe, F., Chazelas, B., Lo Curto, G., & Lovis, C. 2011, in Society of Photo-Optical Instrumentation Engineers (SPIE) Conference Series, Vol. 8151, Society of Photo-Optical Instrumentation Engineers (SPIE) Conference Series, 1

Wilken, T., Curto, G. L., Probst, R. A., et al. 2012, Nature, 485, 611

Winn, J. N. 2010, ArXiv e-prints

Wolszczan, A. & Frail, D. A. 1992, Nature, 355, 145

Appendix A

Density of stars

```
30│ 0.0e+00 0.0e+00 0.0e+00 0.0e+00 0.0e+00 0.0e+00 0.0e+00 0.0e+00 0.0e+00 0.0e+00 0.0e+00 8.6e+02 6.7e+03 3.1e+03 3.7e+05
   │ 0.0e+00 0.0e+00 0.0e+00 0.0e+00 0.0e+00 0.0e+00 0.0e+00 0.0e+00 0.0e+00 0.0e+00 0.0e+00 1.4e+04 1.3e+04 4.4e+04 7.5e+05
   │ 0.0e+00 0.0e+00 0.0e+00 0.0e+00 0.0e+00 0.0e+00 0.0e+00 0.0e+00 0.0e+00 0.0e+00 0.0e+00 3.2e+04 2.5e+04 2.7e+05 6.3e+05
   │ 0.0e+00 0.0e+00 0.0e+00 0.0e+00 0.0e+00 0.0e+00 0.0e+00 0.0e+00 0.0e+00 0.0e+00 6.9e+02 3.8e+04 9.3e+04 6.0e+05 3.5e+05
   │ 0.0e+00 0.0e+00 0.0e+00 0.0e+00 0.0e+00 0.0e+00 0.0e+00 0.0e+00 0.0e+00 1.0e+02 8.5e+03 3.0e+04 3.5e+05 6.2e+05 1.4e+05
25│ 0.0e+00 0.0e+00 0.0e+00 0.0e+00 0.0e+00 0.0e+00 0.0e+00 0.0e+00 2.8e+03 3.6e+03 9.8e+03 3.5e+04 6.6e+05 3.5e+05 4.5e+04
   │ 0.0e+00 0.0e+00 0.0e+00 0.0e+00 0.0e+00 0.0e+00 0.0e+00 3.7e+03 6.9e+03 2.9e+03 7.1e+03 6.6e+04 7.0e+05 1.4e+05 1.4e+04
   │ 0.0e+00 0.0e+00 0.0e+00 0.0e+00 0.0e+00 0.0e+00 1.2e+03 7.2e+03 5.0e+03 2.3e+03 1.1e+04 9.9e+04 5.4e+05 4.6e+04 4.3e+03
   │ 0.0e+00 0.0e+00 0.0e+00 0.0e+00 0.0e+00 0.0e+00 2.3e+03 5.7e+03 5.2e+03 7.2e+03 2.9e+04 1.4e+05 3.2e+05 1.4e+04 1.3e+03
   │ 8.0e+00 0.0e+00 0.0e+00 0.0e+00 0.0e+00 0.0e+00 1.7e+03 6.1e+03 1.6e+04 2.0e+04 6.1e+04 1.5e+05 1.4e+05 4.3e+03 3.6e+02
20│ 1.5e+01 1.1e+01 5.0e+00 3.0e+00 0.0e+00 1.0e+00 1.1e+03 1.9e+04 3.3e+04 3.4e+04 1.1e+05 1.0e+05 5.0e+04 1.2e+03 9.2e+01
   │ 8.0e+00 1.9e+01 9.0e+00 1.6e+01 0.0e+00 9.0e+00 6.1e+02 3.6e+04 5.1e+04 5.6e+04 9.6e+04 4.4e+04 1.6e+04 3.6e+02 3.1e+01
   │ 2.0e+00 8.0e+00 5.0e+00 8.0e+00 0.0e+00 5.0e+00 2.1e+02 4.2e+04 7.5e+04 4.9e+04 5.0e+04 1.5e+04 4.7e+03 9.2e+01 8.0e+00
   │ 3.0e+00 2.0e+00 6.0e+00 5.0e+00 0.0e+00 5.0e+00 2.8e+02 4.2e+04 6.1e+04 2.9e+04 2.0e+04 4.7e+03 1.5e+03 3.4e+01 1.0e+00
   │ 3.0e+00 3.0e+00 2.0e+00 6.0e+00 0.0e+00 4.6e+01 1.4e+03 3.1e+04 2.9e+04 1.3e+04 9.4e+03 1.5e+03 4.5e+02 8.0e+00 0.0e+00
15│ 1.0e+00 0.0e+00 0.0e+00 2.0e+00 3.4e+01 3.2e+02 2.8e+03 1.6e+04 1.1e+04 5.7e+03 7.3e+03 5.2e+02 1.4e+02 1.0e+00 0.0e+00
   │ 0.0e+00 0.0e+00 0.0e+00 7.0e+00 1.7e+02 6.8e+02 2.6e+03 6.2e+03 3.3e+03 2.2e+03 6.4e+03 4.9e+02 1.5e+02 4.0e+00 2.0e+00
   │ 0.0e+00 0.0e+00 0.0e+00 2.5e+01 2.9e+02 6.8e+02 1.4e+03 2.0e+03 1.0e+03 9.3e+02 3.8e+03 5.0e+02 2.7e+02 2.8e+01 1.0e+00
   │ 0.0e+00 0.0e+00 0.0e+00 5.2e+01 2.7e+02 4.3e+02 5.7e+02 6.5e+02 3.0e+02 3.6e+02 1.6e+03 3.3e+02 2.5e+02 3.6e+01 1.0e+00
   │ 0.0e+00 0.0e+00 0.0e+00 5.5e+01 1.6e+02 2.0e+02 2.1e+02 2.0e+02 7.7e+01 1.0e+02 5.4e+02 1.4e+02 1.2e+02 3.2e+01 2.0e+00
10│ 0.0e+00 0.0e+00 0.0e+00 3.3e+01 7.1e+01 6.8e+01 7.3e+01 5.4e+01 2.6e+01 3.8e+01 2.2e+02 4.2e+01 4.4e+01 8.0e+00 0.0e+00
   │ 0.0e+00 0.0e+00 0.0e+00 1.7e+01 3.1e+01 1.9e+01 1.3e+01 1.0e+01 6.0e+00 2.1e+01 7.6e+01 1.6e+01 9.0e+00 2.0e+00 0.0e+00
   │ 0.0e+00 0.0e+00 0.0e+00 1.2e+01 9.0e+00 6.0e+00 8.0e+00 7.0e+00 4.0e+00 7.0e+00 1.7e+01 4.0e+00 1.0e+00 2.0e+00 0.0e+00
   │ 0.0e+00 0.0e+00 1.0e+00 4.0e+00 2.0e+00 4.0e+00 2.0e+00 1.0e+00 1.0e+00 1.0e+00 2.0e+00 0.0e+00 0.0e+00 0.0e+00 0.0e+00
   │ 0.0e+00 0.0e+00 3.0e+00 3.0e+00 1.0e+00 1.0e+00 0.0e+00 0.0e+00 0.0e+00 0.0e+00 3.0e+00 1.0e+00 2.0e+00 1.0e+00 0.0e+00
 5│ 0.0e+00 0.0e+00 0.0e+00 0.0e+00 0.0e+00 0.0e+00 0.0e+00 0.0e+00 0.0e+00 0.0e+00 2.0e+00 1.0e+00 0.0e+00 0.0e+00 0.0e+00
   │ 0.0e+00 0.0e+00 0.0e+00 2.0e+00 0.0e+00 0.0e+00 0.0e+00 0.0e+00 0.0e+00 0.0e+00 0.0e+00 0.0e+00 0.0e+00 0.0e+00 0.0e+00
   │ 0.0e+00 0.0e+00 0.0e+00 0.0e+00 0.0e+00 0.0e+00 0.0e+00 0.0e+00 0.0e+00 0.0e+00 0.0e+00 0.0e+00 0.0e+00 0.0e+00 0.0e+00
   │ 0.0e+00 0.0e+00 0.0e+00 0.0e+00 0.0e+00 0.0e+00 0.0e+00 0.0e+00 0.0e+00 0.0e+00 0.0e+00 0.0e+00 0.0e+00 0.0e+00 0.0e+00
   │ 0.0e+00 0.0e+00 0.0e+00 0.0e+00 0.0e+00 0.0e+00 0.0e+00 0.0e+00 0.0e+00 0.0e+00 0.0e+00 0.0e+00 0.0e+00 0.0e+00 0.0e+00
 0│ 0.0e+00 0.0e+00 0.0e+00 0.0e+00 0.0e+00 0.0e+00 0.0e+00 0.0e+00 0.0e+00 0.0e+00 0.0e+00 0.0e+00 0.0e+00 0.0e+00 0.0e+00
   └─────────────────────────────────────────────────────────────────────────────────────────────────────────────────────
    [O0,O5[  [O5,B0[  [B0,B5[  [B5,A0[  [A0,A5[  [A5,F0[  [F0,F5[  [F5,G0[  [G0,G5[  [G5,K0[  [K0,K5[  [K5,M0[  [M0,M5[  [M5,M8[  [M8,M9]
```

Figure A.1: Number of stars in each bin of spectral type and magnitude for an area of the sky with a radius of 3°.

mag	[O0,O5[	[O5,B0[	[B0,B5[	[B5,A0[	[A0,A5[	[A5,F0[	[F0,F5[	[F5,G0[	[G0,G5[	[G5,K0[	[K0,K5[	[K5,M0[	[M0,M5[	[M5,M8[	[M8,M9]
30	0.0e+00	0.0e+00	0.0e+00	0.0e+00	0.0e+00	0.0e+00	0.0e+00	0.0e+00	0.0e+00	0.0e+00	0.0e+00	1.8e-06	1.4e-05	6.5e-06	7.9e-04
	0.0e+00	0.0e+00	0.0e+00	0.0e+00	0.0e+00	0.0e+00	0.0e+00	0.0e+00	0.0e+00	0.0e+00	0.0e+00	3.1e-05	2.8e-05	9.4e-05	1.6e-03
	0.0e+00	0.0e+00	0.0e+00	0.0e+00	0.0e+00	0.0e+00	0.0e+00	0.0e+00	0.0e+00	0.0e+00	0.0e+00	7.0e-05	5.4e-05	5.8e-04	1.3e-03
	0.0e+00	0.0e+00	0.0e+00	0.0e+00	0.0e+00	0.0e+00	0.0e+00	0.0e+00	0.0e+00	0.0e+00	0.0e+00	5.4e-05	2.0e-04	1.3e-03	7.4e-04
	0.0e+00	0.0e+00	0.0e+00	0.0e+00	0.0e+00	0.0e+00	0.0e+00	0.0e+00	0.0e+00	0.0e+00	0.0e+00	2.0e-04	7.5e-04	7.6e-04	3.0e-04
25	0.0e+00	0.0e+00	0.0e+00	0.0e+00	0.0e+00	0.0e+00	0.0e+00	0.0e+00	0.0e+00	0.0e+00	0.0e+00	8.2e-05	2.3e-04	1.4e-04	9.7e-05
	0.0e+00	0.0e+00	0.0e+00	0.0e+00	0.0e+00	0.0e+00	0.0e+00	0.0e+00	0.0e+00	0.0e+00	0.0e+00	1.6e-05	1.3e-04	1.5e-05	3.0e-05
	0.0e+00	0.0e+00	0.0e+00	0.0e+00	0.0e+00	0.0e+00	0.0e+00	0.0e+00	0.0e+00	0.0e+00	0.0e+00	1.2e-05	2.1e-05	1.2e-03	9.2e-06
	0.0e+00	0.0e+00	0.0e+00	0.0e+00	0.0e+00	0.0e+00	0.0e+00	0.0e+00	0.0e+00	0.0e+00	0.0e+00	1.1e-05	1.5e-05	9.8e-04	2.7e-06
	0.0e+00	0.0e+00	0.0e+00	0.0e+00	0.0e+00	0.0e+00	0.0e+00	0.0e+00	0.0e+00	0.0e+00	0.0e+00	1.5e-05	6.3e-05	6.8e-04	7.6e-07
20	0.0e+00	0.0e+00	0.0e+00	0.0e+00	1.9e-08	2.1e-09	2.3e-06	4.0e-05	7.0e-05	2.3e-04	2.2e-04	1.1e-04	3.0e-04	9.3e-06	2.0e-07
	1.7e-08	4.1e-08	3.4e-08	1.9e-08	0.0e+00	1.3e-06	7.8e-05	1.2e-04	2.3e-04	9.5e-05	3.4e-05	1.2e-04	2.7e-06	7.8e-07	6.6e-08
	4.3e-09	1.7e-08	1.7e-08	0.0e+00	1.1e-08	4.5e-07	9.0e-05	1.6e-04	1.1e-04	3.3e-05	1.0e-05	2.0e-05	7.3e-08	2.0e-07	1.7e-08
	6.4e-09	4.3e-09	1.3e-08	0.0e+00	9.9e-08	6.0e-07	8.9e-05	6.1e-05	2.9e-05	1.0e-05	3.2e-06	7.3e-06	1.7e-08	0.0e+00	2.1e-09
	2.1e-09	0.0e+00	4.3e-09	7.3e-08	6.9e-07	5.9e-06	3.4e-05	2.3e-05	2.0e-05	1.6e-05	1.1e-06	3.0e-07	2.1e-08	0.0e+00	0.0e+00
15	0.0e+00	0.0e+00	0.0e+00	1.5e-08	1.5e-08	5.6e-06	1.3e-05	7.2e-06	4.7e-06	1.4e-05	1.1e-06	3.3e-07	8.6e-09	0.0e+00	0.0e+00
	0.0e+00	0.0e+00	0.0e+00	3.7e-07	5.6e-06	1.3e-05	4.2e-06	2.0e-06	1.6e-05	3.0e-07	5.8e-07	6.0e-08	4.3e-09	0.0e+00	0.0e+00
	0.0e+00	0.0e+00	0.0e+00	6.2e-07	1.5e-06	3.0e-06	2.1e-06	2.0e-06	8.1e-06	1.1e-06	5.8e-07	6.0e-08	2.1e-09	0.0e+00	4.3e-09
	0.0e+00	0.0e+00	0.0e+00	5.4e-08	9.1e-07	1.2e-06	1.4e-06	6.4e-07	3.4e-06	7.0e-07	5.3e-07	7.7e-08	0.0e+00	0.0e+00	2.1e-09
	0.0e+00	0.0e+00	0.0e+00	1.1e-07	3.4e-07	4.5e-07	1.7e-07	2.3e-07	1.2e-06	3.0e-07	2.5e-07	6.9e-08	0.0e+00	0.0e+00	4.3e-09
10	0.0e+00	0.0e+00	0.0e+00	7.1e-08	1.5e-07	2.8e-08	1.2e-07	8.1e-08	4.7e-07	9.0e-08	9.4e-08	1.7e-08	0.0e+00	0.0e+00	0.0e+00
	0.0e+00	0.0e+00	3.6e-08	6.6e-08	4.1e-08	2.8e-08	1.3e-08	4.5e-08	1.6e-07	3.4e-08	1.9e-08	4.3e-09	0.0e+00	0.0e+00	0.0e+00
	0.0e+00	0.0e+00	2.6e-08	1.9e-08	1.3e-08	1.7e-08	1.5e-08	1.5e-08	3.6e-08	8.6e-09	2.1e-09	4.3e-09	0.0e+00	0.0e+00	0.0e+00
	0.0e+00	0.0e+00	8.6e-09	4.3e-09	8.6e-09	4.3e-09	2.1e-09	2.1e-09	4.3e-09	2.1e-09	0.0e+00	0.0e+00	0.0e+00	0.0e+00	0.0e+00
	0.0e+00	0.0e+00	2.1e-09	6.4e-09	2.1e-09	0.0e+00	0.0e+00	2.1e-09	4.3e-09	2.1e-09	0.0e+00	0.0e+00	0.0e+00	0.0e+00	0.0e+00
5	0.0e+00	0.0e+00	6.4e-09	6.4e-09	0.0e+00	0.0e+00	0.0e+00	0.0e+00	4.3e-09	4.3e-09	0.0e+00	0.0e+00	0.0e+00	0.0e+00	0.0e+00
	0.0e+00	0.0e+00	0.0e+00	4.3e-09	0.0e+00	0.0e+00	0.0e+00	0.0e+00	0.0e+00	2.1e-09	0.0e+00	0.0e+00	0.0e+00	0.0e+00	0.0e+00
	0.0e+00	0.0e+00	0.0e+00	0.0e+00	0.0e+00	0.0e+00	0.0e+00	0.0e+00	0.0e+00	0.0e+00	0.0e+00	0.0e+00	0.0e+00	0.0e+00	0.0e+00
	0.0e+00	0.0e+00	0.0e+00	0.0e+00	0.0e+00	0.0e+00	0.0e+00	0.0e+00	0.0e+00	0.0e+00	0.0e+00	0.0e+00	0.0e+00	0.0e+00	0.0e+00
	0.0e+00	0.0e+00	0.0e+00	0.0e+00	0.0e+00	0.0e+00	0.0e+00	0.0e+00	0.0e+00	0.0e+00	0.0e+00	0.0e+00	0.0e+00	0.0e+00	0.0e+00
0	0.0e+00	0.0e+00	0.0e+00	0.0e+00	0.0e+00	0.0e+00	0.0e+00	0.0e+00	0.0e+00	0.0e+00	0.0e+00	0.0e+00	0.0e+00	0.0e+00	0.0e+00

Figure A.2: Density of stars in each bin of spectral type and magnitude for an area of the sky with a radius of 0.5 arcsec.

Appendix B

Star observation properties

Table B.1: Stars used in our simulations, their spectral type, signal to noise ratio at 500 nm, and the program ID of their observation.

Object	Spec. Type	SN50	Airmass	Prog. ID
Tau Ceti	G8	286	1.208	082.C-0315(A)
		229	1.290	082.C-0315(A)
		164	1.042	083.C-1001(A)
		196	1.039	083.C-1001(A)
		308	1.039	083.C-1001(A)
		374	1.034	083.C-1001(A)
		196	1.028	083.C-1001(A)
		287	1.079	083.C-1001(A)
		255	1.033	083.C-1001(A)
		273	1.033	084.C-0229(A)
		269	1.195	084.C-0229(A)
		439	1.030	084.C-0229(A)
		381	1.347	084.C-0229(A)
		346	1.396	084.C-0229(A)
		386	1.401	084.C-0229(A)
		409	1.029	084.C-0229(A)
		198	1.028	084.C-0229(A)
		193	1.123	084.C-0229(A)
		245	1.129	084.C-0229(A)
		218	1.090	084.C-0229(A)
		236	1.067	084.C-0229(A)
Continued on next page				

Object	Spec. Type	SN50	Airmass	Prog. ID
		274	1.067	084.C-0229(A)
		264	1.066	084.C-0229(A)
		300	1.067	084.C-0229(A)
HD85512	K5	201	1.095	072.C-0488(E)
		248	1.032	072.C-0488(E)
		191	1.032	072.C-0488(E)
		184	1.047	072.C-0488(E)
		163	1.037	072.C-0488(E)
		177	1.032	082.C-0315(A)
		187	1.132	082.C-0315(A)
		169	1.032	082.C-0315(A)
		145	1.056	082.C-0315(A)
		160	1.379	082.C-0315(A)
		195	1.140	082.C-0315(A)
		188	1.106	082.C-0315(A)
		205	1.058	082.C-0315(A)
		206	1.064	084.C-0229(A)
		172	1.032	086.C-0230(A)
		178	1.115	086.C-0230(A)
		162	1.267	086.C-0230(A)
		181	1.035	086.C-0230(A)
		196	1.043	086.C-0230(A)
		136	1.033	086.C-0230(A)
		143	1.032	086.C-0230(A)
		152	1.067	086.C-0230(A)
		185	1.047	086.C-0230(A)
		180	1.033	087.C-0990(A)
		202	1.038	087.C-0990(A)
		128	1.126	087.C-0990(A)
		132	1.073	087.C-0990(A)
		159	1.034	087.C-0990(A)
		197	1.076	087.C-0990(A)
		167	1.134	087.C-0990(A)
		182	1.036	087.C-0990(A)
		161	1.078	087.C-0990(A)
				Continued on next page

Object	Spec. Type	SN50	Airmass	Prog. ID
		167	1.122	087.C-0990(A)
		183	1.059	087.C-0990(A)
		195	1.398	088.C-0011(A)
		170	1.066	088.C-0011(A)
		134	1.069	088.C-0011(A)
		163	1.204	088.C-0011(A)
		149	1.287	088.C-0011(A)
		155	1.377	088.C-0011(A)
		137	1.152	088.C-0011(A)
		152	1.210	088.C-0011(A)
Gl436	M1	34	1.788	072.C-0488(E)
		48	1.792	072.C-0488(E)
		44	1.829	072.C-0488(E)
		48	1.790	072.C-0488(E)
		47	1.785	072.C-0488(E)
		39	1.788	072.C-0488(E)
		48	1.815	072.C-0488(E)
		41	1.801	072.C-0488(E)
		30	1.897	072.C-0488(E)
		43	1.807	072.C-0488(E)
		32	1.781	072.C-0488(E)
		54	1.781	072.C-0488(E)
		44	2.256	072.C-0488(E)
		39	2.046	072.C-0488(E)
		43	2.164	072.C-0488(E)
		45	1.780	072.C-0488(E)
		45	1.780	072.C-0488(E)
		41	1.781	072.C-0488(E)
		35	1.780	072.C-0488(E)
		30	2.098	072.C-0488(E)
		50	1.831	072.C-0488(E)
		50	1.785	072.C-0488(E)
		47	1.825	072.C-0488(E)
		44	1.843	072.C-0488(E)
		51	1.781	072.C-0488(E)

Object	Spec. Type	SN50	Airmass	Prog. ID
		34	1.781	072.C-0488(E)
		45	1.821	072.C-0488(E)
		63	1.788	072.C-0488(E)
		35	1.785	072.C-0488(E)
		42	1.784	072.C-0488(E)
		51	2.035	072.C-0488(E)
		47	1.781	072.C-0488(E)
		44	1.791	072.C-0488(E)
		35	1.860	072.C-0488(E)
		32	1.841	082.C-0718(B)
		46	1.780	082.C-0718(B)
		42	1.782	082.C-0718(B)
		47	1.798	082.C-0718(B)
		48	1.806	082.C-0718(B)
		46	1.781	082.C-0718(B)
		45	1.783	082.C-0718(B)
		42	1.901	082.C-0718(B)
		44	1.836	082.C-0718(B)

Appendix C

LBLRTM recipe

The LBLRTM code is available for download at *http://rtweb.aer.com/lblrtm.html*. It has three different files: aer_v_X.X.tar.gz, aerlbl_vXX.X.tar.gz, and aerlnfl_vX.X.tar.gz. In the first we can find the all the spectral lines information, the second one permits us to write a file required as input by LBLTRM, which contains all the line parameters, and finally, the third one is the LBLRTM code itself, that will permit to construct the transmission spectra.

In this appendix I write a simple recipe to run the LBLRTM code, that will enable us to obtain the telluric spectra that we used our work.

C.1   LNFL − line file

To run the LBLRTM model, we first need to have the LBLRTM inputs, which are obtained by running the LNFL program with the a line file database for the spectral lines and cross sections for heavy molecules. The first thing we have to do is to extract the three files downloaded from the LBLRTM web-page. After the extraction, is time to make the executable file for LNFL. I have to go to the "build" folder inside the "lnfl" folder, where should be three files:

- makefile.common,

- make_lnfl,

- README.build_instructions,

and open a terminal in this folder. To create the LNFL executable file, we have to type in the terminal:

- > gmake -f make_lnfl <TARGET>

The target will depend on the OS and of the fortran version. The options are listed in the README.build_instructions file. In our case we used *linuxGNUsgl* for a Linux OS using GNU fortran, single precision compile. As output file we will have the executable file *lnfl_v2.6_linux_gnu_sgl* (this name will change according to the lnfl, OS, and fortran version), that will appear in the "lnfl" folder.

This executable file must be copied to our working directory, in which we will create the input file for the LBLRTM containing the line parameters. In the working directory we should also have the files:

- TAPE1

- and TAPE5.

The TAPE1 is noting more than the line parameter database in ASCII format. To have it on the working directory, one have to extract from aer_v_X.X.tar.gz the file called aer_v_X.X, that is inside the directory "line_file". Then one must either copy it to the working directory and rename it as TAPE1, or link it to the working directory, naming this link as TAPE1.

The TAPE5 is the LNFL input file in which we choose which molecular species, and the wavenumber range we want for our purposes. The file "lnfl_instructions" in the folder "lnfl/docs" contains the instructions on how to build the this TAPE5.

With the TAPE1, TAPE5, and the file *lnfl_v2.6_linux_gnu_sgl* in the working directory, the next step is to execute the executable file:

- > ./lnfl_v2.6_linux_gnu_sgl

As output a binary file with the name TAPE3 will be produced. This file contains information about the lines and it will be necessary to model the telluric spectra with the LBLRTM.

C.2 LBLRTM

As in previous section about the LNFL (Sect. C.1), we first need to produce an executable file for LBLRTM. The executable file is to be made inside the "build" directory in the "lblrtm" folder. We should confirm that inside the "build" directory there these three files are present:

- makefile.common,

- make_lblrtm,

- README.build_instructions,

and open a terminal in this directory. To create the LBLRTM executable file, we have to type in the terminal:

- > gmake -f make_lblrtm <TARGET>

Once again, the target will depend on the OS and of the fortran version. The options are listed in the README.build_instructions file. In our case we used *linuxGNUdbl* for a Linux OS using GNU fortran, double precision compile. As output file we will have the executable file *lblrtm_v12.1_linux_gnu_dbl* (this name will change according to the lblrtm, OS, and fortran version), that will appear in the "lblrtm" folder. This executable file should be copied/moved to the working directory, along with the TAPE3 resulting from the LNFL. We also need a input file called TAPE5 file. Although this file has the same name that the one used in the LNFL, the content will not be the same. This is the file in which we input the parameters for our modeled atmospheric spectra, wavenumber range, atmospheric model (it has five predefined models, and the option to input an user defined model), altitude, etc. The construction of this file in not obvious, especially in the case of the user defined model, for which all the molecular information for each layer, along with emissivity and reflectivity information, must be supplied. A instruction file for the construction of TAPE5 can be found in the "docs" folder of the "lblrtm" directory. Because these instructions are long and not always clear, my personal advice is to first understand the examples that are given with the LBLRTM model. When we have a valid TAPE5, we have to run the executable file in a terminal in the working directory:

- > ./lblrtm_v12.1_linux_gnu_dbl

As output will have several files called TAPEXX, the XX number will depend on the input file TAPE5. In our case, the output file that we wanted was the TAPE28, which contains the wavenumber and transmission information.

C.3   The use of the LBLRTM made easy

As it was stated earlier in this thesis, the use of the LBLRTM is not easy for a not-expert in the transmission spectra modeling person. During my thesis work I also collaborated in the development of an on-line platform to minimize this difficulty.

The ULME (the **u**se of **L**BLRTM **m**ade **e**asy) is an interface between the user and the LBLRTM code, written in php and that runs a python code. Although the php-based platform makes the use of the LBLRTM more intuitive, the user may choose to work only with the python code. The python code has to modalities:

- the interactive: the users enters a value for each parameter, and the users choices are restricted to avoid errors;

- the non interactive: the user inputs a file containing the parameters.

This is a work is still in progress and not yet available for the community.

Appendix D

Publications relevant for this thesis

- **D. Cunha**, N. C. Santos, P. Figueira, A. Santerne, J. L. Bertaux, C. Lovis, 2014, *Impact of micro-telluric lines on precise radial velocities and its correction*, Astronomy and Astrophysics, 568, A35;

- N. C. Santos, A. Mortier, J. P. S. Faria, X. Dumusque, V. Zh. Adibekyan, E. Delgado Mena, P. Figueira, L. Benamati, I. Boisse, **D. Cunha**, J. Gomes da Silva, G. Lo Curto, C. Lovis, J. H. C. Martins, M. Mayor, C. Melo, M. Oshagh, F. Pepe, D. Queloz, A. Santerne, D. Ségransan, A. Sozzetti, S. G. Sousa, S. Udry, 2014, *The HARPS search for southern extra-solar planets. XXXV. The interesting case of HD41248: stellar activity, no planets?*, Astronomy and Astrophysics, 566, A35;

- **D. Cunha**, P. Figueira, N. C. Santos, C. Lovis, G. Boué, 2013, *Impact of stellar companions on precise radial velocities*, Astronomy and Astrophysics, 550, A75.